

The Pennsylvania State University
The Graduate School
Department of Electrical Engineering

**ADVANCED COMPACT, LOW PROFILE ANTENNA DESIGNS FOR MODERN
COMMUNICATION SYSTEMS**

A Dissertation in
Electrical Engineering
by
Taiwei Yue

© 2018 Taiwei Yue

Submitted in Partial Fulfillment
of the Requirements
for the Degree of

Doctor of Philosophy

August 2018

The dissertation of Taiwei Yue was reviewed and approved* by the following:

Douglas H. Werner
John L. and Genevieve H. McCain Chair Professor of Electrical Engineering
Dissertation Advisor
Chair of Committee

Pingjuan L. Werner
Professor of Electrical Engineering

Ram. M. Narayanan
Professor of Electrical Engineering

Ramakrishnan Rajagopalan
Assistant Professor of Energy and Mineral Engineering

Kultegin Aydin
Professor of Electrical Engineering
Head of the Department of Electrical Engineering

*Signatures are on file in the Graduate School

ABSTRACT

In this dissertation, the design, analysis, and demonstration of multiple advanced compact and low-profile antennas with enhanced functionalities are presented with operational frequency bands ranging from microwave frequencies to the terahertz regime. Basic background knowledge is reviewed first in Chapter 1. In Chapter 2, three single-band antennas with compact sizes operating in the 4.0 GHz band are proposed. Specifically, the first two designs are linearly-polarized (LP) antennas with fractional bandwidths of more than 10% and unidirectional radiation patterns. The third design in Chapter 2 is a circularly-polarized (CP) antenna with an operational bandwidth exceeding 9% and a unidirectional radiation pattern. In Chapter 3, the design methodology of a dual-band antenna is introduced. The proposed LP antenna functions at both the 1.9 and 2.5 GHz frequency bands with unidirectional radiating characteristics. An ultra-compact footprint is achieved by the proposed antenna by virtue of rectangular complementary split ring resonator (CSRR) loadings, which also contributes to the dual-band functionality. In Chapter 4, a dual-band dual-sense CP antenna that operates at 1.9 and 2.5 GHz is proposed. The bi-anisotropic characteristic of the circular CSRR resonators is utilized in antenna engineering for the first time to realize the dual-band dual-sense CP radiation at broadside. Moreover, the size of the antenna is smaller than most of its counterparts reported in the literature. In Chapter 5, a highly miniaturized wideband wearable antenna with filtering characteristics is proposed for the 2.4 GHz industry, scientific, and medical (ISM) band based on the substrate-integrated-waveguide (SIW) technology. More importantly, the SIW structure is based on Eutectic Gallium-Indium (EGaIn) liquid metal and a flexible Styrene Ethylene Butylene Styrene (SEBS) polymer. This represents the first application of these flexible materials in antenna engineering. In Chapter 6, compact optical nanoantennas, referred to as surface plasma (SP) wave generators in this dissertation, are introduced to realize the generation of reconfigurable directional SP waves. In summary, these antennas with

miniaturized volumes and advanced functionalities are promising candidates for integration into various modern communication systems.

TABLE OF CONTENTS

List of Figures	vii
List of Tables	xii
Acknowledgements.....	xiii
Chapter 1 Introduction	1
1.1 Microstrip Patch Antennas	3
1.2 Substrate-Integrated-Waveguide (SIW).....	5
1.3 Surface Plasma (SP) Wave.....	8
1.4 Original Contribution.....	11
Chapter 2 Antenna Designs with Compact Form Factor Enabled by Metasurfaces Loaded with Interdigitated Capacitors	13
2.1 Introduction.....	13
2.1.1 Metasurfaces and Their Applications.....	13
2.1.2 MS-based Artificial Antenna Ground Plane	15
2.2 1D Loaded ICMS Enabled LP Antenna Design.....	16
2.2.1 Analysis of the ICMS Unit Cell	17
2.2.2 Simulated Antenna Performances	20
2.2.3 Antenna Working Principles	25
2.2.4 Experimental Results.....	30
2.3 2D Loaded ICMS Enabled LP Antenna Design.....	32
2.3.1 Simulated Antenna Performances	34
2.3.2 Parametric Study of the ICs along the y-axis	36
2.3.3 Experimental Results.....	38
2.4 ICMS Enabled CP Antenna Design	39
2.4.1 Analysis of ICMS Unit Cell	40
2.4.2 Simulated Antenna Performances	42
2.4.3 Experimental Results.....	46
2.5 Conclusion	48
Chapter 3 Miniaturized Dual-band Antenna Enabled by an Artificial Ground Plane Loaded with Complementary Split Ring Resonators	50
3.1 Introduction.....	50
3.2 Antenna Design.....	52
3.2.1 Unit Cell Synthesis and Analysis	54
3.2.2 Simulated Antenna Performances	56
3.2.3 Antenna Working Principles	60
3.3 Individual Band-tuning Technique	65
3.4 Comparison with Conventional U-Slot Antenna	70
3.5 Experimental Results	73

3.6 Conclusion	76
Chapter 4 A Compact Dual-Band Dual-Sense Circularly-Polarized Antenna Enabled by a CSRR Loaded Metasurface.....	78
4.1 Introduction.....	78
4.2 Antenna Design.....	80
4.3 Unit Cell Analysis.....	82
4.4 Simulated Antenna Performances	87
4.5 Conclusion	91
Chapter 5 A Novel Wearable Quarter-Mode Substrate Integrated Waveguide Antenna Design Enabled by Flexible Materials	92
5.1 Introduction.....	92
5.1.1 SIW Antenna.....	92
5.1.2 SIW Wearable Antenna.....	93
5.2 Flexible QMSIW Antenna Design with Novel Flexible Materials	95
5.3 Wearable Stacked QMSIW Antenna	105
5.3.1 Antenna Deformations	105
5.3.2 Human Body Loading Effect	108
5.4 Conclusion	113
Chapter 6 Reconfigurable Directional Surface Plasma (SP) Wave Generators.....	114
6.1 Introduction.....	114
6.2 Unidirectional SP wave Generator Based on Nanowires (NWs).....	115
6.2.1 NW Pair.....	115
6.2.2 NW in Nanogroove (NG).....	122
6.3 Reconfigurable SP Wave Generator Based on VO ₂ Material	124
6.3.1 VO ₂ Material.....	124
6.3.2 VO ₂ based SP wave generator Design.....	125
6.4 Conclusion	127
Chapter 7 Future Work	128
Bibliography.....	129

LIST OF FIGURES

Figure 1-1. Configuration of a rectangular microstrip antenna [11].	4
Figure 1-2. TM_{10} mode of a patch antenna approximated by the cavity model.	5
Figure 1-3. 3D configuration of a rectangular SIW.	7
Figure 1-4. Snapshot of instantaneous magnitude of the E -field within a rectangular SIW.	8
Figure 1-5. Interface between dielectric and metal layers that can support the propagation of SP waves [8].	10
Figure 1-6. Calculated normalized H -field along (a) z - and (b) x -directions based on Eq. (1-5).	11
Figure 2-1. 3D configuration and side view of the proposed integrated LP antenna.	17
Figure 2-2. (a) HFSS simulation and (b) the equivalent circuit model of an ICMS unit cell.	18
Figure 2-3. (a) Simulated results of unit cells with and without IC loading, and parametric studies on (b) s_1 , (c) f_1 , and (d) the number of fingers.	19
Figure 2-4. Simulated and measured (a) impedance matching and (b) broadside gain performances of the LP integrated antenna with a 1D loaded ICMS artificial ground plane.	21
Figure 2-5. Simulated input impedance of the feeding monopole antenna alone in free space.	22
Figure 2-6. Simulated and measured radiation patterns on the (a) E -plane and (b) H -plane (dashed line: simulated; solid line: measured).	23
Figure 2-7. Scenarios where the monopole antenna is shifted along the (a) x and (b) y directions.	24
Figure 2-8. Simulated impedance matching and gain performances with the monopole antenna staggered along the (a) x and (b) y directions.	25
Figure 2-9. Simulated and sketched E -field distributions on the (a) $y = 0$ and (b) $x = 33$ mm planes at 3.75 GHz.	26
Figure 2-10. Simulated and sketched E -field distributions on the (a) $y = 0$ and (b) $x = 33$ mm planes at 4.20 GHz.	27
Figure 2-11. (a) Simulation setup and (b) dispersion curves of the ICMS- TM_{10} (left) and ICMS- TM_{12} (right) modes.	29

Figure 2-12. Simulated (a) current and (b) <i>E</i> -field distributions on the top surface of the ICMS artificial ground plane at 4.20 GHz.	30
Figure 2-13. Antenna prototype of the 1D loaded ICMS artificial ground plane enabled integrated antenna.	31
Figure 2-14. Configurations of (a) the 2D loaded ICMS and (b) the monopole antenna.	33
Figure 2-15. Simulated (a) impedance matching and (b) gain profile of the 2D loaded ICMS enabled LP antenna.	35
Figure 2-16. Simulated and measured radiation patterns on the (a) <i>E</i> -plane and (b) <i>H</i> -plane (dashed line: simulated; solid line: measured).	36
Figure 2-17. (a) Integrated antennas enabled by an ICMS artificial ground plane that contains extra ICs with different numbers of fingers along the <i>y</i> -axis, (b) simulated <i>S11</i> of the antennas, and (c) resonant frequencies with varying numbers of fingers of ICs along the <i>y</i> -axis.	38
Figure 2-18. Antenna prototype of the 1D loaded ICMS enabled integrated antenna design.	38
Figure 2-19. Configuration of the ICMS enabled CP antenna design.	40
Figure 2-20. (a) Simulation model and (b) simulated ratio of magnitudes of TE to TM modes and phase difference between TE and TM modes.	42
Figure 2-21. Simulated and measured (a) impedance matching, (b) broadside AR, and (c) gain performances of the ICMS enabled CP antenna.	43
Figure 2-22. Simulated and measured radiation patterns on the (a) <i>xoz</i> -plane and (b) <i>yo_z</i> -plane (dashed line: simulated; solid line: measured).	44
Figure 2-23. Simulated and measured angular AR at (a) 3.9, (b) 4.0, and (c) 4.1 GHz.	46
Figure 2-24. Antenna prototype of the ICMS enabled integrated CP antenna design.	46
Figure 3-1. Configurations of (a) the dual-band MS artificial ground plane enabled integrated antenna and (b) the printed planar monopole feeding antenna.	54
Figure 3-2. Exploded and stacked view of a CSRR loaded double-layered unit cell.	54
Figure 3-3. (a) Simulated and calculated dispersion properties and (b) the equivalent circuit of a single MS unit cell. The finalized circuit parameters are $C_{se} = 1$ pF, $C_f = 5$ pF, $C_{sh} = 0.3$ pF, $CCSRR = 0.48$ pF, and $LCSRR = 5.7$ nH.	56
Figure 3-4. Simulated and measured impedance matching performances of the proposed dual-band LP antenna enabled by an MS artificial ground plane.	58

Figure 3-5. Simulated and measured broadside gains of the (a) first and (b) second frequency band.....	58
Figure 3-6. Simulated and measured normalized radiation patterns on the <i>E</i> -plane and <i>H</i> -plane at (a) 2.0 and (b) 2.5 GHz (dashed lines: simulated; solid lines: measured; black lines: co-polarization; grey lines: cross-polarization).....	59
Figure 3-7. Illustration of the second order within the second band.....	61
Figure 3-8. Simulated and sketched <i>E</i> -field distributions at 2.0 and 2.5 GHz on (a) $y = 0$ and (b) $x = 64$ mm planes.....	62
Figure 3-9. (a) Configurations and (b) simulated <i>SII</i> performances of integrated antennas with different MS artificial ground planes.....	64
Figure 3-10. Independent tuning of the first operational band by adjusting <i>du1</i>	66
Figure 3-11. Parametric studies of (a) <i>du2</i> , (b) <i>LC</i> , and (c) <i>WC</i>	68
Figure 3-12. Individual band-tuning technique for the second operational band, which relies on simultaneously varying the parameters (a) <i>du1</i> and <i>du2</i> , (b) <i>du1</i> and <i>LC</i> , and (c) <i>du1</i> and <i>WC</i>	70
Figure 3-13. Configurations of (a) proposed antenna, (b) FR-4, and (c) RO4003 U-slot patch antennas. Comparisons of (d) <i>SII</i> , gain performances at (e) lower and (f) higher bands, and FB ratios at (e) lower and (f) higher bands among the three antennas.....	72
Figure 3-14. Antenna prototype of the proposed dual-band MS artificial ground plane enabled integrated antenna.....	73
Figure 4-1. (a) 3D exploded and (b) side views of the proposed antenna. (c) Top (left) and bottom (right) views of the monopole antenna.	82
Figure 4-2. (a) Configuration of a single unit cell. (b) Detailed dimensions of the CSRR resonator.....	83
Figure 4-3. Field decomposition of \mathbf{E}_m	83
Figure 4-4. Dispersion behavior of a single unit cell with wave propagating (a) parallel and (b) perpendicular to the symmetrical line of the CSRR resonator.	85
Figure 4-5. Dispersion behavior of a unit cell loaded with NBCSRR.	86
Figure 4-6. Simulated <i>SII</i> of the proposed dual-band dual-sense CP antenna.	88
Figure 4-7. Simulated broadside AR performance of the proposed antenna.	89
Figure 4-8. Simulated broadside antenna gains of the proposed antenna at the (a) first and (b) second operational bands.....	89

Figure 4-9. Simulated normalized radiation patterns on (a) $\phi = 45^\circ$ and (b) $\phi = 135^\circ$ planes at 1.90 (left) and 2.47 (right) GHz.	91
Figure 5-1. Configuration of a conventional QMSIW antenna with equal length and width.	95
Figure 5-2. The simulated (a) resonant frequency and (b) S_{11} at the resonant frequency of the QMSIW antenna.....	96
Figure 5-3. Simulated S_{11} performances of the QMSIW antenna with different feeding positions.	97
Figure 5-4. Configuration of the stacked QMSIW antenna.	98
Figure 5-5. Simulated S_{11} of the preliminary stacked QMSIW antenna design with $LS = WS = 36$, $LQ = WQ = 26$, $LQs = WQs = 26$, $r1 = 0.5$, $r2 = 1.0$, $wf = 2.6$, $h = 6.3$, $mx = my = 0$, $fx = fy = 0.3$, all in millimeter.	99
Figure 5-6. Parametric studies on (a) fx and (b) fy	100
Figure 5-7. Parametric studies on (a) mx and (b) my	101
Figure 5-8. Parametric studies on (a) LQs and (b) WQs	103
Figure 5-9. Simulated S_{11} and gain of the proposed stacked QMSIW antenna.....	104
Figure 5-10. Simulated normalized radiation patterns on the (a) E -plane and (b) H -plane at 2.44 GHz.	105
Figure 5-11. Bent stacked QMSIW antenna.	106
Figure 5-12. Simulated banding effect on the S_{11} of the proposed stacked QMSIW antenna.	107
Figure 5-13. Simulated banding effect on the gain of the proposed stacked QMSIW antenna.	107
Figure 5-14. Simulated bending effect on the normalized radiation patterns of the proposed stacked QMSIW antenna on the (a) E -plane and (b) H -plane.	108
Figure 5-15. Simulation setup for modeling antenna being placed on human chest.	109
Figure 5-16. Simulated antenna performances when the antenna is placed human chest model.....	110
Figure 5-17. Simulated normalized radiation patterns at 2.44 GHz on the (a) E -plane and (b) H -plane when the antenna is placed human chest model (dot line: antenna in free space; solid line: co-polarization; dashed line: cross-polarization).	110
Figure 5-18. Simulation of the stacked QMSIW antenna placed on human arm.....	111

Figure 5-19. Simulated antenna performances when the antenna is placed human arm model.....	112
Figure 5-20. Simulated normalized radiation patterns at 2.44 GHz on the (a) E -plane and (b) H -plane when the antenna is placed human arm model (dot line: antenna in free space; solid line: co-polarization; dashed line: cross-polarization).	112
Figure 6-1. (a) 3D configuration and (b) side view of a two-element Si NW array on top of a gold film.....	117
Figure 6-2. Analytically calculated $E \pm yEspp$ with plane wave incident angle equal to (a) 0 and (b) $\pi/2$	119
Figure 6-3. Simulated (a) $Ez, \pm y$ (V/m) and (b) ER (dB) with varying d	119
Figure 6-4. Snapshots of the Ez when the SP wave generator is illuminated by an obliquely incident plane wave with $d = 300$ nm, $d = 980$ nm, and $d = 800$ nm.	119
Figure 6-5. (a) 3D configuration and (b) 2D side view of the simulation setup.	121
Figure 6-6. Simulated (a) $Ez, \pm y$ and (b) ER (dB) with varying NW-separation d	122
Figure 6-7. Snapshots of the Ez when the proposed SP generator is illuminated by a normally incident plane wave with $d = 310$ nm, $d = 460$ nm, and $d = 630$ nm.	122
Figure 6-8. (a) 3D configuration and (b) 2D side view of the simulation setup.	123
Figure 6-9. Simulated (a) $Ez, \pm y$ and (b) ER (dB) with varying NW-separation d	124
Figure 6-10. Snapshots of the Ez when the proposed SP wave generator is illuminated by a normally incident plane wave with $d = 0$, $d = 220$ nm, and $d = 140$ nm.	124
Figure 6-11. (a) 3D configuration and (b) 2D side view of the proposed reconfigurable SP wave generator.	126
Figure 6-12. Simulated ER (dB) with varying d and ϵd when the VO2 NW is in (a) metal and (b) insulator phase.	126
Figure 6-13. Snapshots of the Ez of the generated SP wave that propagates along the $-y$ direction when the SP wave generator is illuminated by a normally incident plane wave with the VO2 NW in (a) metal and (b) insulator phases.....	127

LIST OF TABLES

Table 2-1. Detailed Dimension of the Proposed 1D Loaded ICMS Based Antenna (all in mm).....	17
Table 2-2. Detailed Dimensions of the Proposed 2D Loaded ICMS Enabled LP Antenna (all in mm).....	33
Table 2-3. Detailed Dimensions of the Proposed ICMS Based CP Antenna (all in mm).....	40
Table 2-4. Optimized Design Parameters of the ICMS Unit Cell (all in mm).....	42
Table 2-5. Comparison of Artificial Ground Plane Enabled Antenna Designs.	48
Table 3-1. Detailed Dimensions of the Proposed Dual-Band Antenna (all in mm).....	57
Table 3-2. Analytically Predicted and Numerically Simulated Resonant Frequencies of Different Dual-band MS Artificial Ground Plane Enabled Antennas.....	65
Table 3-3. Comparison of Dual-Band and Multi-Band Antennas Enabled by MS.....	75
Table 4-1. Detailed Dimensions of the Proposed Dual-Band Dual-Sense CP Antenna (all in mm).....	87
Table 5-1. Finalized Design Parameters for the Stacked QMSIW Antenna (all in mm).	103
Table 5-2. Electromagnetic Properties and Dimensions of Skin, Fat, Muscle, and Bone of Human Body Models.	108

ACKNOWLEDGEMENTS

Many thanks should be given to various people who have helped me with my study, research, and life in numerous aspects. Without their support and encouragement, this dissertation would have never been accomplished.

First, I would like to thank my research advisor and committee chair, Dr. Douglas H. Werner, for his valuable guidance and support during my Ph.D. studies. I would also like to thank my committee members, Dr. Pingjuan L. Werner, Dr. Ram. M. Narayanan, and Dr. Ramakrishnan Rajagopalan, for their valuable suggestions on this dissertation. A special thank you is given to my former lab mate, Dr. Zhi Hao Jiang, who helped me overcome many difficulties, both in my research and my personal life. His passion for academia, humility, and optimism about life always encouraged me. I would also like to thank all the members of the Computational Electromagnetics and Antennas Research Laboratory (CEARL) for their advice, suggestions, and continuous help.

I would like to thank all my friends, both in the United States and back in China, as they always had my back when I was frustrated.

Finally, I would like to thank my parents, Yiguo Yue and Huifen Zhang, for their unconditional love and encouragement.

The research works presented in Chapter 2, 3, 4, and 5 were supported by the National Science Foundation (NSF) Nanosystems Engineering Research Center on Advanced Self-Powered Systems of Integrated Sensor Technologies (ASSIST), under the award 2012-1067-01. The work presented in Chapter 6 was funded by the Penn State Materials Research Science and Engineering Center (MRSEC), Center for Nanoscale Science, under the award NSF DMR-1420620

To Yiguo Yue and Huifen Zhang, my beloved parents.

To the city of Wuhan where I always belong.

To Nanjing University where my adventures were begun.

Chapter 1

Introduction

With the rapid development of modern wireless communication systems, the miniaturization of their constituting components has become increasingly emphasized. Hence, considerable research efforts have been devoted to the size reduction of antennas, as antennas act as the key elements in wireless communication systems by establishing wireless links between different nodes. Specifically, antennas in modern wireless communication systems are preferred to have low profiles, small footprints, low weights, and low costs. Numerous types of antennas have recently been proposed to meet these preferences.

For example, traditional three-dimensional (3D) antennas have been modified to possess two-dimensional (2D) configurations. An example is the very low-profile monopole antenna used in mobile phones [1]. Another example is the printed microstrip patch antenna [5], which is widely used in different wireless communication systems, including global positioning systems (GPS), satellite communication systems, and wireless local area networks (WLAN), among other technologies. In Chapters 2, 3, and 4 of this dissertation, five low-profile and compact antennas are introduced. These antennas operate similar to a rectangular patch antenna but have the dispersive behavior to achieve wide-band or multi-band functionalities with linearly-polarized (LP) or circularly-polarized (CP) radiating characteristics. To help develop a better understanding of the working principles of the proposed antenna designs, a brief overview of the design and analysis of microstrip patch antennas is presented in Section 1.1.

While microstrip patch antennas have been favored mostly in sub-6 GHz frequency bands, the frequency spectrum of certain communication systems has recently been extended to the

millimeter-wave (mm-wave) band to achieve a higher data rate, as measured in gigabits per second (Gbps). An example of these communication systems is the fifth-generation (5G) communication system expected to be available in the early 2020s [2]. The traditional microstrip or coplanar waveguide (CPW) structures are not suitable for such applications due to their high losses in the high frequency band and the difficulties in fabrication and integration in complex packaging environments [3]. To solve this problem, a new structure named the substrate-integrated-waveguide (SIW) has recently been proposed as a tool for developing mm-wave devices such as mm-wave antennas [4]. The SIW structure can be regarded as a low-profile 2D H -plane waveguide that can easily be fabricated with lightweight and low-cost features based on standard printed circuit board (PCB) techniques. Another desirable characteristic of the SIW is its high isolation from its surroundings, which allows SIW-based antennas to easily be integrated into various complicated packaging situations. Moreover, its low loss and high quality-factor are also highly preferred.

Beyond their mm-wave applications, SIW-based antennas are fabricated based on novel flexible materials and used in wearable wireless communication systems [6]. These SIW-based wearable antennas possess a high isolation from human bodies. In Chapter 5 of this dissertation, a novel, highly miniaturized wideband wearable antenna based on SIW technology is proposed, operating at the 2.4 GHz industry, scientific, and medical (ISM) band. The dielectric layers of the proposed antenna are the Styrene Ethylene Butylene Styrene (SEBS) polymer with a dielectric constant $\epsilon_r = 2.52$ and a loss tangent $\tan\delta = 0.00045$. The vertical electroplated via holes involved in traditional PCB-based SIW structures (explained in detail in Section 1.2) are replaced by Eutectic Gallium-Indium (EGaIn) liquid metal [9] walls. In this way, the proposed wearable SIW-based antenna does not need to be ultra-thin to maintain its flexibility, a difficulty that is commonly seen in state-of-the-art designs. This development ultimately leads to the possibility of bandwidth enhancement. A brief introduction to the SIW technique is presented in Section 1.2.

In addition to the sub-6 GHz and mm-wave frequency ranges, terahertz and optical bands are also of interest in communication systems, where they can help to bridge the gap between electronics and photonics [3]. Nanoantennas have been thus developed to work at the terahertz and optical bands to enhance or tailor the light emissions [7]. Additionally, the manipulation of the surface waves, such as surface plasma (SP) waves, at optical frequency range have also been explored by researchers. This is because the SP waves have been widely applied in numerous nanotechnologies, including integrated photonic circuits, surface-enhanced Raman scattering (SERS), biological spectroscopy and sensing, among others [8]. The generation of the SP waves is thus a critical procedure. Many SP wave generators are designed by researchers to realize functional SP wave generation. Basically, an SP wave generator can couple the plan waves from free space to SP waves bonded at the interface between metals and insulators. While traditional SP wave generators suffer from bulky size and low efficiency, and can only provide bi-directional propagating SP waves, four novel SP wave generators are proposed in Chapter 6 of this dissertation to achieve the reconfigurable directional generation of SP waves with compact sizes. In this chapter, basic background knowledge about SP waves is reviewed in Section 1.3.

1.1 Microstrip Patch Antennas

A typical microstrip patch antenna consists of a metallic patch of a certain shape printed on a grounded dielectric slab. The patch of a microstrip patch antenna can be of different shapes, such as a disk, rectangle, or triangle. A patch antenna can be regarded as a radiating resonator, and two analytical methods are usually adopted to model its resonating behavior. The first one is the transmission line model, and the second is the cavity model. It should be noted that only the rectangular microstrip patch antenna is considered in this dissertation, but antennas with other shapes can be analyzed in similar ways.

Figure 1-1 shows the configuration of a rectangular patch antenna fed by a microstrip line [11]. The curved arrows show the E -field distributions at its two ends. The in-phase magnetic currents generated by these E -fields at the two edges contribute constructively to the far-field radiation of the antenna at broadside. It should be noted that the two notches cut into the rectangular patch are used to obtain an optimal impedance matching. Besides the microstrip line feeding method used in Figure 1-1, there are other ways to feed a microstrip patch antenna, including the probe-feeding, aperture-coupled, and proximity-coupled methods [11].

According to the transmission line model, a patch radiator can be modeled by a parallel resistor-inductor-capacitor (RLC) resonator, where the resistance accounts for the radiation from the patch antenna. This parallel RLC circuit approximation is held valid except for in the aperture-coupled feeding method, where a more complicated equivalent circuit is required [11]. A microstrip line or probe feeds the antenna inductively, while a proximity-coupled or an aperture-coupled feeding tends to be capacitive. The transmission line model of a patch antenna is the simplest, but it can only offer analytical approximation with limited accuracy. Moreover, it cannot explain the field distribution within the patch antenna or its far-field radiation characteristics.

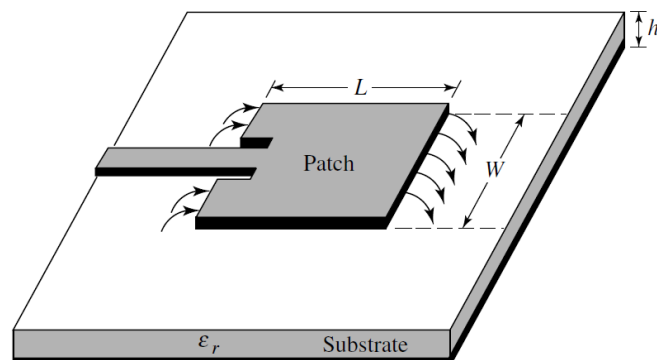


Figure 1-1. Configuration of a rectangular microstrip antenna [11].

The cavity model is another way to conduct patch antenna analysis. Basically, a patch radiator is approximated to a cavity resonator. The top and bottom surfaces of the patch radiator are approximated to perfect electrical conductors (PECs) and the four side walls are assumed to be perfect magnetic conductors (PMCs). By solving the electromagnetic fields inside the cavity with corresponding boundary conditions, the resonant frequencies as well as the field distributions within the antenna can be determined. It should be noted that, because the height of a patch antenna is extremely low, the E -fields are assumed to be perpendicular to the top and bottom surfaces with no phase variations. Figure 1-2 shows the fundamental TM_{10} mode of a patch antenna [11] with arrows indicating the E -fields.

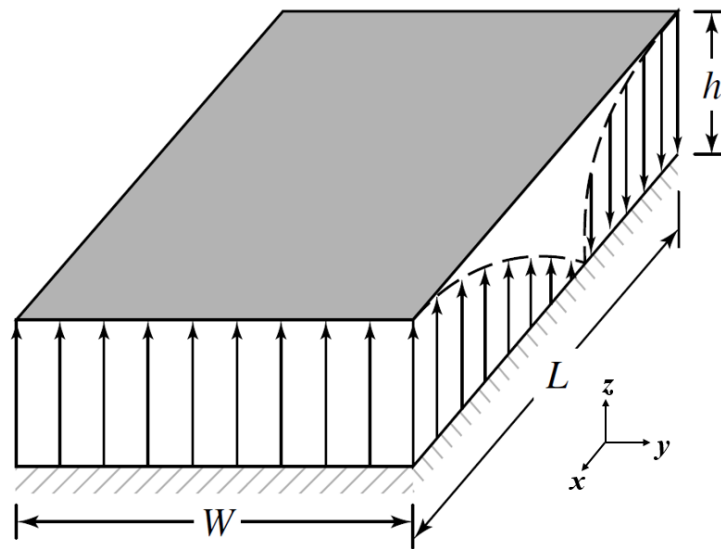


Figure 1-2. TM_{10} mode of a patch antenna approximated by the cavity model.

1.2 Substrate-Integrated-Waveguide (SIW)

SIWs, which originated from the concept of substrate-integrated circuits, have received increasing attention from researchers and engineers since they were first reported in [12]. An SIW simultaneously realizes the low profile of the traditional microstrip transmission line and the high

quality-factor of conventional 3D metallic waveguides. These features make the SIW the key enabling technology in many applications, such as mm-wave and wearable communication devices.

Figure 1-3 shows a typical rectangular SIW. It should be noted that Figure 1-3 also shows two SIW-microstrip transitions [12] at the two ends of the SIW; through these, the SIW can be integrated with a microstrip-based circuit. As can be seen, the SIW-microstrip transitions are actually tapered microstrip transmission lines. The tapering of the microstrip transmission lines can be calculated based on the equations proposed in [13]. There have also been SIW-to-coplanar waveguide (CPW) transitions [14] reported in the literature. From the figure we can see that the SIW consists of two metallic layers printed on the two opposite faces of a standard PCB along with two columns of electroplated via holes penetrating the PCB and electrically connecting the two metallic layers. The distance between the two columns of via holes is denoted as W_{SIW} , which is also referred to as the width of the SIW. The thickness of the PCB is denoted as t , and the diameter of a single via hole is d . The distance between via holes in each column is kept at a certain constant p so as to mimic the side walls of a traditional metallic waveguide. The value of p can be determined based on [4] as

$$\frac{p}{d} < 2.5 \quad (1-1)$$

and it is recommended that $p = 2d$.

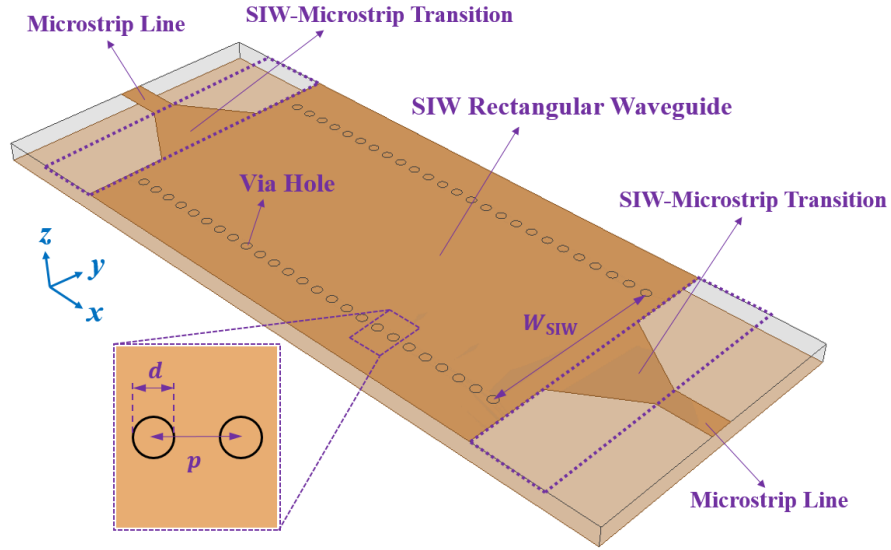


Figure 1-3. 3D configuration of a rectangular SIW.

In [15], the authors pointed out that only TE_{n0} modes can be supported by a rectangular SIW. Using both numerical simulations and experiments, they demonstrated that the dispersion characteristics of rectangular SIWs are equivalent to conventional rectangular waveguides. Specifically, according to [16], an SIW with a width equal to W_{SIW} has the same dispersion characteristics as a metallic rectangular waveguide with width W . That is,

$$W = W_{SIW} - \frac{d^2}{0.95p}. \quad (1-2)$$

A more accurate relation is [15]

$$W = W_{SIW} - 1.08 \frac{d^2}{p} + 0.1 \frac{d^2}{W_{SIW}}, \quad (1-3)$$

taking into account the effect of d/W_{SIW} .

Although modern advanced computational resources have allowed full-wave simulations to be carried out in designing SIWs, the aforementioned equations can be utilized to give an approximated characterization of SIWs with high accuracy. Figure 1-4 shows the operation of an SIW by numerical simulation.

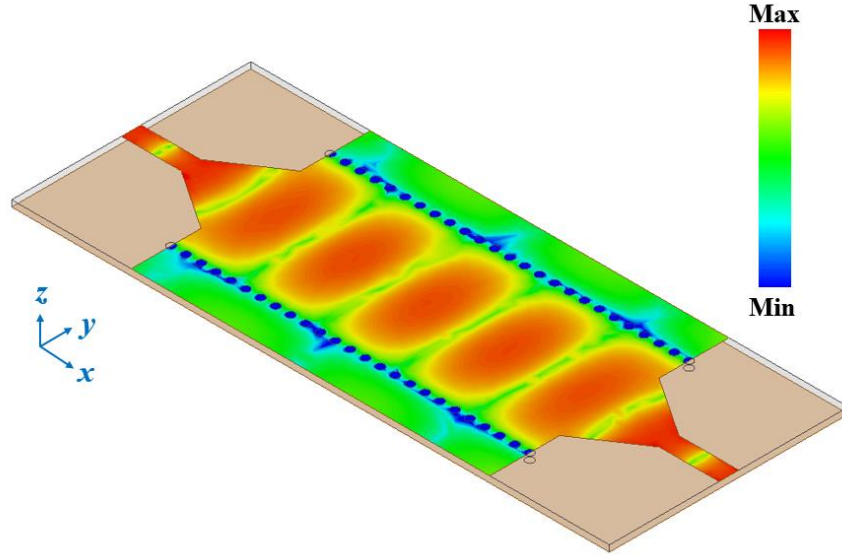


Figure 1-4. Snapshot of instantaneous magnitude of the E -field within a rectangular SIW.

Given this SIW technology, both passive and active circuit components have been proposed, including SIW-based filters [17], antenna array beamforming networks [18], oscillators [19], and amplifiers [20]. Besides, the SIW technology has also been found to be widely applicable in antenna engineering. Chapter 5 illustrates the SIW-based antenna technology in detail.

1.3 Surface Plasma (SP) Wave

Metals at optical wavelength possess different properties than they do at microwave frequencies, where they are considered simply as PECs. However, as the frequency increases to optical frequency range, the behavior of the metals is more like dielectric materials with finite dielectric constants ϵ_m . A well-known equation for calculating ϵ_m at frequency f is based on [8]:

$$\epsilon_m = \epsilon_\infty - \frac{\omega_p^2}{\omega^2 - i\omega\gamma}, \quad (1-4)$$

where ϵ_∞ is a dielectric constant usually between 1 and 10, ω_p is the plasma frequency varying among different metals, γ is the characteristic collision frequency also varying among different

metals, and $\omega = 2\pi f$ is the angular frequency. A More rigorous characterization of the complex dielectric constant of metals at optical and terahertz frequencies can be obtained through experiments.

Researchers have already verified that at optical frequency, the real part of the dielectric constant of some noble metals, such as silver and gold, has negative value, *i.e.* $\text{Re}\{\epsilon_m\} < 0$. This special characteristic leads to the existence of SP waves that are highly bonded at the interface between these noble metals and insulators with dielectric constant ϵ_d . As pointed out in [8], a SP wave can be only a transverse magnetic (TM) wave with its E -field and H -field written as

$$\vec{H}_{sp} = \hat{y}H_y(x, y) = \hat{y}Ae^{i\beta_{SP}x}e^{-k_dz} \quad (1-5a)$$

$$\vec{E}_{sp} = \hat{x}E_x + \hat{z}E_z = \hat{x}iA\frac{1}{\omega\epsilon_0\epsilon_d}k_d e^{i\beta_{SP}x}e^{-k_dz} - \hat{z}A\frac{\beta_{SP}}{\omega\epsilon_0\epsilon_d}e^{i\beta_{SP}x}e^{-k_dz} \quad (1-5b)$$

for $z > 0$, and

$$\vec{H}_{spp} = \hat{y}H_z(x, y) = \hat{y}Ae^{i\beta_{SP}x}e^{k_mz} \quad (1-5c)$$

$$\vec{E}_{spp} = \hat{x}E_x + \hat{z}E_z = -\hat{x}iA\frac{1}{\omega\epsilon_0\epsilon_m}k_1 e^{i\beta_{SP}x}e^{k_mz} - \hat{z}A\frac{\beta_{SP}}{\omega\epsilon_0\epsilon_m}e^{i\beta_{SP}x}e^{k_mz} \quad (1-5d)$$

for $z < 0$,

where A is the complex magnitude of the SP wave, β_{SP} is the SP wave propagation constant written as

$$\beta_{SP} = k_0\sqrt{\frac{\epsilon_m\epsilon_d}{\epsilon_m+\epsilon_d}}. \quad (1-6)$$

In Eq. (1-6), k_d and k_m are the components of the wave vector along the z -direction, respectively, and are written as

$$k_d^2 = \beta_{SP}^2 - k_0^2\epsilon_d \quad (1-7a)$$

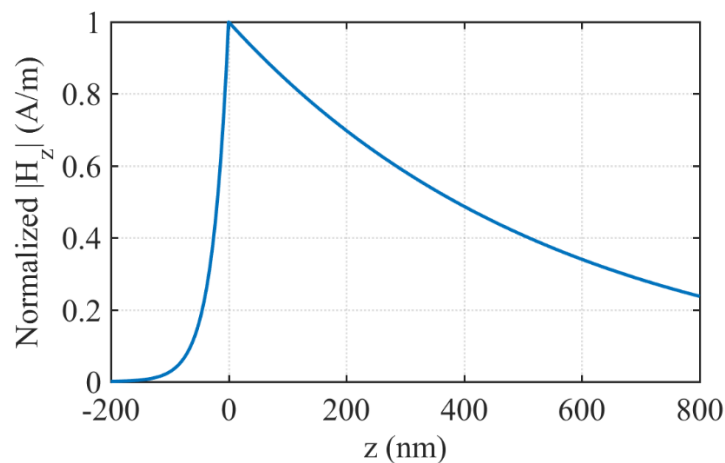
$$k_m^2 = \beta_{SP}^2 - k_0^2\epsilon_m. \quad (1-7b)$$



Figure 1-5. Interface between dielectric and metal layers that can support the propagation of SP waves [8].

The detailed derivations of SP waves can be found in [8] by solving wave equations along with corresponding boundary conditions.

Here, the normalized H -field profile of the SP wave along the z -axis at an arbitrary point along the interface between gold and air is calculated at 800 nm wavelength based on Eq. (1-5) with the dielectric constant of gold extracted from [21]. The SP wave is propagating along the positive x -direction. The H -field profile is plotted as shown in Figure 1-6(a). The normalized H -field (normalized to unity at $x = 0$) along the x -direction at an arbitrary distance from the interface is also calculated based on Eq. (1-5) and plotted in Figure 1-6(b).



(a)

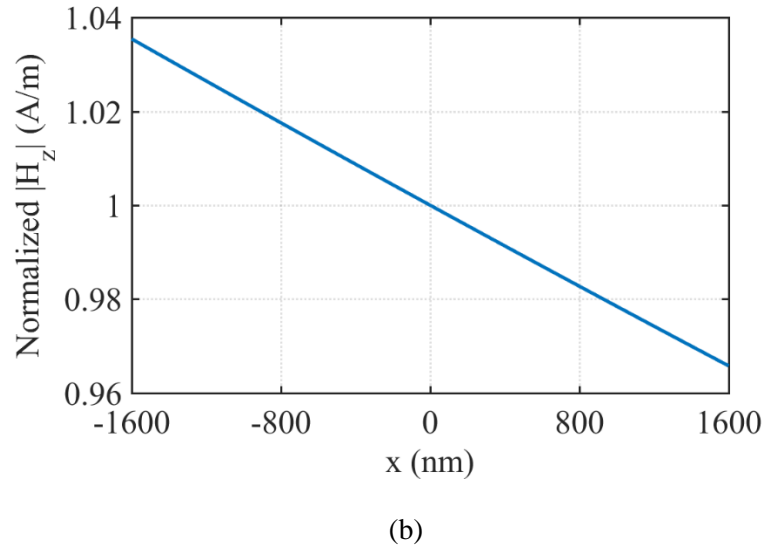


Figure 1-6. Calculated normalized H -field along (a) z - and (b) x -directions based on Eq. (1-5).

From Figure 1-6(a), it can be seen that the $|H_z|$ of the SP wave has a maximum value at the interface and experiences exponential decays into both the dielectric and metal layers. On the other hand, as shown, the $|H_z|$ experiences a small decay along the x -direction due to the imaginary part of β_{SP} .

In Chapter 6, various SP wave generation methods are reviewed, and the proposed reconfigurable directional SP wave generators are presented.

1.4 Original Contribution

During my Ph.D. studies at Penn State University, I have made the following contributions to the field of antenna engineering:

- Designed, fabricated, and tested a compact and low-profile LP antenna with wide operational band at 4.0 GHz enabled by a metasurface (MS) loaded with interdigitated capacitors (ICs) along one dimension [59]

- Designed, fabricated, and tested a compact and low-profile LP antenna with a wide operational band at 4.0 GHz enabled by an MS loaded with ICs along two dimensions [59]
- Designed, fabricated, and tested a compact and low-profile CP antenna with a wide operational band at 4.0 GHz enabled by an MS loaded with ICs [59]
- Designed, fabricated, and tested an ultra-compact, dual-band antenna operating at 1.9 and 2.5 GHz enabled by an MS loaded with complementary split ring resonators (CSRRs) [152]
- Designed a compact dual-band, dual-sense CP antenna operating at 1.9 and 2.5 GHz enabled by an MS loaded with CSRRs [153]
- Designed a compact stacked quarter mode substrate-integrated-waveguide (QMSIW) wearable antenna operating at 2.4 GHz with a wide operational band and filtering characteristics
- Designed a reconfigurable, directional SP wave generator consisting of two identical silicon (Si) nanowires (NWs)
- Designed a reconfigurable, directional SP wave generator consisting of two distinct Si NWs
- Designed a reconfigurable, directional SP wave generator consisting of a Si NW placed inside a gold nanogroove (NG)
- Designed a reconfigurable, directional SP wave generator consisting of a dielectric NW and a vanadium oxide (VO₂) NW.

Chapter 2

Antenna Designs with Compact Form Factor Enabled by Metasurfaces Loaded with Interdigitated Capacitors

2.1 Introduction

2.1.1 Metasurfaces and Their Applications

Metasurfaces (MSs), which are the 2D counterparts of 3D metamaterials with near-zero electrical thickness, have attracted more and more attention from researchers and engineers recently because of their artificial electromagnetic behaviors, fully planar configuration, and ease of fabrication. Numerous MSs have been reported, all of which can be generally categorized into three classes. The first class of MSs is reactive impedance surfaces (RISs) with engineered surface impedance of reactive values. The second class of MSs is referred to as electromagnetic bandgap (EBG) surfaces that can block the propagation of waves within certain frequency ranges. The third class of MSs is artificial magnetic conductors (AMCs), which mimic the behavior of magnetic conducting surfaces.

Most of the MSs have the same configuration, with subwavelength unit cells periodically placed to form planar arrays. Depending on the unit cells as well as their arrangement, MSs can be synthesized to exhibit either isotropic, anisotropic, or bi-anisotropic electromagnetic behaviors. Usually, a unit cell consists of specific metallic patterns printed on a grounded dielectric substrate. There can also be conducting vias/holes imbedded within the substrate in order to electrically connect the metallic patterns and the ground. In the literature, many unit cell designs have been reported. For example, in [22], the well-known mushroom-shaped unit cell was proposed. A

modified mushroom-shaped unit cell was subsequently reported in [23]. Unlike mushroom-type unit cells with the involvement of conducting vias, there are also uniplanar unit cells, such as the I-shaped patch resonator reported in [24] and the Jerusalem cross dipole resonator reported in [25]. Unit cells that possess wide/multiple operational bands and/or polarization dependable responses with more complicated metallic patterns have been also developed in [26-28].

Researchers have developed an analytical measure, the surface impedance tensor [29], to describe the electromagnetic response of MSs. The electromagnetic behavior of MSs can also be rigorously characterized using numerical simulations performed by commercially available software such as the high frequency structure simulator (HFSS) [30].

MSs are found to be widely applicable as the enabling components in a large number of radio frequency (RF) devices and systems. For example, MSs can be implanted in filters [31] to improve filtering performances. MSs have also been applied to the engineering of advanced electromagnetic waveguides [32], absorbers [33], and cloaks [34]. In addition, antenna engineers and researchers have adopted MSs in developing cutting-edge antennas. For example, in [35], a bandwidth-enhanced monopole antenna with a metasurface coating was reported. In [36], the functioning of a conformal antenna was improved through the phase compensation offered by a MS. When serving as antenna superstrates, MSs can realize the conversion of an LP input radiation from a feeding antenna to a CP output radiation [37]. In [38], the gain enhancement of a leaky wave antenna was realized by suppressing its spurious radiation through the usage of an MS. In [39], MSs were adopted to realize a conformal holographic antenna. Researchers have also found that the performances of transmit- and reflect-arrays can be improved by MSs [40, 41].

2.1.2 MS-based Artificial Antenna Ground Plane

In antenna engineering, MSs can be implemented as artificial antenna ground planes. In this way, numerous antenna performance enhancements can be realized, including antenna gain improvements [42], bandwidth broadenings [43], side-lobe suppressions [44], radiation efficiency promotions [45], and antenna size reductions [46].

An MS-based artificial ground plane can also be utilized to generate CP radiation from an LP feeding antenna placed above it, as reported in [47]. However, this design suffers from a narrow operational bandwidth. In [48, 49], a couple of MS-based artificial CP antenna designs were reported that have realized broadened operational bandwidths at the expense of increasing overall antenna volumes.

In this chapter, MS-based artificial ground planes are synthesized and implemented in antenna designs to achieve bandwidth-enhanced antennas with low profiles and small footprints. The MS-based artificial ground planes are loaded with properly designed interdigitated capacitors (ICs) and thus are called interdigitated capacitive metasurfaces (ICMSs). Three novel antennas are introduced in this chapter, two of which are LP antennas and one of which provides CP radiation. For the first LP antenna design, the ICs are loaded along one dimension of the MS, leading to a fractional operational bandwidth equal to 15%. The second LP antenna realizes a further antenna size reduction by loading the ICs along both dimensions of the MS. Even with such a miniaturized volume, the second LP antenna still maintains a wide fractional bandwidth equal to 10%. The third proposed antenna is a CP antenna with enhanced axial ratio (AR) bandwidth. The antenna is also enabled by an ICMS artificial ground plane. However, unlike the previous two LP antennas, the CP antenna has an ICMS with ICs in triangular shapes. Moreover, on the top surface of each unit cell, a slot is etched off from the metallic patch along its diagonal line. By virtue of this ICMS, the LP radiation from the feeding antenna is converted into CP radiation. Even with a compact size,

this proposed antenna still possesses a fractional $S_{11} < -10$ dB bandwidth equal to 15.6%, fully covering a fractional AR < 3 dB bandwidth equal to 9.1%.

This chapter is organized as follows. In Section 2.2, the design procedure as well as the simulated and measured performances of the one-dimensional (1D) loaded ICMS artificial ground plane enabled LP antenna are presented. In Section 2.3, the 2D loaded ICMS artificial ground plane based LP antenna is discussed. The ICMS artificial ground plane enabled CP antenna is illustrated in Section 2.4. This chapter is concluded in Section 2.5.

2.2 1D Loaded ICMS Enabled LP Antenna Design

The configuration of the proposed LP antenna with a 1D loaded ICMS artificial ground plane as well as the corresponding coordinate system is shown in Figure 2-1. As can be seen, the proposed antenna consists of two components, *i.e.* a printed planar monopole antenna and a 1D loaded ICMS artificial ground plane. The planar monopole feeding antenna consists of a 50Ω microstrip line and a circularly-shaped patch, both of which are printed on a 1.5 mm-thick Rogers RO3003 laminate with a relative dielectric constant $\epsilon_r = 3$ and a dielectric loss tangent $\tan\delta = 0.001$. Before moving forward, it is worth mentioning that the metallic patch is not always circular. In fact, it can also be rectangular or in other shapes. However, the dimensions of the metallic patch can be tuned to obtain an optimal impedance matching of the integrated antenna. As is later explained, the monopole antenna serves as a feeding component or transducer to excite the ICMS artificial ground plane which is the actual radiator.

The ICMS artificial ground plane is a 3×6 unit cell periodic array printed on a 2.5 mm-thick Rogers RO3003 laminate. The synthesis and analysis of the ICMS unit cell are presented in subsection 2.2.1. As is also illustrated, the ICMS artificial ground plane is similar to a rectangular patch antenna but with engineered dispersion behavior so as to achieve a wide operational band.

The overall footprint of the integrated antenna is $33.0 \times 62.4 \text{ mm}^2$, which is equivalent to an electrical footprint of $0.37\lambda_0^2$, where λ_0 is the free-space wavelength at the center frequency 4.0 GHz and equal to 75mm. The detailed dimensions of the proposed antenna are summarized in Table 2-1.

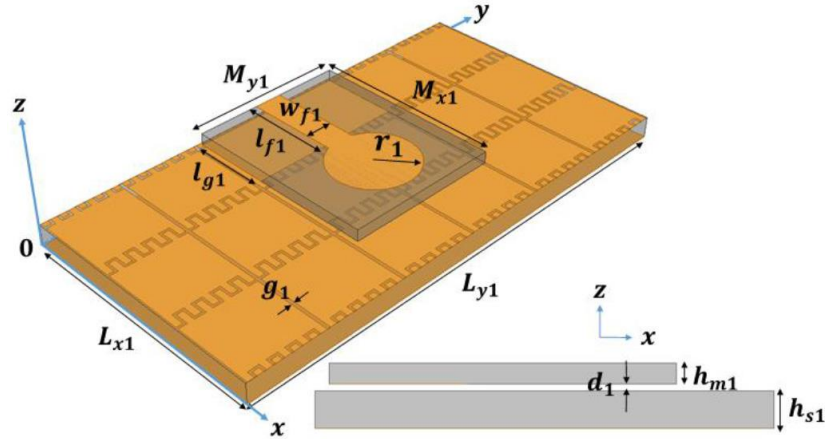


Figure 2-1. 3D configuration and side view of the proposed integrated LP antenna.

Table 2-1. Detailed Dimension of the Proposed 1D Loaded ICMS Based Antenna (all in mm).

M_{x1}	M_{y1}	L_{x1}	L_{y1}	d_1	h_{m1}	h_{s1}	r_1	l_{f1}	w_{f1}	l_{g1}	g_1
25	20	33	62.4	0.5	1.5	2.5	5.5	12.2	3.6	10	0.4

2.2.1 Analysis of the ICMS Unit Cell

In order to investigate the dispersion behavior of the ICMS, numerical simulations of the ICMS unit cell are carried out using HFSS [30], as shown in Figure 2-2. As can be seen, a plane wave with its E -field polarized along the x -axis is normally incident on the unit cell, and periodic boundary conditions (not shown here) are applied to mimic an infinite ICMS. The unit cell consists of an IC loaded patch printed on a grounded Rogers RO3003 laminate. Another unit cell (not shown

here) whose IC loading is replaced by a gap loading on the patch has also been simulated for reference. The equivalent circuit of a single ICMS unit cell is depicted in Figure 2-2(b) with resonant frequency calculated as [24]

$$f_r = \frac{1}{2\pi\sqrt{(L_s+L_d)C_s}} \quad (2-1)$$

In the above equation, L_s and C_s are the equivalent inductance and capacitance of the unit cell, respectively.

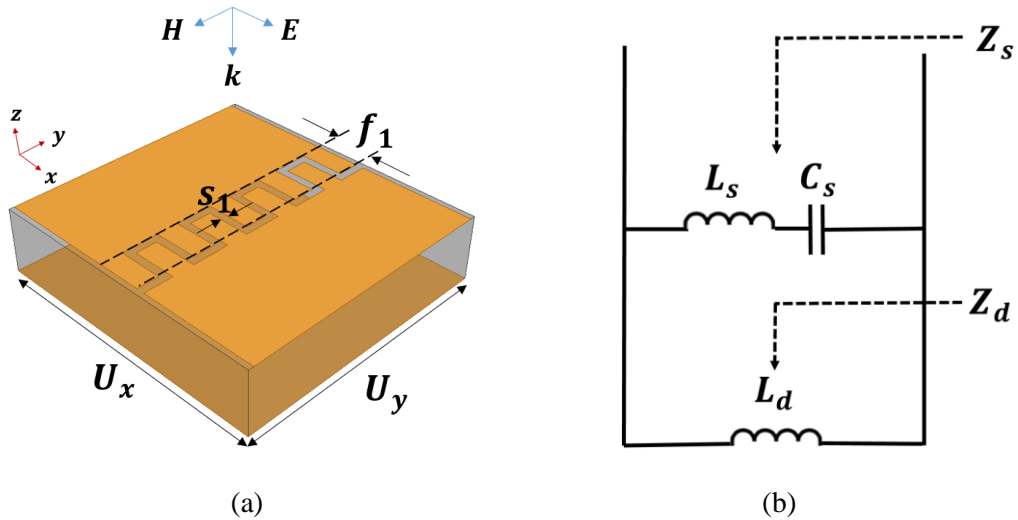


Figure 2-2. (a) HFSS simulation and (b) the equivalent circuit model of an ICMS unit cell.

The simulated reflection phases of a unit cell loaded with and without the IC loading are compared in Figure 2-3(a). As shown, the resonant frequency of a unit cell with IC loading is lower, leading to a smaller electrical size. This size reduction can be explained by Eq. (2-1). Since the capacitance C_s provided by the IC loading is larger than that provided by a gap loading, the numerator on the right-hand side of Eq. (2-1) is larger with the IC loading, resulting in a smaller resonant frequency f_r .

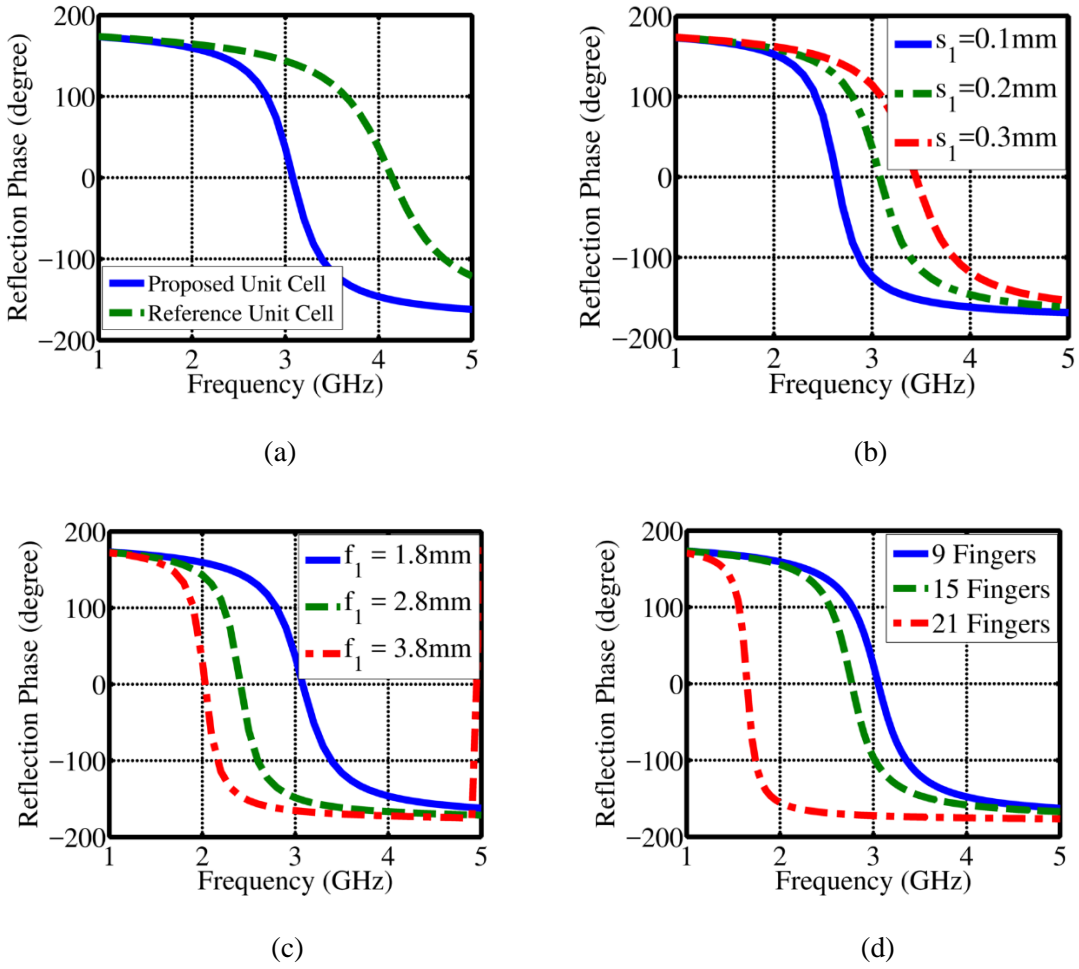


Figure 2-3. (a) Simulated results of unit cells with and without IC loading, and parametric studies on (b) s_1 , (c) f_1 , and (d) the number of fingers.

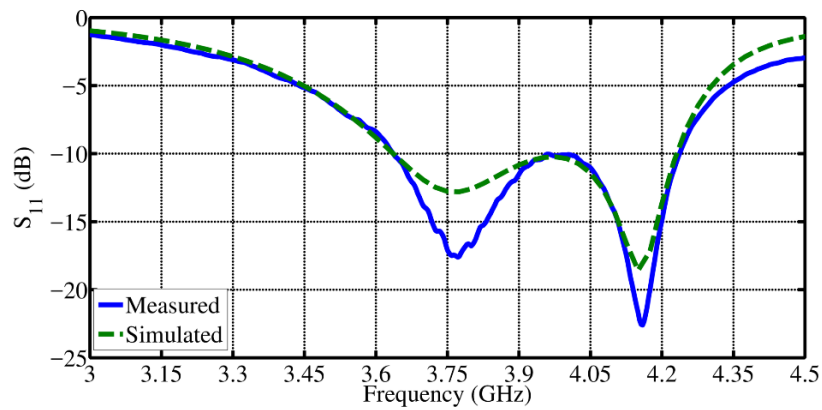
To realize further miniaturization, the resonant frequency must be further decreased while the overall size of the unit cell remains the same. To this end, the denominator of Eq. (2-1) needs to be increased, which possibly can be achieved by increasing either L_d , L_s , or C_s . An increase in L_d results in a larger profile of the unit cell, which should be avoided. On the other hand, a larger L_s and/or L_d causes a narrower operational bandwidth of the unit cell. This is because Eq. (2-1) is equivalent to a serial connected LC resonant circuit with inductance and capacitance equal to $(L_d + L_s)$ and C_s , respectively. An increase in either L_d or L_s , or both, causes the quality-factor of

the resonant circuit to be larger. Hence, efforts are made to increase C_s , which can be realized by tuning the corresponding design parameters of the IC. Parametric studies of finger gap width s_1 , finger length f_1 , and the number of fingers of the IC are carried out and the corresponding results are shown in Figure 2-3(b) to Figure 2-3(d). In summary, a lower resonant frequency can be achieved by decreasing finger gap width, increasing finger length, or introducing more IC fingers. It should be noted that the compromise for achieving a smaller resonant frequency is a narrower fractional bandwidth, defined as the ratio of the frequency range where the reflection phase is between $\pm 90^\circ$ to the resonant frequency f_r . For instance, the fractional bandwidths are 11.3% and 16.2% with resonant frequencies equal to 2.03 and 3.08 GHz, respectively, as shown in Figure 2-3(c). This can be explained by the fact that although adjusting these design parameters mainly increases C_s , it also introduces parasitic inductance. Here, as a compromise between size reduction and bandwidth, a unit cell with 9 fingers that possesses a 0.2 mm finger gap width and a 1.8 mm finger length is adopted for ICMS construction.

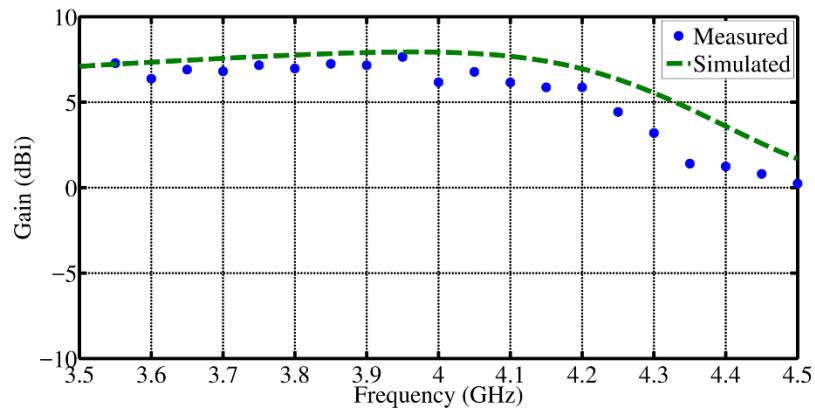
2.2.2 Simulated Antenna Performances

After the finalization of ICMS engineering, a printed planar monopole antenna is designed and placed above the ICMS with a distance $d_1 = 0.5$ mm. It is worth mentioning that an optimal impedance matching of the integrated antenna can be obtained by tuning d_1 . Here, the value of d_1 is obtained through parametric study, which is explained in detail later. It is likewise shown later that a small variance in d_1 only causes an ignorant effect on the overall performances of the integrated antenna. During antenna prototyping, a 0.5 mm-thick foam layer is inserted between the ICMS and the monopole antenna. In addition to d_1 , there are other parameters, including the radius of the circular metallic patch, that can be effectively tuned to obtain an optimal impedance.

The simulated impedance matching performance of the proposed antenna is presented in Figure 2-4(a). As can be clearly seen, two closely located resonances are observed, giving rise to a wide $S_{11} < -10$ dB impedance matching band equal to 600 MHz ranging from 3.63 to 4.23 GHz centered at 3.93 GHz. Equivalently, a fractional bandwidth equal to 15.3% is achieved. Figure 2-4(b) presents the broadside gain performance of the proposed antenna. As can be seen, the gain value varies from 6.67 to 7.94 dBi within the impedance matching band.



(a)



(b)

Figure 2-4. Simulated and measured (a) impedance matching and (b) broadside gain performances of the LP integrated antenna with a 1D loaded ICMS artificial ground plane.

A comparison between Figure 2-4(a) and Figure 2-3 reveals that within the operational band of the integrated antenna, the ICMS artificial ground plane is a capacitive impedance surface. Thus, the impedance matching can be achieved if it is fed by an inductive component so that the imaginary part of the input impedance can be cancelled out. The simulated results of the input impedance of the monopole antenna alone in free space are shown in Figure 2-5. As can be seen, the reactance of the monopole antenna within the operational band of the integrated antenna has a positive value, indicating that the monopole antenna is inductive. Thus, the capacitance of the ICMS is cancelled out by the inductance of the monopole feeding antenna.

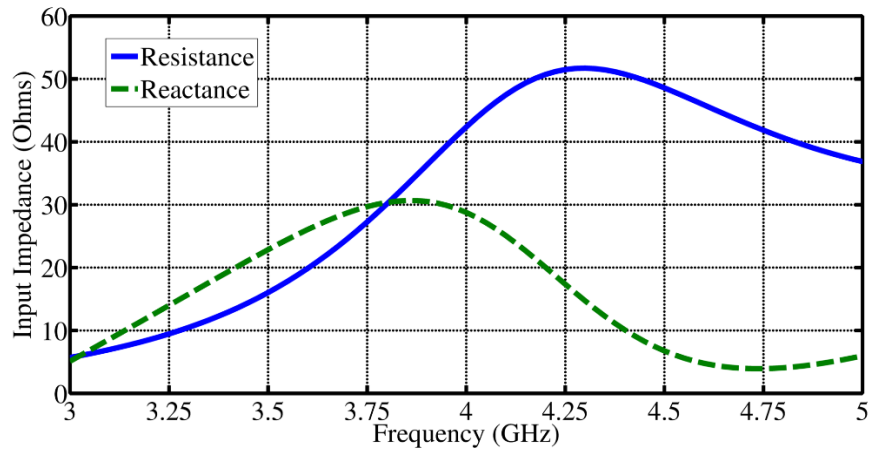


Figure 2-5. Simulated input impedance of the feeding monopole antenna alone in free space.

The simulated radiation patterns of the antenna at three sampling frequency points, 3.8, 4.0, and 4.2 GHz, on the *E*-plane and *H*-plane are presented in Figure 2-6. It is observed that unidirectional radiation patterns with the majority of radiation directed along the broadside are achieved on both planes at all three sampling frequencies. Specifically, the half-power beamwidths (HPBW) at 3.8, 4.0, and 4.2 GHz on the *E*-plane are 84° , 84° , and 83° , respectively. The HPBW at the three frequencies on the *H*-plane are 64° , 60° , and 52° , respectively. Moreover, the back radiations are well suppressed, leading to high front-to-back (FB) ratios above 10 dB for all radiation patterns.

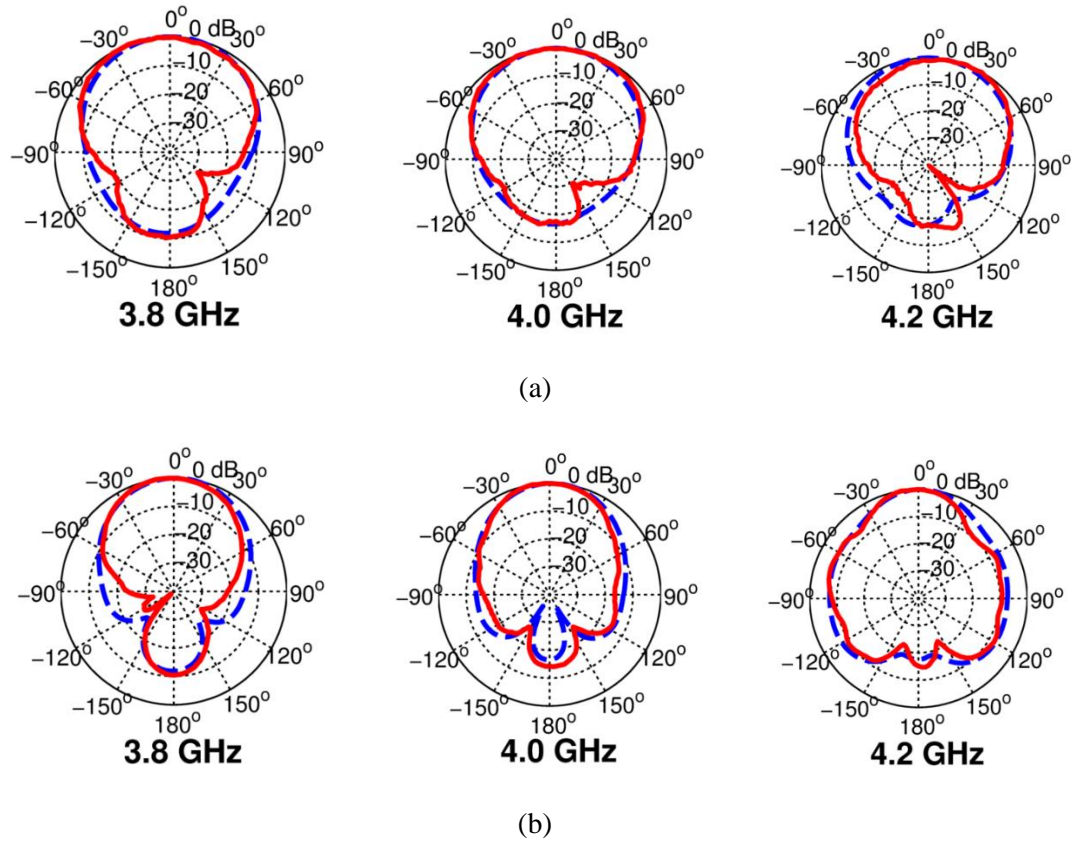
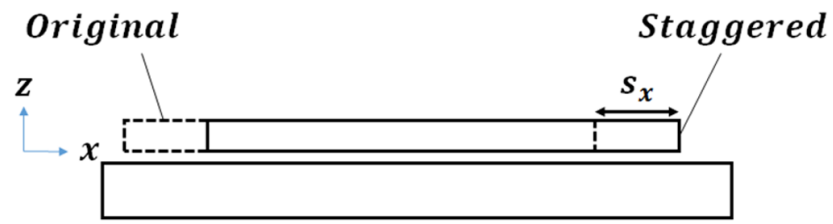
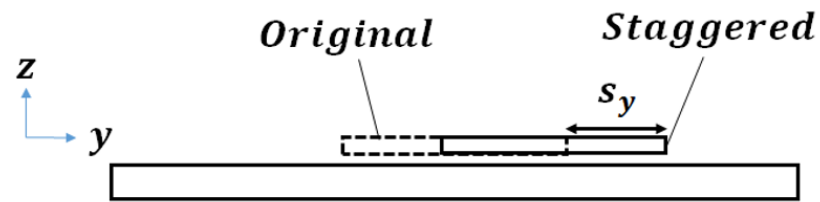


Figure 2-6. Simulated and measured radiation patterns on the (a) E -plane and (b) H -plane (dashed line: simulated; solid line: measured).

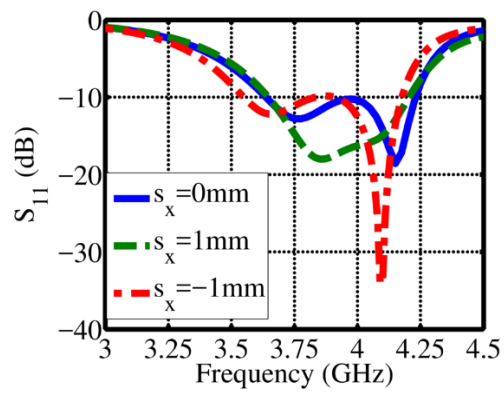
Before closing this section, it is worth investigating the effect of staggering the monopole antenna along the x and y directions (as illustrated in Figure 2-7) on the overall performances of the proposed antenna, as this may happen during antenna assembly. Specifically, shifting the monopole antenna along the x -axis is investigated with s_x equal to 0, 1, and 2 mm. On the other hand, shifting along the y -axis is investigated with s_y equal to 0 and $\frac{U_y}{4}$. The corresponding simulated impedance matching and antenna gain performances are shown in Figure 2-8. The results reveal that a small amount of staggering of the monopole antenna along the x -axis or y -axis causes only a minor effect on the overall performances of the integrated antenna.



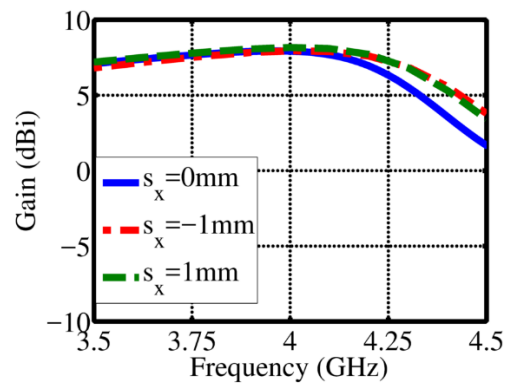
(a)



(b)

Figure 2-7. Scenarios where the monopole antenna is shifted along the (a) x and (b) y directions.

(a)



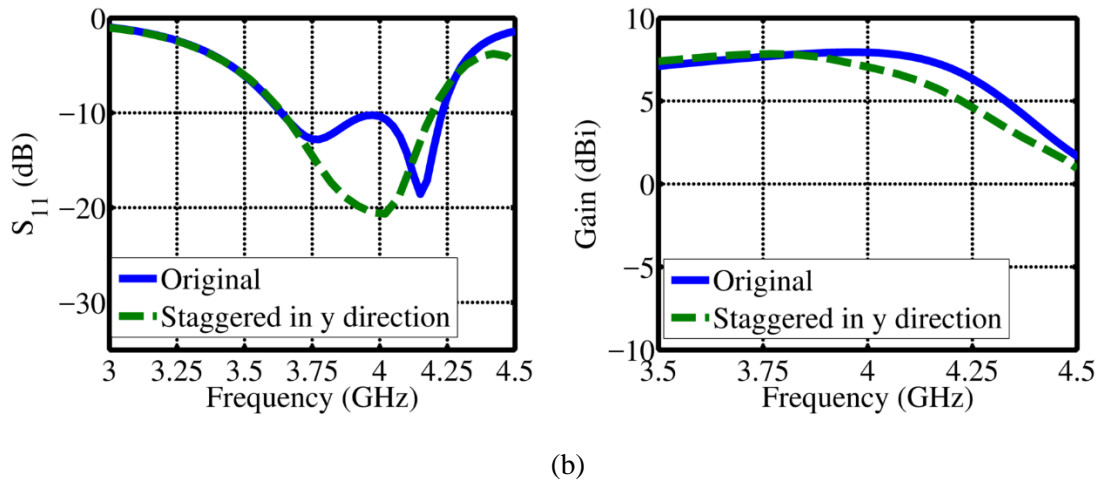


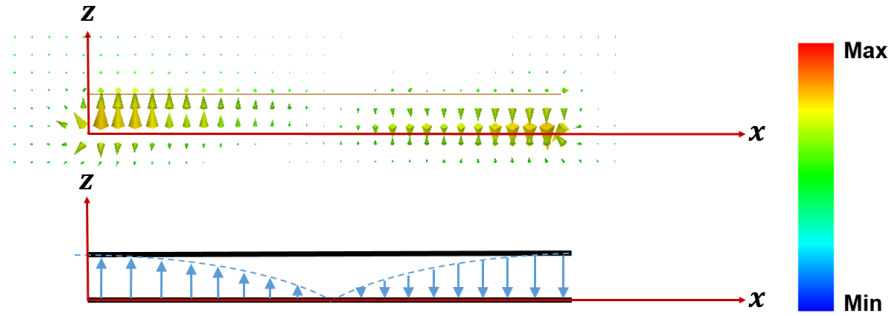
Figure 2-8. Simulated impedance matching and gain performances with the monopole antenna staggered along the (a) x and (b) y directions.

2.2.3 Antenna Working Principles

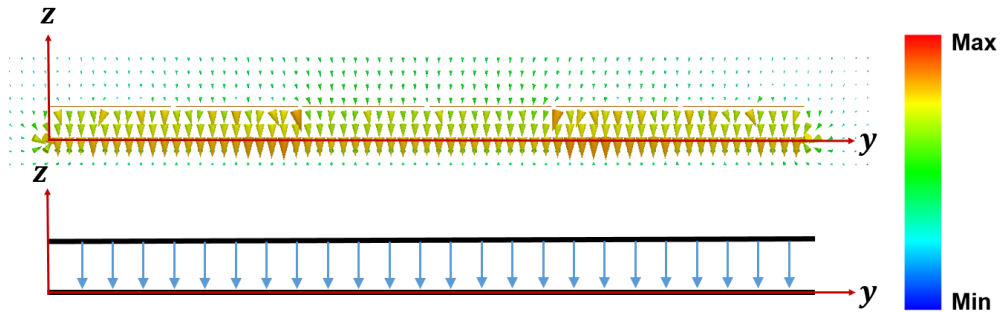
As mentioned in previous sections, the ICMS in the proposed integrated antenna serves as the main radiator, operating similarly to a rectangular patch antenna but with modified dispersion behavior. In the following figures, the E -field distributions within the ICMS when excited by the feeding monopole antenna and the E -field distributions within a conventional rectangular patch antenna are compared for illustration.

The simulated E -field distributions on the $y = 0$ and $x = 33$ mm planes (see Figure 2-1 for the two planes) at 3.75 GHz are shown in Figure 2-9(a) and Figure 2-9(b), respectively. The E -field distributions on the $y = 0$ and $x = 33$ mm planes at 4.20 GHz are illustrated in Figure 2-10(a) and Figure 2-10(b), respectively. For reference, the sketched E -field distributions of a conventional rectangular patch antenna operating in its TM_{10} and TM_{12} modes are also plotted based on the classical cavity model [11]. It can be seen that the E -field distributions of the proposed antenna working at 2.35 and 2.40 GHz are almost the same as those of a conventional rectangular patch antenna operating in its TM_{10} and TM_{12} modes, respectively. The minor differences are the field

enhancements on the top surface of the ICMS where the ICs exist. For differentiation, the corresponding two modes of the ICMS artificial ground plane are denoted as the ICMS- TM_{10} and ICMS- TM_{12} modes, respectively, in the rest of this chapter.

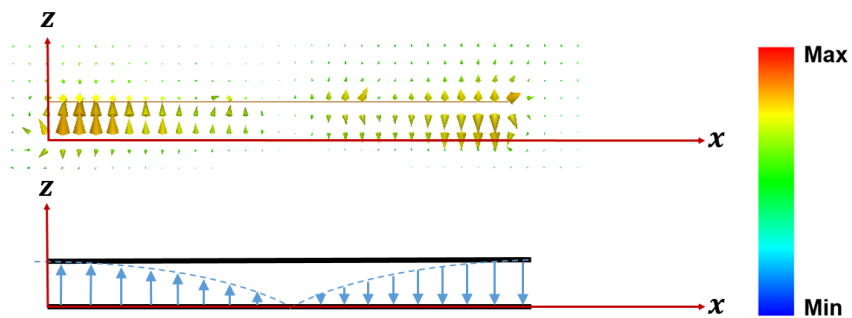


(a)



(b)

Figure 2-9. Simulated and sketched E -field distributions on the (a) $y = 0$ and (b) $x = 33$ mm planes at 3.75 GHz.



(a)

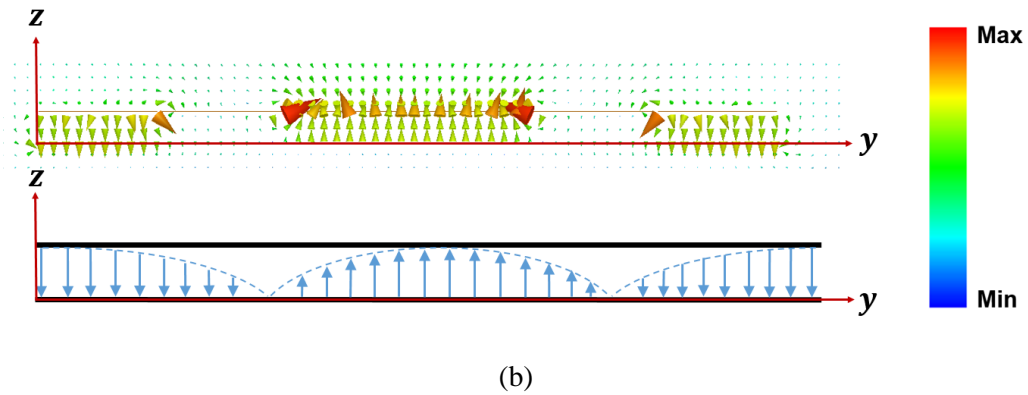


Figure 2-10. Simulated and sketched E -field distributions on the (a) $y = 0$ and (b) $x = 33$ mm planes at 4.20 GHz.

The frequency ratio of resonant frequencies of the TM_{10} and TM_{12} modes of a conventional rectangular patch antenna is always very large and the two frequencies can barely be tuned to be close to each other to offer a wide operation band. However, the ICMS- TM_{10} and ICMS- TM_{12} modes of the proposed ICMS artificial ground plane-based antenna are merged together to form a wide operational band. This mode-merging phenomenon can be attributed to the modified dispersion behavior of the proposed ICMS artificial ground plane. For illustration, the dispersion relations of the ICMS operating in the ICMS- TM_{10} and ICMS- TM_{12} modes are simulated using the eigenmode solver of HFSS. The corresponding simulation model is shown in Figure 2-11(a). To model the open space above the ICMS, an air box top-hatted with a perfect matching layer (PML) is built above the unit cell. Then, a larger air box is constructed to enclose all the structures. Finally, periodic boundaries are applied to the corresponding four facets of the second air box to realize the infinity of the ICMS along the x - and y -directions. The dispersion curves for the ICMS- TM_{10} and ICMS- TM_{12} modes are shown in Figure 2-11(b). The horizontal axis labeled as p_x (p_y) represents the phase delay provided by a single unit cell along the x -(y -) axis, and the vertical axis indicates the frequency. For the occurrence of the ICMS- TM_{10} resonant mode, the following conditions must be satisfied:

$$N_x \times p_x = 180^\circ \quad (2-2a)$$

$$N_y \times p_y = 0^\circ \quad (2-2b)$$

where N_x and N_y indicate the number of unit cells in the ICMS along the x - and y -axes and equal 3 and 6, respectively. Thus, in the simulation for the ICMS- TM_{10} mode, p_y is pre-defined to be 0 and a parametric sweep on p_x is carried out. In addition, according to Eq. (2-2a), the resonance occurs when p_x is equal to 60° . Hence, based on Figure 2-11(b), the predicted resonant frequency of the ICMS- TM_{10} mode is 3.75 GHz, which agrees well with the first resonance of the integrated antenna observed in Figure 2-4(a). On the other hand, for the occurrence of the ICMS- TM_{12} resonant mode, the following conditions must be satisfied:

$$N_x \times p_x = 180^\circ \quad (2-3a)$$

$$N_y \times p_y = 360^\circ \quad (2-3b)$$

Thus, in the simulation for the ICMS- TM_{12} mode, p_x is pre-defined to be 60° and a parametric sweep of p_y is carried out. In addition, according to Eq. (2-3b), the resonance occurs when p_y is equal to 60° . Hence, based on Figure 2-11(b), the predicted resonant frequency of the ICMS- TM_{12} mode is 4.30 GHz, which agrees well with the second resonance of the integrated antenna observed in Figure 2-4(a). In summary, the ICMS- TM_{10} and ICMS- TM_{12} modes correspond well with the TM_{10} and TM_{12} modes of a conventional rectangular patch antenna based on the classical cavity model. Moreover, because the ICMS- TM_{10} and ICMS- TM_{12} modes are closely oriented in the frequency domain, they are merged together to form a wide operational band.

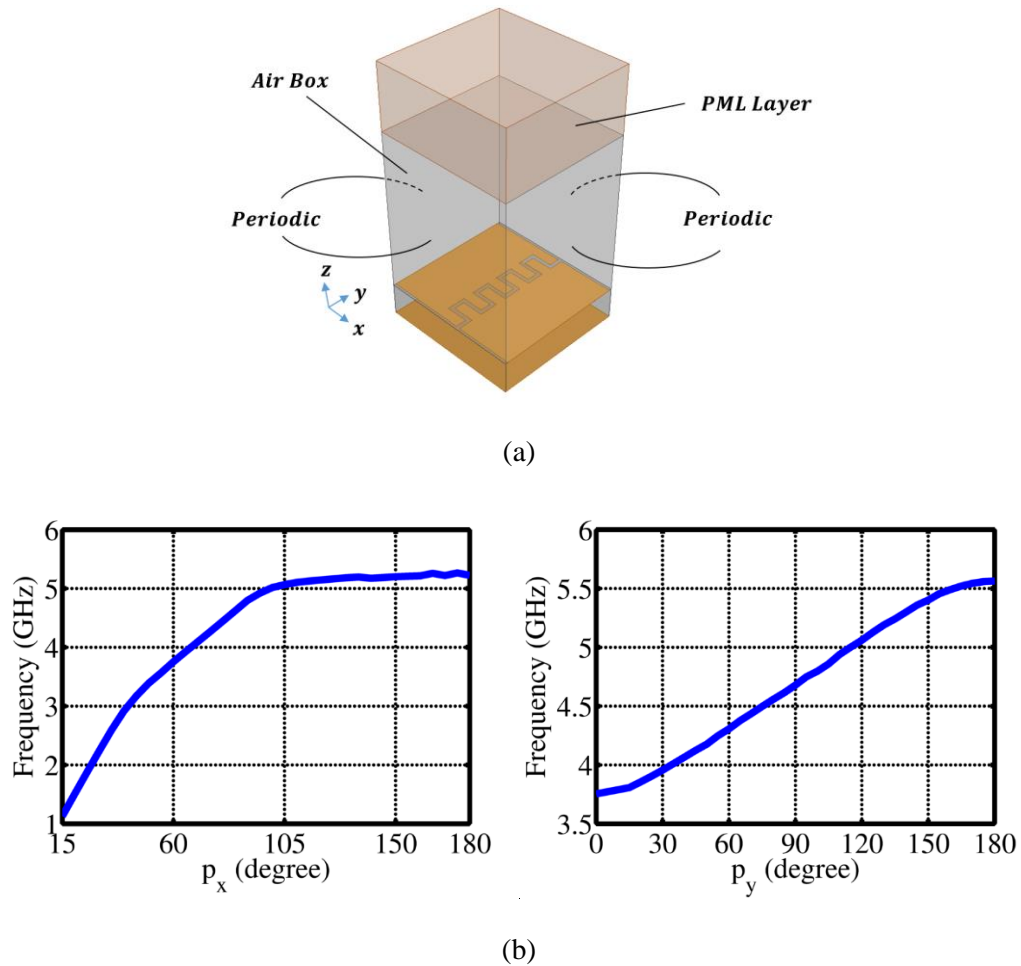
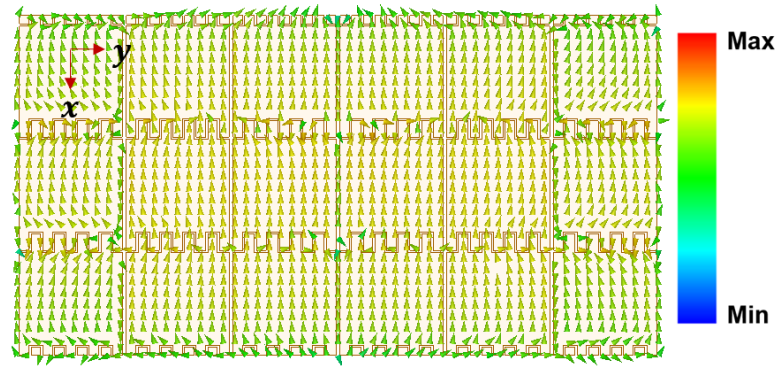


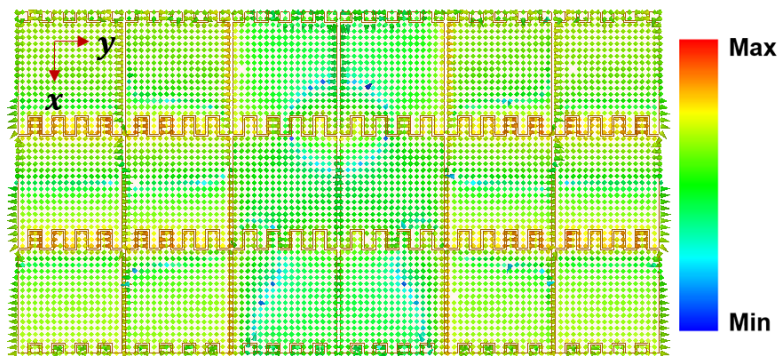
Figure 2-11. (a) Simulation setup and (b) dispersion curves of the ICMS- TM_{10} (left) and ICMS- TM_{12} (right) modes.

While a patch antenna working under the TM_{10} mode provides unidirectional radiation along the broadside, it provides a bi-directional shaped radiation pattern with a null along the broadside when working under the TM_{12} mode. However, the radiation patterns shown in Figure 2-6 indicate that the ICMS- TM_{12} mode still offers a unidirectional pattern with maximal radiation along the broadside. Here, a detailed explanation can be given as follows. In the first place, as shown in Figure 2-12(a), the currents on the top surface of the ICMS are mostly aligned along the x -axis. This behavior is different from the current distribution of a conventional rectangular patch antenna operating in its TM_{12} mode and thus provides unidirectional radiations at far-field with the

E -field polarized along the x -axis. On the other hand, as plotted in Figure 2-12(b), the E -field is enhanced along the meandered gap of ICs, resulting in a strong magnetic current along the y -axis. These magnetic currents also contribute to the maximal radiation along the broadside.



(a)



(b)

Figure 2-12. Simulated (a) current and (b) E -field distributions on the top surface of the ICMS artificial ground plane at 4.20 GHz.

2.2.4 Experimental Results

To experimentally verify the proposed 1D loaded ICMS artificial ground plane enabled integrated antenna design, an antenna prototype is fabricated, assembled, and measured. The antenna prototype is shown in Figure 2-13.



Figure 2-13. Antenna prototype of the 1D loaded ICMS artificial ground plane enabled integrated antenna.

Figure 2-4(a) shows the measured impedance matching performance of the proposed antenna as a solid S_{11} curve. A good agreement between the simulated and measured results is obtained. Specifically, the measured $S_{11} < -10$ dB bandwidth is 600 MHz ranging from 3.63 GHz to 4.23 GHz, which is equivalent to a fractional bandwidth of 15.3%.

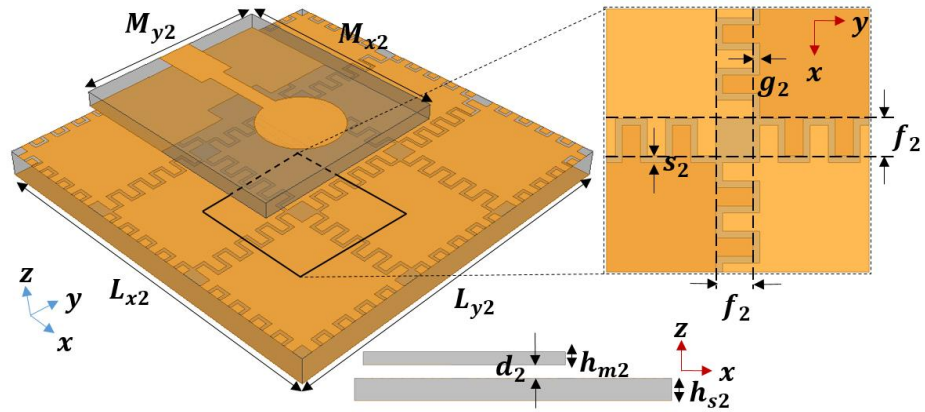
Figure 2-4(b) shows the measured gain profile of the proposed antenna indicated by solid dots. As can be seen, the measured gain varies from 5.8 to 7.5 dBi, with the peak gain occurring at 3.95 GHz.

Figure 2-5 illustrates the measured radiation patterns at 3.8, 4.0, and 4.2 GHz on both the E -plane and H -plane as solid red curves. The measured HPBW_s at 3.8 GHz are 98° and 60° on the E -plane and H -plane, respectively. At 4.0 GHz, the HPBW_s are 101° and 56° on the E -plane and H -plane, respectively. The measured HPBW_s at 4.2 GHz are 72° and 45° on the E -plane and H -plane, respectively. It can be clearly observed that the HPBW has larger values on the E -plane at all three sampling frequencies. This is because the proposed integrated antenna has a smaller dimension on the E -plane.

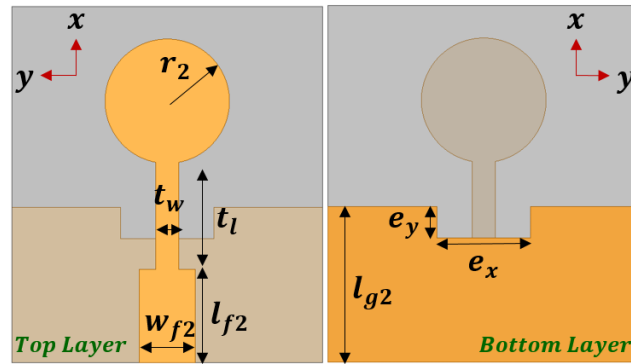
2.3 2D Loaded ICMS Enabled LP Antenna Design

In order to realize further antenna volume miniaturization, a 2D loaded ICMS artificial ground plane is designed in this section. The proposed 2D loaded ICMS artificial ground plane possesses additional ICs along the y -axis. By virtue of these extra ICs, the ICMS consists only of 3×3 unit cells, leading to a significant antenna footprint reduction. Moreover, both the simulated and measured results show that the miniaturized antenna still provides a wide operational band with unidirectional radiation patterns. The effect of the extra ICs is illustrated through a parametric study.

Figure 2-14(a) and Figure 2-14(b) illustrate the configurations of the proposed 2D loaded ICMS and the monopole antenna, respectively. The detailed dimensions are summarized in Table 2-2. As can be seen from Figure 2-14(a), only 3×3 unit cells are adopted to construct the ICMS. The monopole antenna is also different from the one used in the 1D loaded ICMS design presented in Section 2.2. As shown in Figure 2-14(b), stepped sections are introduced to the microstrip line. Moreover, a rectangular notch is etched off from the ground plane. These modifications introduce additional flexibility to obtain an optimal input impedance matching of the proposed integrated antenna. The monopole antenna is printed on a 1.5 mm-thick Rogers RO3003 laminate and the ICMS is printed on a 2.5 mm-thick Rogers RO3003 laminate. The overall thickness of the proposed antenna is 5.5 mm and the overall footprint is $36 \times 36 \text{ mm}^2$, which is equivalent to an electrical footprint of $0.23\lambda_0^2$. This is only 64% of the footprint of the antenna proposed in the previous section. It should be noted that λ_0 is the wavelength at 4.0 GHz in free space.



(a)



(b)

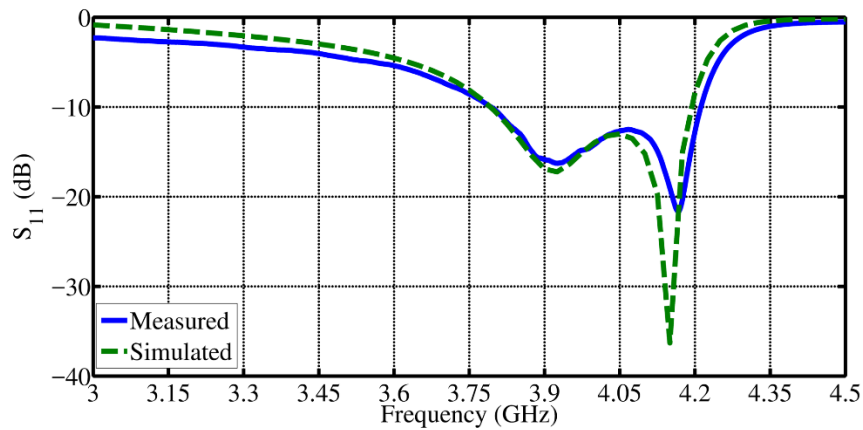
Figure 2-14. Configurations of (a) the 2D loaded ICMS and (b) the monopole antenna.

Table 2-2. Detailed Dimensions of the Proposed 2D Loaded ICMS Enabled LP Antenna (all in mm).

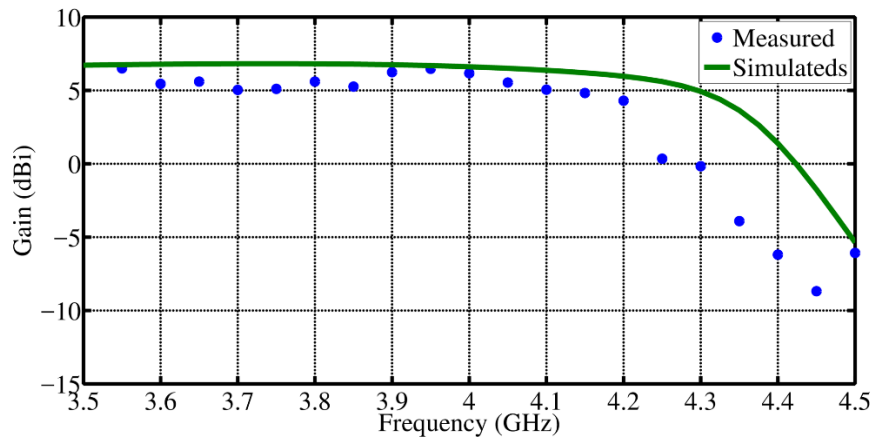
M_{x2}	M_{y2}	L_{x2}	L_{y2}	d_2	h_{m2}	h_{s2}	r_2	l_{f2}	w_{f2}	l_{g2}	g_2
25	20	33	62.4	1.5	1.5	2.5	5.5	12.2	3.6	10	0.4
t_l	t_w	e_x	e_y	l_{p2}	s_2	f_2					
6.9	1.5	2	6	10	0.18	1.92					

2.3.1 Simulated Antenna Performances

Figure 2-15(a) shows the simulated impedance matching performance of the proposed 2D loaded ICMS enabled LP antenna, as indicated by the dashed S_{11} curve. As can be clearly seen, two closely located resonances are observed; these form a wide $S_{11} < -10$ dB band despite the significant antenna miniaturization. Specifically, a 400 MHz bandwidth is achieved from 3.79 GHz to 4.19 GHz, resulting in a fractional bandwidth equal to 10.0%. The simulated gain profile is depicted in Figure 2-15(b). As shown, within the $S_{11} < -10$ dB operational band, the antenna gain is above 6 dBi, with the peak gain equal to 6.8 dBi.



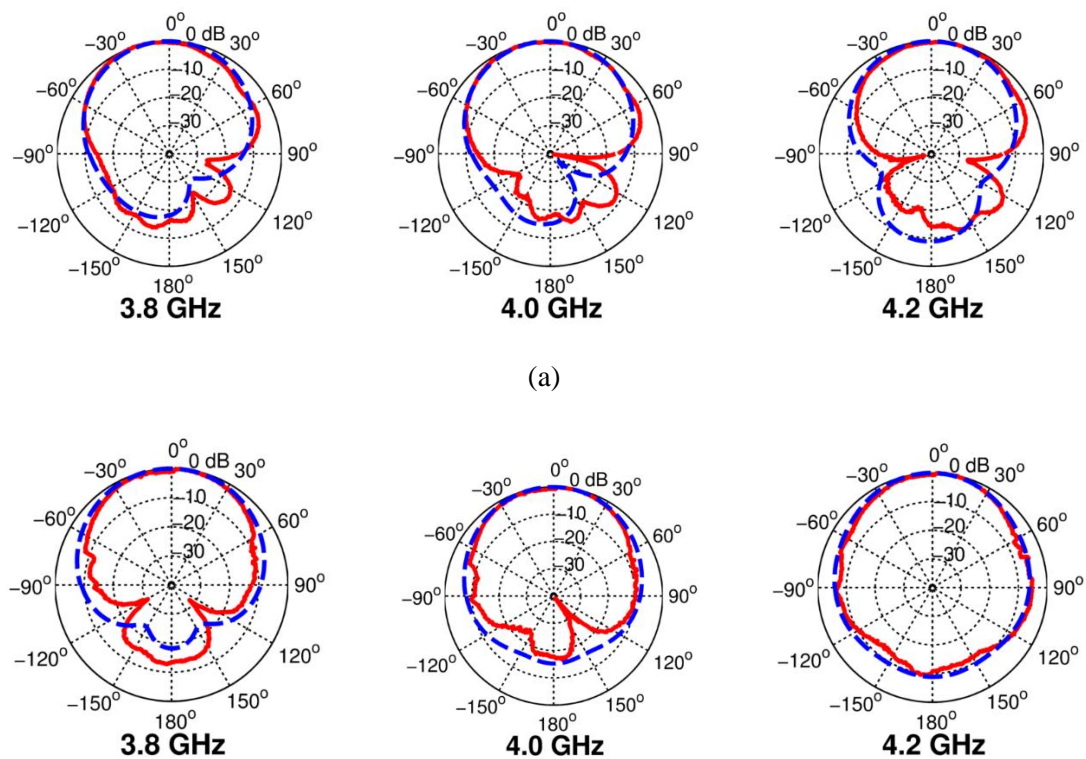
(a)



(b)

Figure 2-15. Simulated (a) impedance matching and (b) gain profile of the 2D loaded ICMS enabled LP antenna.

Figure 2-16 shows the simulated radiation patterns on both the E -plane and H -plane as dashed curves. Again, the three sampling frequencies are chosen to be 3.8, 4.0, and 4.2 GHz. At 3.8 GHz, the simulated HPBWs are 82° and 96° on the E -plane and H -plane, respectively. At 4.0 GHz, the simulated HPBWs are 82° and 92° on the E -plane and H -plane, respectively. At 4.2 GHz, the simulated HPBWs are 81° and 84° on the E -plane and H -plane, respectively. Comparing the HPBWs of the proposed antenna in this section with those in Section 2.2, it can be clearly seen that the 2D loaded ICMS enabled antenna achieves more balanced HPBWs on the E -plane and H -plane. Specifically, the HPBWs on the H -plane of the 2D loaded ICMS enabled antenna are larger than those of the 1D loaded ICMS enabled antenna. This is because the 2D loaded ICMS has a smaller size on the H -plane. In addition, the FB ratios of the simulated radiation patterns remain at high levels above 10 dB, indicating that the back radiations are well suppressed.

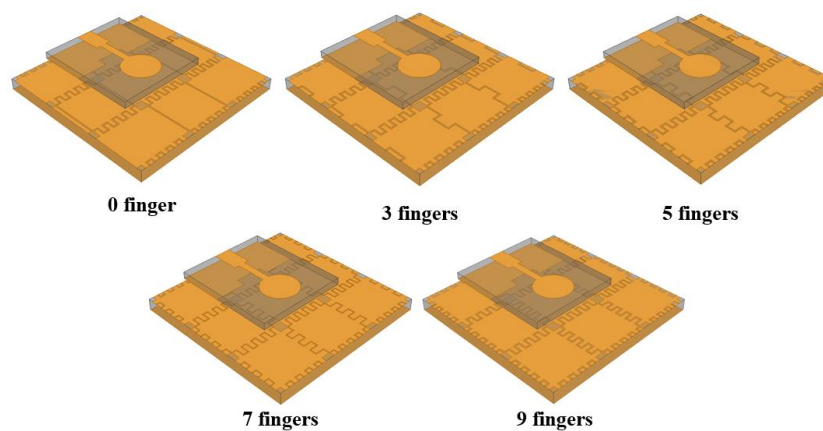


(b)

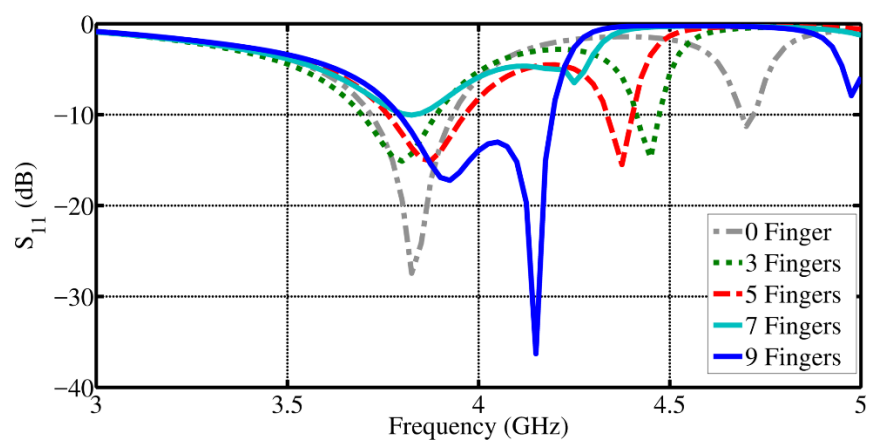
Figure 2-16. Simulated and measured radiation patterns on the (a) *E*-plane and (b) *H*-plane (dashed line: simulated; solid line: measured).

2.3.2 Parametric Study of the ICs along the *y*-axis

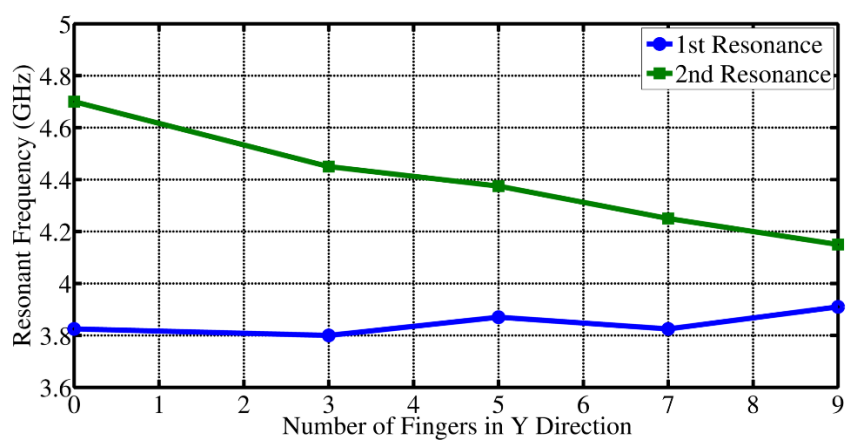
To investigate the effect of extra ICs along the *y*-axis, a parametric study of the number of fingers of the extra ICs is carried out. Five integrated antennas are included in the parametric study, as shown in Figure 2-17(a). The five ICMS artificial ground planes consist of unit cells with varying numbers of IC fingers along the *y*-axis. The simulated S_{11} performances of these five antennas are shown in Figure 2-17(b). It can be seen that extra ICs along the *y*-axis have a minor effect on the first resonance. In other words, the first resonant frequency remains almost the same among the five antennas. In terms of the second resonant frequency, it varies from 4.70 GHz to 4.15 GHz when the number of fingers of an IC in a single unit cell along the *y*-axis is increased from 0 to 9. Figure 2-17(c) summarizes the first and second resonant frequencies of the five integrated antennas. In conclusion, two operational bands with narrow bandwidth are obtained when the two resonances are separated from each other. However, a wide $S_{11} < -10$ dB operational band can be achieved when the two resonances are sufficiently close to each other. Thus, the extra ICs along the *y*-axis can tune the location of the second resonant frequency by adjusting the fingers of the ICs.



(a)



(b)



(c)

Figure 2-17. (a) Integrated antennas enabled by an ICMS artificial ground plane that contains extra ICs with different numbers of fingers along the y -axis, (b) simulated S_{11} of the antennas, and (c) resonant frequencies with varying numbers of fingers of ICs along the y -axis.

2.3.3 Experimental Results

To experimentally verify the proposed 2D loaded ICMS artificial ground plane enabled integrated antenna design, an antenna prototype is fabricated, assembled, and measured. The antenna prototype is shown in Figure 2-18. It should be noted that a 1.5 mm-thick foam is inserted between the monopole antenna and the ICMS to fix the distance between them.

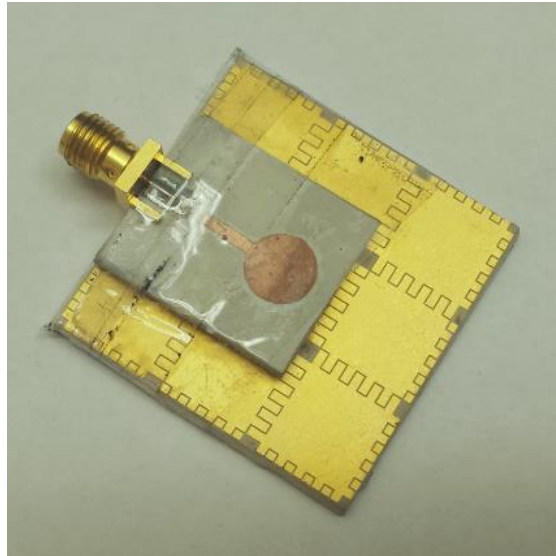


Figure 2-18. Antenna prototype of the 1D loaded ICMS enabled integrated antenna design.

Figure 2-15(a) shows the measured impedance matching performance of the proposed antenna as a solid S_{11} curve. A good agreement between the simulated and measured results is obtained. The measured $S_{11} < -10$ dB bandwidth is 420 MHz ranging from 3.79 to 4.21 GHz, which is equivalent to a fractional bandwidth of 10.5%.

Figure 2-15(b) shows the measured gain profile of the proposed antenna as solid dots. As can be seen, the measured gain varies from 5.0 to 6.2 dBi, with the peak gain occurring at 3.95 GHz.

Figure 2-16 illustrates the measured results of the radiation patterns at 3.8, 4.0, and 4.2 GHz on both the *E*-plane and *H*-plane as solid red curves. The measured HPBWs at 3.8 GHz are 76° and 76° on the *E*-plane and *H*-plane, respectively. The measured HPBWs at 4.0 GHz are 83° and 82° on the *E*-plane and *H*-plane, respectively. The measured HPBWs at 4.2 GHz are 81° and 72° on the *E*-plane and *H*-plane, respectively. Because the proposed antenna has the same dimensions on *x*-axis and *y*-axis, the HPBWs on the *E*-plane and *H*-plane are almost the same.

2.4 ICMS Enabled CP Antenna Design

In Section 2.2 and Section 2.3, the design methodology of two ICMS enabled LP antennas was introduced. In this section, the design of an ICMS enabled CP antenna with enhanced axial ratio (AR) bandwidth and a small form factor is presented. Compared with LP antennas, CP antennas have numerous advantages. For example, the multi-path interference commonly seen in modern communication systems can be mitigated by CP antennas.

Figure 2-19 shows the configuration of the ICMS enabled CP antenna. As can be seen, the CP antenna has a similar configuration to that of the previous two LP antennas, with a monopole antenna placed above an ICMS artificial ground plane. The ICMS unit cell has a diagonal slot cut into the patch and triangular IC fingers are introduced to provide CP radiations at far-field. The overall footprint of the proposed integrated antenna is $45.7 \times 39.3 \text{ mm}^2$, which is equivalent to an electrical footprint of $0.32\lambda_0^2$, where λ_0 is equal to 75 mm. Both the monopole antenna and the ICMS are printed on Rogers RO3003 laminates with a dielectric constant $\epsilon_r=3$ and a loss tangent $\tan\delta=0.001$. The thickness of the monopole antenna is 1.5 mm and the thickness of the ICMS layer

is 2.5 mm. The overall thickness of the antenna is 5.5 mm. Detailed dimensions are summarized in Table 2-3.

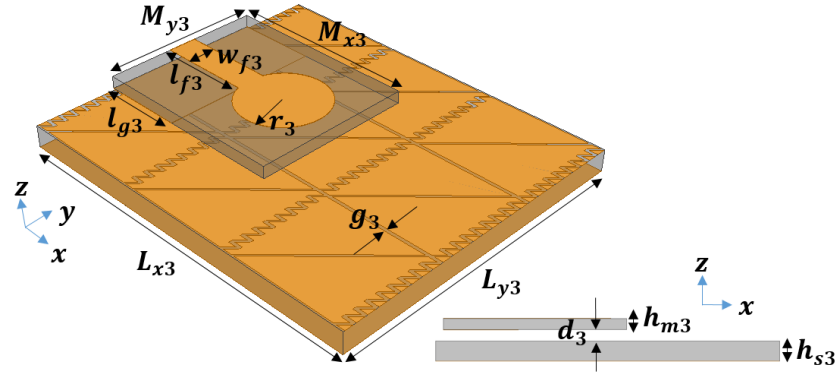


Figure 2-19. Configuration of the ICMS enabled CP antenna design.

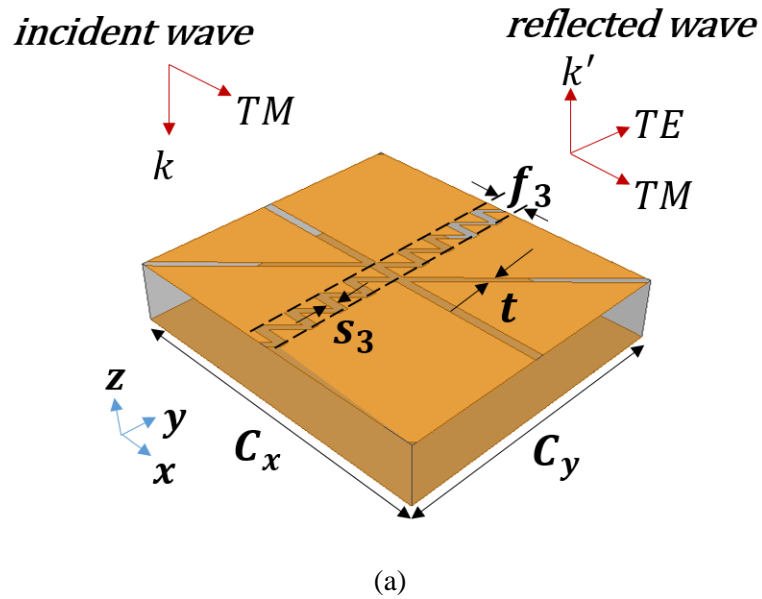
Table 2-3. Detailed Dimensions of the Proposed ICMS Based CP Antenna (all in mm).

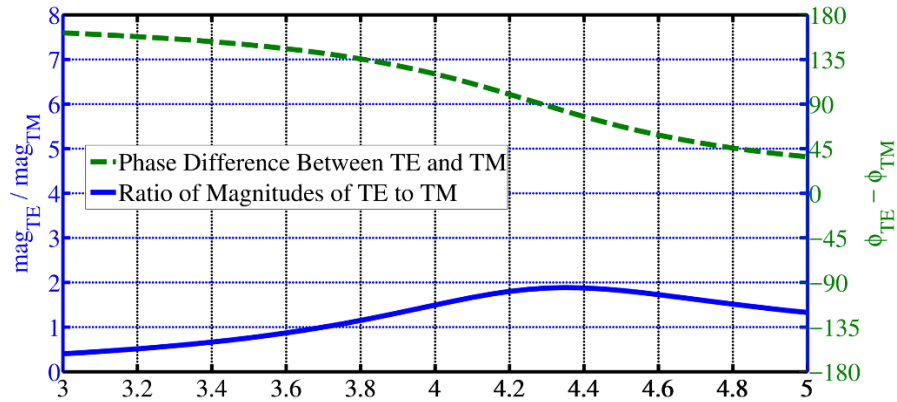
M_{x3}	M_{y3}	L_{x3}	L_{y3}	d_3	h_{m3}	h_{s3}	r_3	l_{f3}	w_{f3}	l_{g3}	g_3
24.3	20	45.7	39.3	1.5	1.5	2.5	5.5	6.9	3.6	10	0.4

2.4.1 Analysis of ICMS Unit Cell

The goal of introducing the diagonal slot and triangular IC fingers is to generate two orthogonal modes when the ICMS is illuminated by an incident LP plane wave, as shown in Figure 2-20(a). Basically, a TM plane wave with its E -field polarized along the x -axis is normally incident on the ICMS unit cell. Both the TM and transverse electric (TE) (E -field polarized along the y -axis) reflected waves are generated. Thus, the broadside radiation of the ICMS integrated antenna is the combination of the TM plane wave radiated by the monopole antenna and the TM and TE plane waves reflected by the ICMS. Hence, the broadside radiation contains both the TM and TE modes. If the two orthogonal modes have the same magnitude and 90° phase difference, a broadside CP radiation can be obtained at far-field. To this end, the unit cell design parameters shown in Figure

2-20(a) are optimized and their values are listed in Table 2-4. The simulated magnitude ratio of and phase difference between the TE and TM modes in the total broadside radiation are presented in Figure 2-20(b). Here, an assumption is made that the magnitude of the directly radiated TM mode is the same as that of the total reflected wave due to the bi-directional radiating characteristic of the monopole antenna. In addition, there is no phase difference between the directly radiated TM mode and the reflected TM and TE waves since the distance between the monopole antenna and the ICMS is very small compared to the wavelength. As can be seen from the simulated results, the frequency range is from 3.9 GHz to 4.3 GHz, where the magnitude ratio of TE to TM waves is kept at nearly unity and their phase difference is almost 90° . Intuitively, CP radiation along the broadside is predicted within this frequency range. It is also observed from Figure 2-20(b) that the TM mode is 90° behind the TE mode, leading to a right-handed circular polarization (RHCP).





(b)

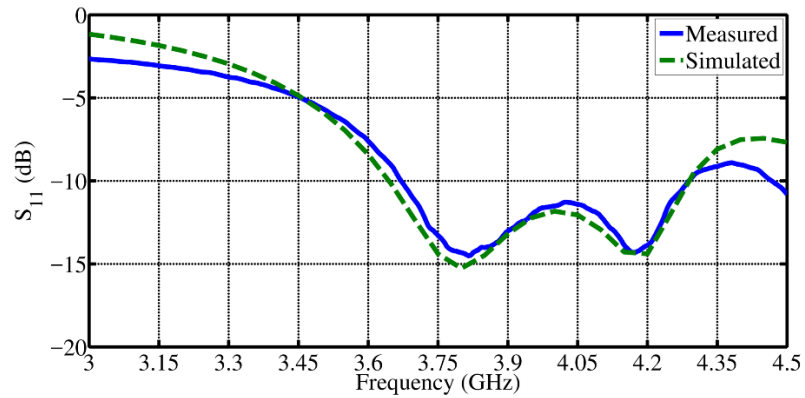
Figure 2-20. (a) Simulation model and (b) simulated ratio of magnitudes of TE to TM modes and phase difference between TE and TM modes.

Table 2-4. Optimized Design Parameters of the ICMS Unit Cell (all in mm).

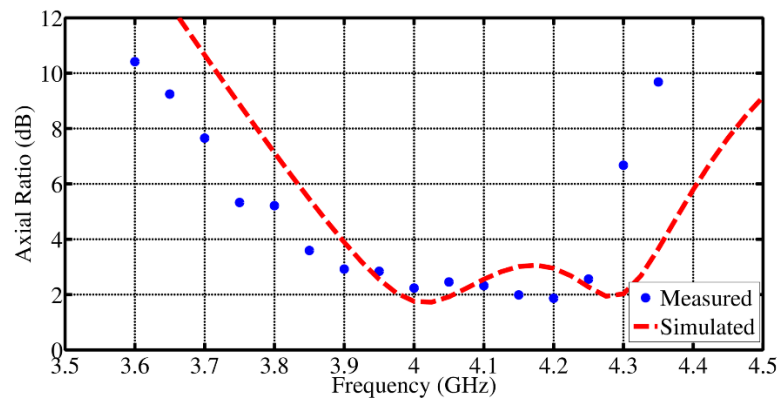
C_x	C_y	s_3	f_3	t
14.8	13.1	0.4	1.5	0.4

2.4.2 Simulated Antenna Performances

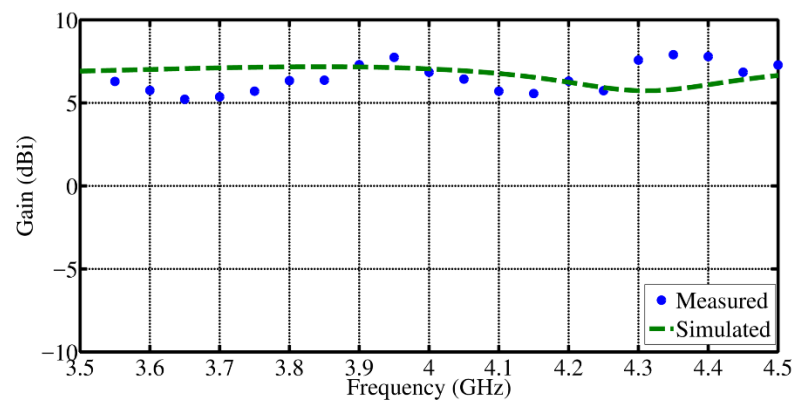
Figure 2-21(a) shows the simulated impedance matching performance of the proposed ICMS enabled CP antenna, as indicated by the dashed S_{11} curve. A 650 MHz bandwidth is achieved from 3.64 GHz to 4.29 GHz, resulting in a fractional bandwidth equal to 16.4%. The simulated broadside AR of the proposed CP antenna is depicted in Figure 2-21(b). As can be seen, a 400 MHz AR < 3dB band is achieved from 3.93 GHz to 4.33 GHz, resulting in a fractional bandwidth equal to 9.7%. It is observed that the $S_{11} < -10$ dB frequency band fully covers the AR < 3 dB frequency band. Thus, the operational band of the proposed CP antenna is the same as the AR < 3 dB band. As shown in Figure 2-21(c), within the operational frequency range, the antenna gain is above 5.5 dBi, with the peak gain equal to 7.0 dBi at 3.9 GHz.



(a)



(b)



(c)

Figure 2-21. Simulated and measured (a) impedance matching, (b) broadside AR, and (c) gain performances of the ICMS enabled CP antenna.

Figure 2-22 shows the simulated radiation patterns on both the xoz -plane and yoz -plane as dashed curves. The three sampling frequencies are chosen to be 3.8, 4.0, and 4.2 GHz. At 3.8 GHz, the simulated HPBWs are 77° and 88° on the xoz -plane and yoz -plane, respectively. At 4.0 GHz, the simulated HPBWs are 81° and 86° on the xoz -plane and yoz -plane, respectively. At 4.2 GHz, the simulated HPBWs are 89° and 87° on the xoz -plane and yoz -plane, respectively. In addition, the FB ratios of the simulated radiation patterns remain above 15 dB, indicating that the back radiations are well suppressed.

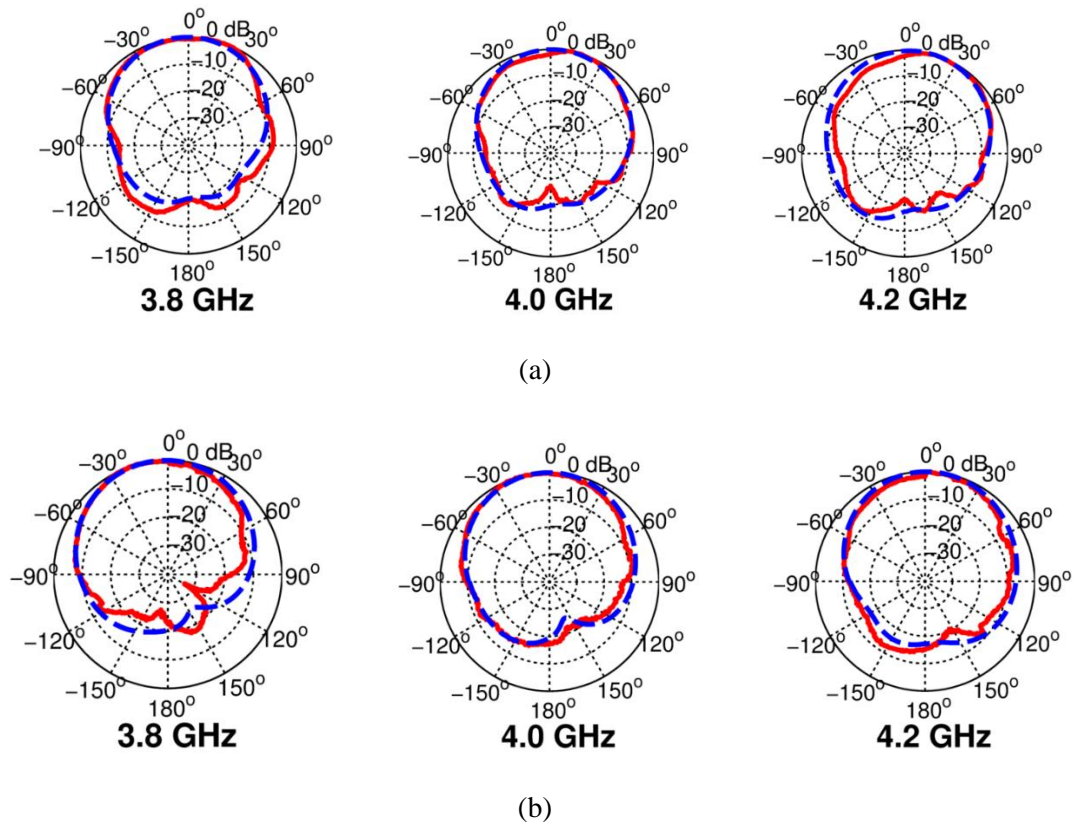
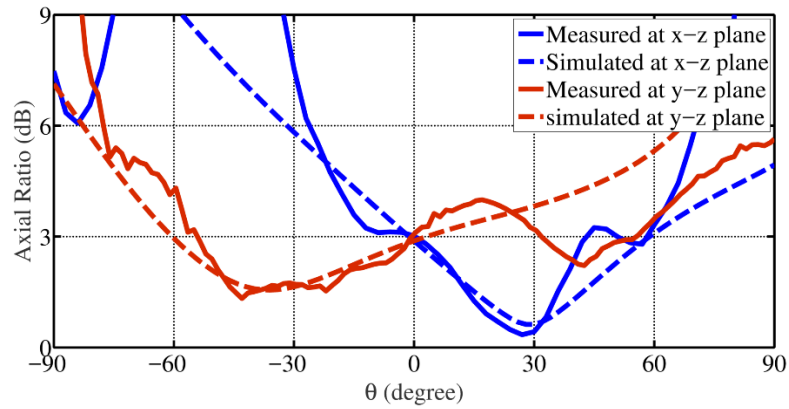


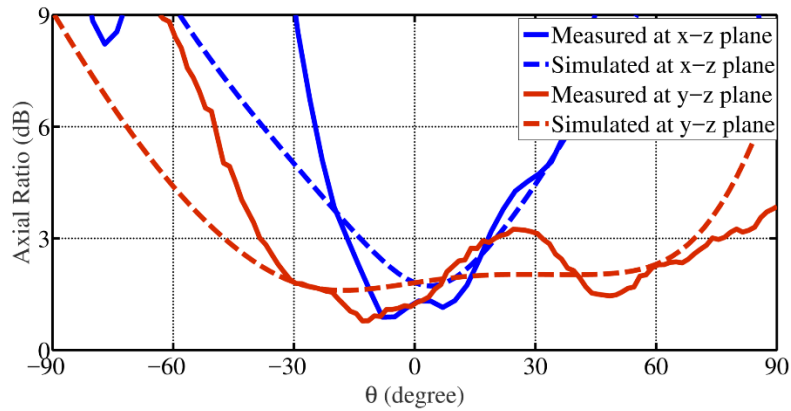
Figure 2-22. Simulated and measured radiation patterns on the (a) xoz -plane and (b) yoz -plane (dashed line: simulated; solid line: measured).

The angular AR performance is also investigated and the corresponding simulated results are plotted in Figure 2-23 as dashed lines. Specifically, the angular AR is simulated on the xoz -plane and yoz -plane at 3.9, 4.0, and 4.1 GHz. Based on the results, at 3.9 GHz, the AR beamwidths

(ARBWs) within which $AR < 3$ dB are 60.0° (from -1.2° to 58.8°) and 63.5° (from -60.4° to 3.1°) on the xoz -plane and $yo z$ -plane, respectively. The ARBW's are 33.5° (from -13.4° to 20.1°) and 116.8° (from -47.3° to 69.5°) on the xoz -plane and $yo z$ -plane, respectively, at 4.0 GHz. At 4.1 GHz, the ARBW's are 19.2° (from -18.9° to 0.3°) and 87.2° (from -1.6° to 85.6°) on the xoz -plane and $yo z$ -plane, respectively.



(a)



(b)

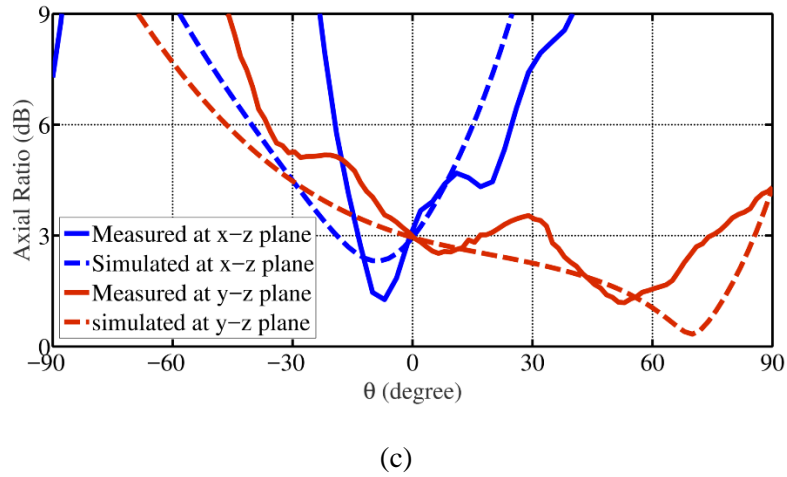


Figure 2-23. Simulated and measured angular AR at (a) 3.9, (b) 4.0, and (c) 4.1 GHz.

2.4.3 Experimental Results

To experimentally verify the proposed ICMS enabled integrated CP antenna design, an antenna prototype is fabricated, assembled, and measured. The antenna prototype is shown in Figure 2-24. It should be noted that a 1.5 mm-thick foam is inserted between the monopole antenna and the ICMS to fix the distance between them.



Figure 2-24. Antenna prototype of the ICMS enabled integrated CP antenna design.

Figure 2-21(a) shows the measured impedance matching performance of the proposed CP antenna as a solid S_{11} curve. A good agreement between the simulated and measured results is observed. Specifically, the measured $S_{11} < -10$ dB bandwidth is 620 MHz ranging from 3.67 GHz to 4.29 GHz, which is equivalent to a fractional bandwidth of 15.6%.

Figure 2-21(b) shows the measured AR of the proposed antenna as solid dots. As can be seen, the measured AR < 3 dB frequency band spans from 3.90 to 4.27 GHz resulting in a 370 MHz frequency band, which is equivalent to a fractional bandwidth of 9.1%. Since the measured AR < 3 dB frequency band is fully covered by the $S_{11} < -10$ dB band, the measured operational band of the antenna prototype is the same as the measured AR < 3 dB frequency band.

Figure 2-21(c) shows the measured gain profile of the antenna prototype. Within the operational band, the antenna gain varies from 5.5 dBi to 7.3 dBi, with the peak gain at 3.95 GHz.

Figure 2-22 presents the measured radiation patterns at 3.8, 4.0, and 4.2 GHz on both the xoz -plane and $yoze$ -plane as solid red curves. The measured HPBW's at 3.8 GHz are 81° and 72° on the xoz -plane and $yoze$ -plane, respectively. The measured HPBW's at 4.0 GHz are 73° and 79° on the xoz -plane and $yoze$ -plane, respectively. The measured HPBW's at 4.2 GHz are 64° and 65° on the xoz -plane and $yoze$ -plane, respectively.

The measured angular AR performances at 3.9 GHz, 4.0 GHz, and 4.1 GHz are displayed in Figure 2-23(a) to Figure 2-23(c) as solid curves. A reasonable agreement is achieved between the measured and simulated results. Specifically, the measured ARBW's at 3.9 GHz are 57.9° and 54.7° on the xoz -plane and $yoze$ -plane, respectively. The measured ARBW's at 4.0 GHz are 35.0° and 114.7° on the xoz -plane and $yoze$ -plane, respectively. The measured ARBW's at 4.1 GHz are 14.0° and 75.0° on the xoz -plane and $yoze$ -plane, respectively.

2.5 Conclusion

In this chapter, the design methodology of three compact antennas enabled by ICMS artificial ground planes were discussed. Two ICMS artificial ground planes with 1D and 2D IC loadings were proposed for LP antenna designs. Another ICMS artificial ground plane with modified IC loadings and additional slot loadings was proposed to realize an integrated antenna with CP radiation. Unit cell analyses were carried out to illustrate the operating principles of these antennas. Specifically, dispersion analysis of unit cells was done to realize the theory of bandwidth enhancement for the LP antennas. In addition, reflection analysis of unit cells was carried out to explain the CP radiation provided by the third antenna. All three proposed antennas realize performance enhancements in numerous aspects including operational bandwidth, gain, and FB ratio. To experimentally demonstrate the designs, three antenna prototypes were fabricated. Reasonable agreements between measured and simulated results were observed for the three proposed antenna designs. It is worth mentioning that due to the fabrication imperfections as well as the unwanted scatterings and power losses from the connecting cables used during measurements, small differences between the measured and the simulated results were observed.

Table 2-5. Comparison of Artificial Ground Plane Enabled Antenna Designs.

	Freq. (GHz)	S_{11} BW (%)	AR BW (%)	Gain (dBi/dBic)	FBTR (dB)	Footprint (λ_0^2)
[24]	2.45	5.5	-	6.2	23	0.15
[26]	2.45/5.8	4/12	-	6.4/7.6	> 10	0.96
[44]	2.45	18	-	5	8	0.29
[46]	1.92	6.7	-	4.5	5.6	0.09
[47]	3	8.18	3.3	5.1	-	0.19
	2.86/3.1	1.75/2.57	1.05/1.61	4.15/4.77	-	0.18

[48]	6.4	54.6	25.2	6.5	-	0.62
[49]	2.3	11.4	14.9	5.7	-	0.59
[50]	5.0	16	-	6.2	-	0.97
[51]	5.6	50	-	10	> 10	2.85
[52]	5.5	25	-	10.8	-	1.21
[53]	3.7	24	5.6	-	-	2.85
LP1	4	15.3	-	7.5	> 10	0.37
LP2	4	10.5	-	6.2	> 10	0.23
CP	4	15.6	9.1	7.3	> 15	0.32

Table 2-5 presents a comparison of the proposed antennas in this chapter and other MS artificial ground plane enabled antenna designs reported in the literature. It can be seen that the footprints of the proposed antennas in this chapter are smaller than most of their counterparts in the literature. Only the antenna designs reported in [24], [46], and [47] have smaller footprints. Even with their miniaturized form factors, the proposed antennas maintain wide operational bands as well as moderate gain performances. In summary, the proposed antennas in this chapter are promising candidates to be integrated in modern compact communication systems with wideband requirements.

Chapter 3

Miniaturized Dual-band Antenna Enabled by an Artificial Ground Plane Loaded with Complementary Split Ring Resonators

3.1 Introduction

The miniaturization of modern communication systems demands antennas with more than one operational band. Compared to antennas with a single operational band, dual-band and multi-band antennas can offer significant size reduction by accommodating multiple communication channels within a single antenna aperture. In Chapter 2, MSs were adopted as artificial ground planes to realize compact wideband antenna designs. In this chapter, the design of a dual-band compact antenna with a CSRR-loaded MS as the antenna's artificial ground plane is introduced.

There have been many MS-based dual-band or multi-band planar antenna designs with various functionalities reported in the literature [23, 26, 47, 54-57]. MSs are implemented in dual-band or multi-band antenna designs in three primary ways.

The first way is to make an MS a part of the main radiator. For instance, an MS formed as a 2×2 array of modified mushroom unit cells was proposed in [54]. The MS was then incorporated into a patch antenna to realize a dual-band antenna operating at 2.4 and 3.5 GHz. By virtue of the MS, the antenna was able to realize not only size reduction but also gain enhancement. Another antenna design was reported in [23]. In this design, a conventional patch radiator was loaded with an MS that was a 5×5 periodic array of shielded mushroom unit cells. Because of the MS loading, the antenna simultaneously achieved multiple operational bands and two different operating modes. A dual-band antenna with a small frequency ratio enabled by an MS that serves as the main radiator was reported in [55]. The MS was a 2D composite right/left-handed (CRLH) transmission line

realized by CSRRs and gap loadings. Another dual-band linearly-polarized (LP) antenna with a distinct sense of polarizations at two operational bands was proposed in [58]. The authors implemented an MS that was a 2×2 periodic array of modified mushroom unit cells as part of the feeding component. This type of MS-enabled antenna design has also been applied to wearable communication systems. For example, in [40], by loading a conventional patch antenna with an MS that was a 2×1 array of modified mushroom unit cells, a wearable antenna operating at WLAN bands with a small form factor and high isolation from the human body loading was realized. In [57], a dual-band dual-mode antenna with an MS consisting of a 2×2 array of modified mushroom unit cells incorporated into a conventional patch antenna realized omnidirectional and unidirectional radiation patterns at two operational bands.

The second way is placing MSs below conventional patch antennas. Unlike using an MS directly as an antenna ground plane, patch antennas and MSs in this class share the same ground plane. One example is the antenna design reported in [47]. The reported antenna was a dual-band CP antenna operating at 2.9 and 3.1 GHz. This functionality was accomplished by inserting an MS with the reactive impedance characteristic beneath a slotted patch antenna. The MS was an 8×8 unit cell array, and each unit cell consisted of a square patch printed on a grounded dielectric slab. Similar square-patch type unit cells were also used in [56] and [58], where dual-band antennas based on a 5×5 array of such unit cells were utilized to achieve dual-band functionality.

The last category of MS-enabled dual-band or multi-band antenna designs employs MSs as artificial ground planes. A planar monopole antenna is always included, serving as the feeding component, and the MS is the main radiator. A dual-band wearable antenna (2.45/5 GHz) was proposed in [26]. The MS was a 3×3 periodic array of unit cells fabricated based on clothing fabrics. Each unit cell consisted of two concentric conducting square-shaped rings printed on a grounded fabric layer. A monopole that was also fabricated by using the fabric materials was placed above the MS as the feeding component. The proposed antenna not only possessed miniaturized

antenna volume, but also achieved multiple antenna performance enhancements such as an improved broadside gain and FB ratio, which are desirable features for wearable applications. In summary, researchers and engineers have discovered that the MS artificial ground plane enabled antenna exhibits numerous advantages, including high gain [42, 50, 51, 44, 26, 24, 59], wide operational bandwidth [60, 46, 59, 48, 43, 49], a small form factor [60, 44, 46, 24, 59, 53], and a high FB ratio [42, 46, 44, 24, 59, 61].

In this chapter, a novel low-profile and compact MS artificial ground plane enabled dual-band LP antenna is presented. The MS is loaded with CSRRs together with capacitive gaps. The CSRR loadings are proven to realize the dual-band operational bands and antenna volume miniaturization simultaneously. The proposed antenna works at 1.9 and 2.5 GHz with an overall electrical footprint $0.062 \lambda_0^2$, where λ_0 is the wavelength at 1.9 GHz in free space. Moreover, the two operational bands can be independently tuned by adjusting the corresponding design parameters. Unidirectional radiation along the broadside is observed at both bands. The detailed antenna design is presented in Section 3.2. In Section 3.3, the independent band-tuning techniques are discussed. A comparison between the proposed antenna and U-slot patch antennas is made in Section 3.4. The simulated antenna performances and experimental results of measuring an antenna prototype are shown in Section 3.5. This chapter is concluded in Section 3.6.

3.2 Antenna Design

The configuration of the proposed MS artificial ground plane enabled integrated antenna is shown in Figure 3-1(a). The integrated antenna consists of an MS artificial ground plane as well as a printed planar monopole antenna. The monopole antenna consists of a circular patch connected to a SubMiniature version A (SMA) connector (not shown) by a 50Ω microstrip line with stepped sections, which are adopted here to offer additional design flexibility for tuning a better impedance

matching. In addition to the stepped sections, tuning the radius of the circular metallic patch helps to obtain the optimal impedance matching of the integrated antenna. As the monopole antenna only serves as the feeding component to reactively couple power from the source to the MS artificial ground plane, its shape is not a critical factor and thus not limited to be circular. This is confirmed by additional simulations that reveal that the replacement of the circular patch with a rectangular one has only a minor effect on the overall antenna performances. Both the monopole antenna and MS artificial ground plane are printed on Rogers RO3003 laminates with a dielectric constant $\epsilon_r = 3$ and a dielectric loss tangent $\tan\delta = 0.001$. The thickness of the monopole layer is 1.52 mm and that of the MS artificial ground plane layer is 5.6 mm. The MS artificial ground plane is actually an array formed by 4×1 unit cells. Figure 3-2 illustrates the configuration of a single unit cell. Basically, two layers are involved: a rectangular gapped metallic patch printed on a dielectric substrate and a rectangular CSRR printed on another grounded dielectric substrate. The thickness of the first and the second layers is 1.04 and 4.56 mm, respectively. As the MS artificial ground plane is highly truncated and only contains four unit cells, a highly miniaturized antenna footprint of $24 \times 64 \text{ mm}^2$ is accomplished. This is equivalent to $0.062\lambda_0^2$, where λ_0 is the free space wavelength at 1.9 GHz.

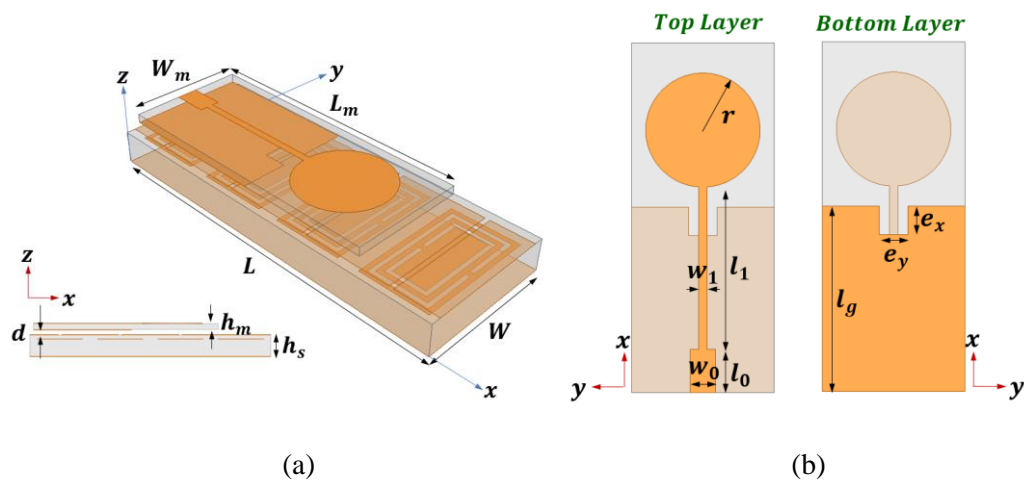


Figure 3-1. Configurations of (a) the dual-band MS artificial ground plane enabled integrated antenna and (b) the printed planar monopole feeding antenna.

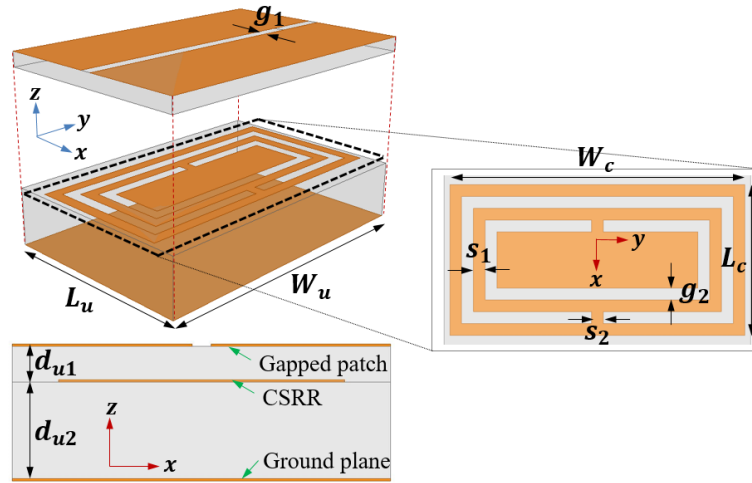


Figure 3-2. Exploded and stacked view of a CSRR loaded double-layered unit cell.

3.2.1 Unit Cell Synthesis and Analysis

The characterization of a single MS artificial ground plane unit cell is carried out by numerical simulation using HFSS [30]. The simulation model and the corresponding simulated and calculated dispersive properties of the unit cell are shown in Figure 3-3(a). The unit cell simulation is based on the simulation methods in [52, 60]. Basically, port 1 and 2 are assigned to the two faces of the dielectric substrate perpendicular to the x -axis (refer to Figure 3-2 for the corresponding coordinate system). An air box (not shown) is also built up to enclose the whole unit cell model to model an infinite free-space environment. The simulated dispersive curve (solid blue) of wave propagating along the x -axis within the MS unit cell is presented in Figure 3-3(a). The dispersive behavior of light propagating in air (dashed grey) is also shown for reference. It is observed that the simulated dispersive curve splits at 2.37 GHz to form two frequency bands due to the resonating characteristic of the CSRR structure. In other words, the unit cell has a self-resonance occurring at 2.37 GHz mainly due to the resonating characteristic of the embedded CSRR structure. As is

explained in detail in the following sections, it is the two frequency bands that enable the dual-band functionality of the proposed integrated antenna.

While the aforementioned unit cell simulation is based on the “Driven Model” solver in HFSS, another unit cell simulation is carried out based on the “Eigenmode” solver in HFSS. The simulation setup and corresponding results are not shown here. It is found that the two simulations reasonably verify each other. The two TM modes (with an in-phase E -field aligned along the z -axis) obtained from the “Eigenmode” simulation have exactly the same dispersive behaviors as the two bands of the simulated dispersion curve in Figure 3-3(a).

In addition to full-wave simulations, the dispersive property of a single MS unit cell is analytically calculated based on the developed equivalent circuit shown in Figure 3-3(b). In the circuit model, C_{se} indicates the serial capacitance provided by the patch gap on the top surface of the unit cell. C_f represents the capacitive coupling between the gapped patch and the embedded CSRR structure. C_{CSRR} and L_{CSRR} are used to characterize the capacitance and inductance of the CSRR resonator. C_{sh} models the capacitive coupling between the CSRR and the unit cell ground. The gapped patch is considered to be formed by two equal-length microstrip transmission lines. Based on the dielectric constant, the thickness of the unit cell substrate, and the width of the gapped patch, the characteristic impedance of the equivalent microstrip transmission lines is 59Ω . Then, C_{CSRR} and L_{CSRR} are calculated based on the equations in [62]. It should be mentioned that the equations are modified in this particular case because the CSRR in our proposed design is rectangular instead of circular as in [62]. Then, curve fitting is carried out by tuning the lumped element values. The finalized lumped element values are listed in the caption of Figure 3-3. As can be seen from Figure 3-3(b), the calculated dispersive curve represented as a red dashed line is almost the same as the simulated dispersive curve, validating the proposed equivalent circuit model.

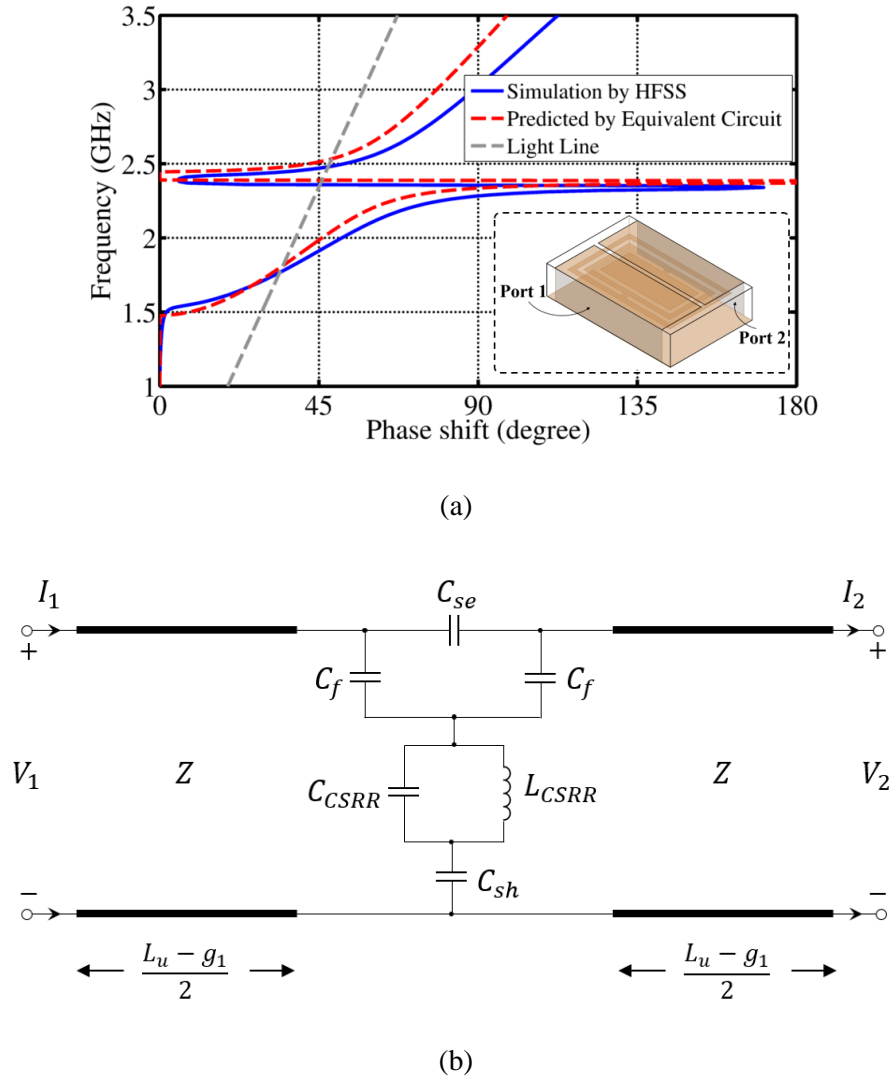


Figure 3-3. (a) Simulated and calculated dispersion properties and (b) the equivalent circuit of a single MS unit cell. The finalized circuit parameters are $C_{se} = 1$ pF, $C_f = 5$ pF, $C_{sh} = 0.3$ pF, $C_{CSRR} = 0.48$ pF, and $L_{CSRR} = 5.7$ nH.

3.2.2 Simulated Antenna Performances

Once the unit cell synthesis is completed, the MS artificial ground plane is constructed as a 4×1 periodic unit cell array. Then, the proposed dual-band antenna is integrated by placing a printed planar monopole antenna 1.5 mm above the MS artificial ground plane. It should be noted that during the antenna prototyping, a 1.5 mm-thick foam is inserted between the monopole antenna

and the MS artificial ground plane. Since the dielectric constant of the foam is almost the same as that of the air, the gap between the monopole antenna and the MS artificial ground plane is modeled as an air layer. It should be mentioned that the gap size is tuned to be 1.5 mm in order to obtain the optimal impedance matching for the integrated antenna. The detailed dimensions associated with Figure 3-1 and Figure 3-2 are shown in Table 3-1.

Table 3-1. Detailed Dimensions of the Proposed Dual-Band Antenna (all in mm).

L	W	L_m	W_m	d	h_m	h_s	r	w_0	w_1	l_0	l_1	l_g
64	24	49	20	1.5	1.5	5.6	8	3.6	1.2	6	22.8	26
e_x	e_y	L_u	W_u	L_C	W_C	s_1	s_2	g_1	g_2	d_{u1}	d_{u2}	
4	4	16	20.8	12.1	20	0.8	0.8	0.8	0.8	1.04	4.56	

The simulated impedance matching performance of the proposed antenna is presented in Figure 3-4. As can be clearly seen, two resonances are observed at 2.02 and 2.51 GHz, respectively, giving rise to two $S_{11} < -10$ dB frequency bands. The simulated bandwidth of the first frequency band is equal to 50 MHz ranging from 1.99 to 2.04 GHz. This is equivalent to a fractional bandwidth of 2.5%. The second $S_{11} < -10$ dB impedance matching band is 50 MHz ranging from 2.49 to 2.54 GHz, which is equivalent to a fractional bandwidth of 2.0%.

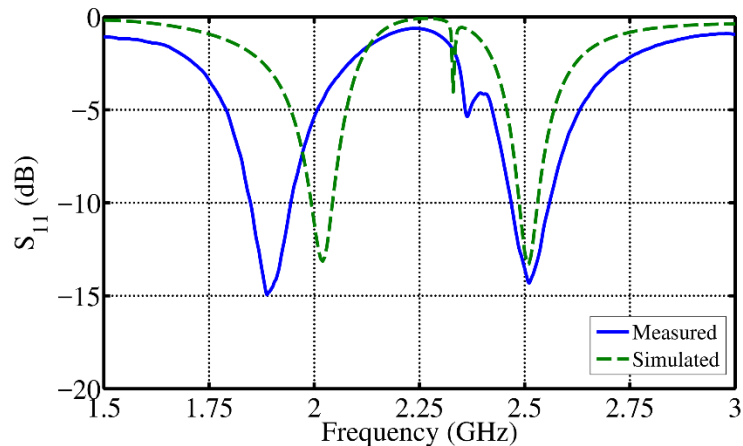
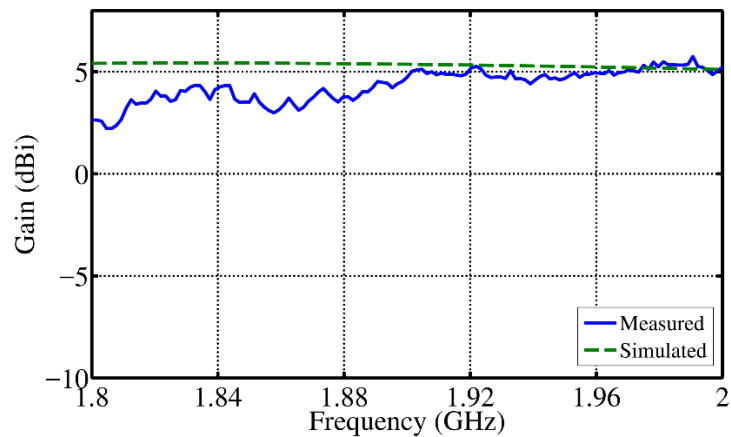
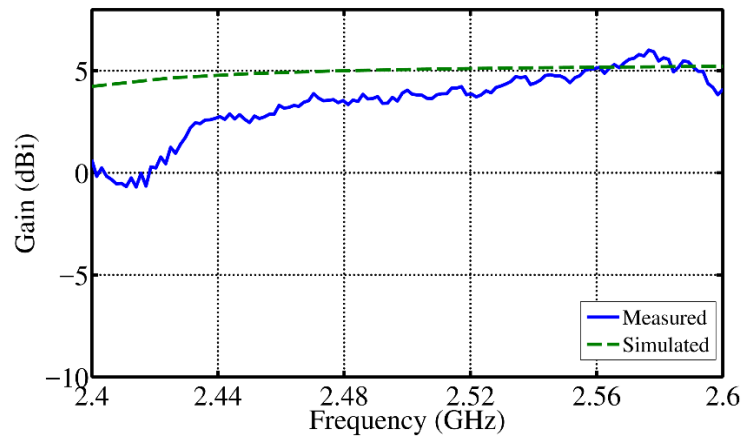


Figure 3-4. Simulated and measured impedance matching performances of the proposed dual-band LP antenna enabled by an MS artificial ground plane.

The simulated broadside gain performances for the two operational bands are plotted in Figure 3-5(a) and Figure 3-5(b), respectively. Specifically, within the first and second simulated $S_{11} < -10$ dB band, the antenna gains along the broadside are above 5 dBi.



(a)

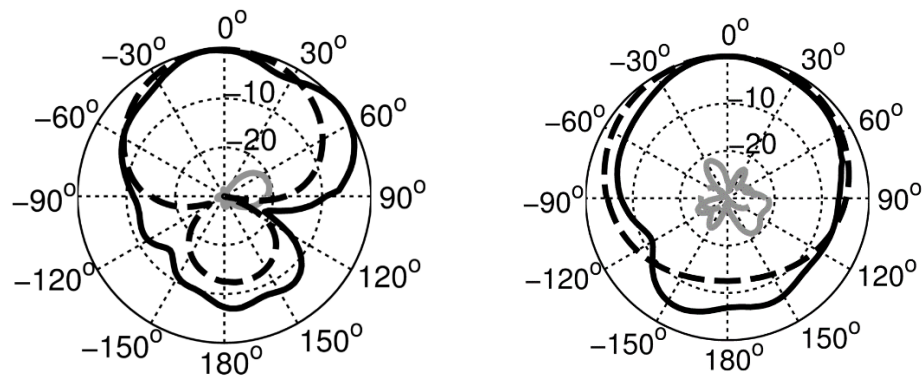


(b)

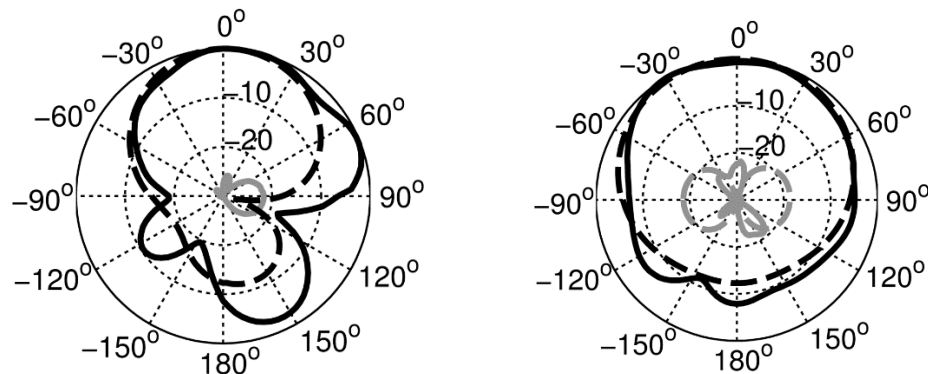
Figure 3-5. Simulated and measured broadside gains of the (a) first and (b) second frequency band.

The simulated normalized radiation patterns of the integrated antenna on both the E -plane and H -plane at 2.0 and 2.5 GHz are plotted in Figure 3-6(a) and Figure 3-6(b), respectively. At 2.0

GHz, the simulated HPBWs are 82° and 142° on the E -plane and H -plane, respectively. At 2.5 GHz, the simulated HPBWs are 76° and 128° on the E -plane and H -plane, respectively. It can be clearly seen that the HPBWs on the H -plane are larger than those on the E -plane. This is because the proposed integrated antenna has a much smaller size on the H -plane. In addition, the FB ratios of the simulated radiation patterns are all maintained above 10 dB, indicating that the back lobes are well suppressed.



(a)



(b)

Figure 3-6. Simulated and measured normalized radiation patterns on the E -plane and H -plane at (a) 2.0 and (b) 2.5 GHz (dashed lines: simulated; solid lines: measured; black lines: co-polarization; grey lines: cross-polarization).

3.2.3 Antenna Working Principles

The integrated antenna can be regarded as formed by two parts, *i.e.* the feeding and radiating parts. The feeding part is the planar monopole antenna and the radiating part is the MS artificial ground plane. The power is transferred from the planar monopole antenna to the MS artificial ground plane through capacitive coupling. As is later shown, the MS artificial ground plane operates like a conventional rectangular patch antenna working in the TM_{10} mode at both bands. For purpose of differentiation, the resonant mode of the MS artificial ground plane is denoted as the MS- TM_{10} mode. For the MS- TM_{10} mode to be excited the following equation must be satisfied:

$$N_x \beta_x p_x = m\pi, (m = 0, \pm 1, \pm 2, \dots) \quad (3-1)$$

where N_x is the number of unit cells along the x -axis. In the proposed MS artificial ground plane, $N_x = 4$. The parameter β_x indicates the propagation constant of the standing wave within the MS artificial ground plane along the x -axis, and p_x is the length of one unit cell along the x -direction. The product of β_x and p_x is the phase shift along the x -axis of a single unit cell corresponding to the horizontal axis of Figure 3-3(a). The parameter m on the right-hand side of Eq. (2-1) indicates the order of the MS artificial ground plane resonant modes. Here, as is explained later, only the fundamental mode with $m = +1$ is of interest and

$$\beta_x p_x = \frac{\pi}{4} \quad (3-2)$$

According to Figure 3-3(a), the corresponding resonant frequency can be predicted as the value of the vertical coordinate of the point on the dispersive curve with the phase shift along the x -axis to $\frac{\pi}{4}$. Based on Figure 3-3(a), the predicted resonant frequencies are 1.9 and 2.5 GHz. Comparing the predicted frequencies with those simulated and shown in Figure 3-4, it can be seen that the resonant frequencies of the integrated antenna can be predicted with high accuracy through the dispersive behavior of a single unit cell. The reason why only the fundamental modes are considered is

explained as follows. The zeroth order mode with $m = 0$ is known to have an omnidirectional radiation pattern and cannot be excited through our capacitive coupling feeding method. Within the first band shown in Figure 3-3(a), higher-order modes with $m \geq 2$ are featured with high quality-factor and resonant frequencies very close to the self-resonance of the unit cell. These multiple resonances are merged to form a single spurious resonance with the narrow band of the integrated antenna (see Figure 3-4) at around 2.3 GHz. On the other hand, within the second band shown in Figure 3-3(a), the higher-order modes give undesirable radiation patterns and a large electrical antenna size. For example, as shown in Figure 3-7, when $m = +2$, this second order resonance occurs at 3.15 GHz and a conical radiation pattern instead of a unidirectional broadside pattern is achieved. In addition, higher-order modes are inherently narrow-band, making them of little interest. It should also be noted that because there are no left-handed modes supported in our proposed MS, m can only be a positive integer in Eq. (3-1).

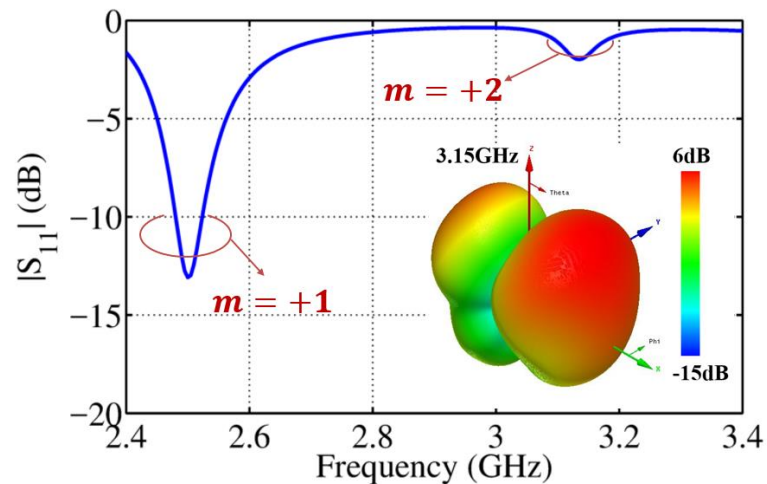


Figure 3-7. Illustration of the second order within the second band.

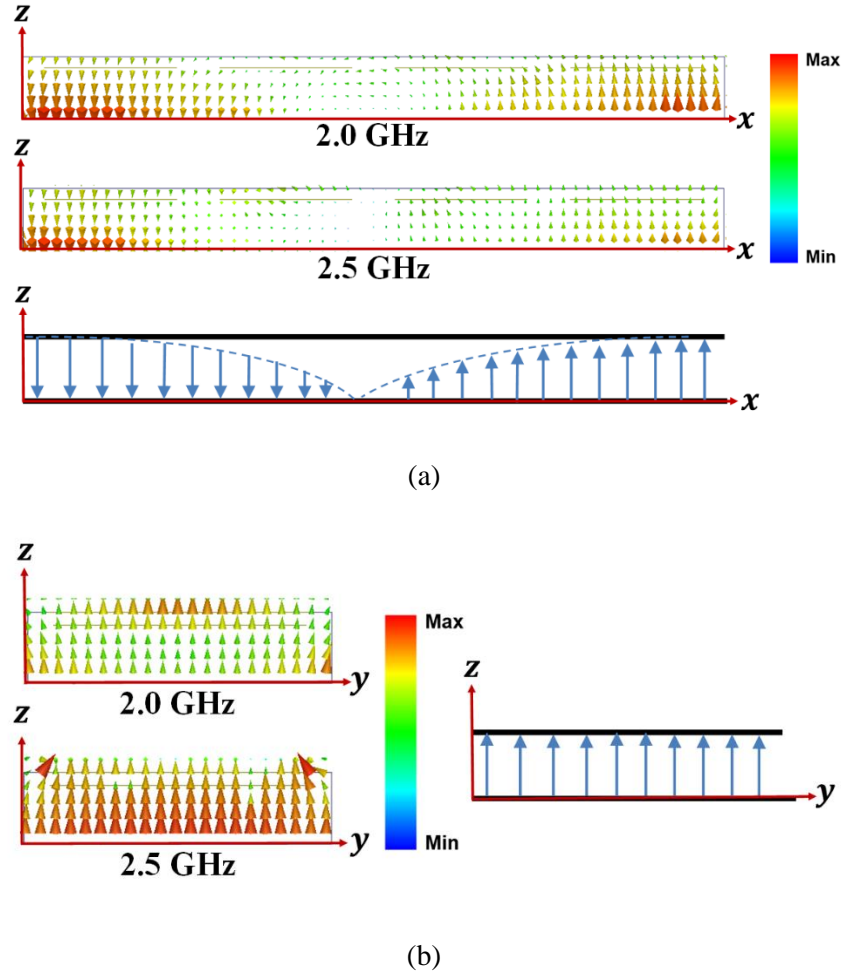
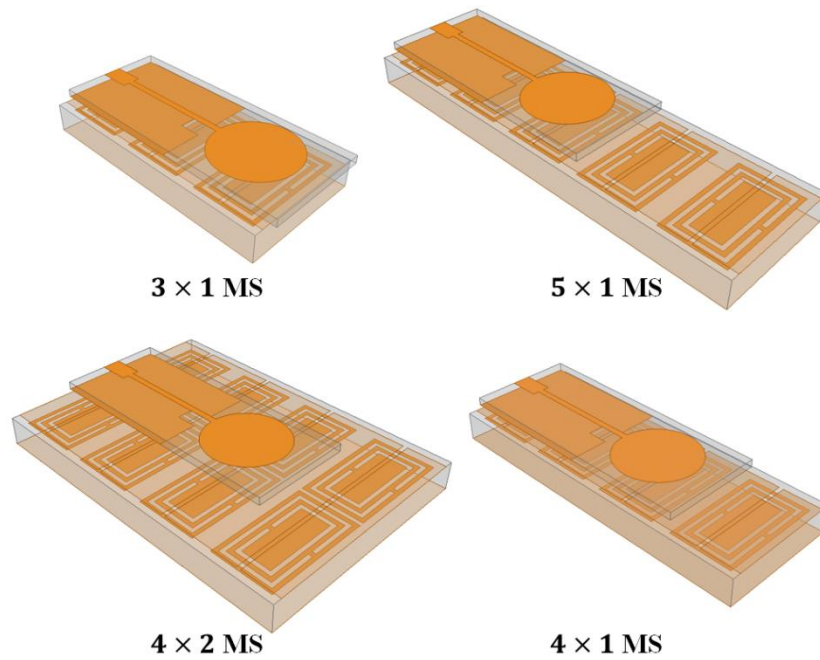


Figure 3-8. Simulated and sketched E -field distributions at 2.0 and 2.5 GHz on (a) $y = 0$ and (b) $x = 64$ mm planes.

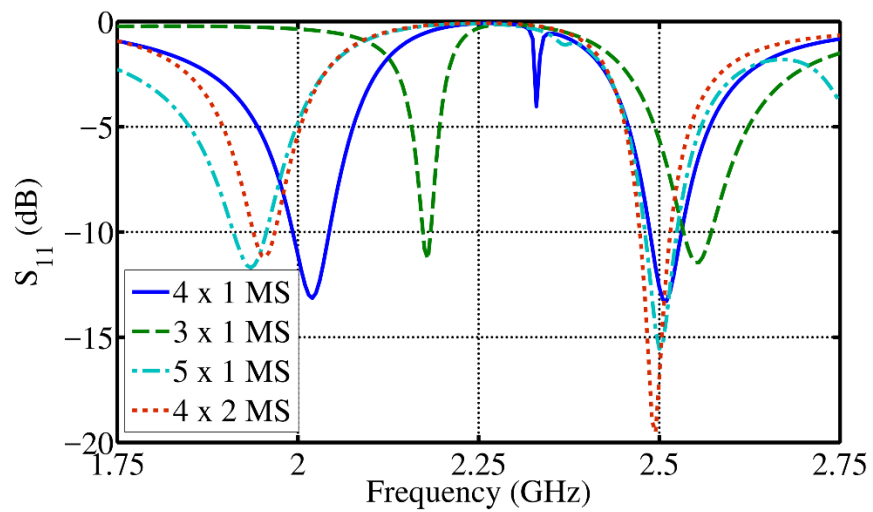
In order to compare the MS- TM_{10} mode of the MS artificial ground plane with the TM_{10} mode of a conventional rectangular patch antenna, the simulated E -field distributions of the proposed MS artificial ground plane and the sketched E -field distributions of a rectangular patch antenna operating in TM_{10} are plotted in Figure 3-8. The simulated E -field distributions are plotted on the $y = 0$ and $x = 64$ mm planes (see Figure 3-1 for the coordinate system) at both 2.0 and 2.5 GHz. Similarities are observed between the simulated and sketched E -field distributions, verifying that the MS- TM_{10} mode of the MS artificial ground plane at both 2.0 and 2.5 GHz is equivalent to

the TM_{10} mode of a rectangular patch antenna. Thus, broadside unidirectional radiation patterns are expected for the MS artificial ground plane at the 2.0 and 2.5 GHz bands.

To further demonstrate the validity of Eq. (3-1) and (3-2) and the radiation mechanisms, integrated antennas with different MS artificial ground plane configurations are simulated and compared. Figure 3-9(a) shows the integrated antennas under investigation. It should be noted that the integrated antenna enabled by the 4×1 MS artificial ground plane discussed in previous sections is also included. In addition, three MS artificial ground planes formed as 3×1 , 5×1 , and 4×2 periodic unit cell arrays are shown. All the MS artificial ground planes are fed by the same printed planar monopole antenna. The simulated S_{11} performances are summarized in Figure 3-9(b). The simulated resonant frequencies of these integrated antennas and those analytically calculated based on Eq. (3-1) and (3-2) are compared and tabulated in Table 3-2. Specifically, the resonant frequencies of the 4×1 and 4×2 MS artificial ground plane based integrated antennas should be the same, according to Eq. (3-1) and (3-2). This is indeed the case, as shown in Table 3-2. The predicted resonant frequencies for the integrated antennas with 3×1 and 5×1 MS artificial ground planes are 2.14/2.62 GHz and 1.79/2.50 GHz, respectively. These analytically predicted frequencies correspond well with those obtained through full-wave simulations, which are 2.18/2.55 GHz for the 3×1 MS artificial ground plane based antenna and 1.94/2.50 GHz for the 5×1 MS artificial ground plane based antenna. In conclusion, the validity of Eq. (3-1) and (3-2) is demonstrated. In addition, the radiation patterns of these integrated antennas are examined (not shown here). As expected, they all possess unidirectional radiation patterns along the broadside at both operational bands. It should be mentioned that a larger MS artificial ground plane leads to a higher antenna gain and FB ratio.



(a)



(b)

Figure 3-9. (a) Configurations and (b) simulated S_{11} performances of integrated antennas with different MS artificial ground planes.

Table 3-2. Analytically Predicted and Numerically Simulated Resonant Frequencies of Different Dual-band MS Artificial Ground Plane Enabled Antennas.

Number of Unit Cells	Predicted Frequencies (GHz)	Simulated Frequencies (GHz)
4×1	1.92/2.53	2.02/2.51
3×1	2.14/2.62	2.18/2.55
4×2	1.92/2.53	1.95/2.49
5×1	1.79/2.50	1.94/2.50

3.3 Individual Band-tuning Technique

It is desirable for multi-band antennas to have adjustable frequency ratios and for their operational bands to be tuned independently. Based on the equivalent circuit mode depicted in Figure 3-3(b) as well as full-wave parametric studies on different design parameters, techniques for individually tuning the operational bands of the proposed dual-band MS artificial ground plane enabled integrated antenna are developed in the section. The design parameters included to realize the individual band tuning techniques are d_{u1} , d_{u2} , W_C , and L_C , which represent the thickness of the first and second MS artificial ground plane layers and length and the width of the embedded CSRR resonators, respectively.

The simulated S_{11} performances of the integrated antenna with varying d_{u1} are plotted in Figure 3-10. As can be seen, by increasing d_{u1} from 0.76 to 1.52 mm, the resonant frequency of the first band is shifted from 1.95 to 2.09 GHz while the resonant frequency of the second band is maintained at 2.50 GHz. Thus, the independent tuning of the first operational band can be easily achieved by adjusting d_{u1} , the thickness of the first layer of the MS artificial ground plane. This band tuning functionality can be explained by the equivalent circuit model shown in Figure 3-3(b).

Basically, adjusting the value of d_{u1} affects the capacitive coupling between the gapped patch and the CSRR structure. Consequently, the value of C_f in the equivalent circuit is tuned. Specifically, the value of C_f is decreased with the increased value of d_{u1} due to a weaker coupling. Simple calculation based on the circuit model shows that varying values of C_f lead to variation in the first band of the dispersion of a single unit cell but have a minor effect on the second band. In summary, the independent tuning of the first band is achieved by adjusting d_{u1} which can be explained by the equivalent circuit shown in Figure 3-3(a).

However, it is found that the second operational band cannot be tuned independently by only varying a single parameter. Thus, the feasibility of simultaneously changing two parameters to tune the second operational band is explored in the rest of this section. Intuitively, if there exists a design parameter that can be adjusted to tune the two operational bands at the same time, a proper tuning of this parameter together with d_{u1} may only vary the second operational band.

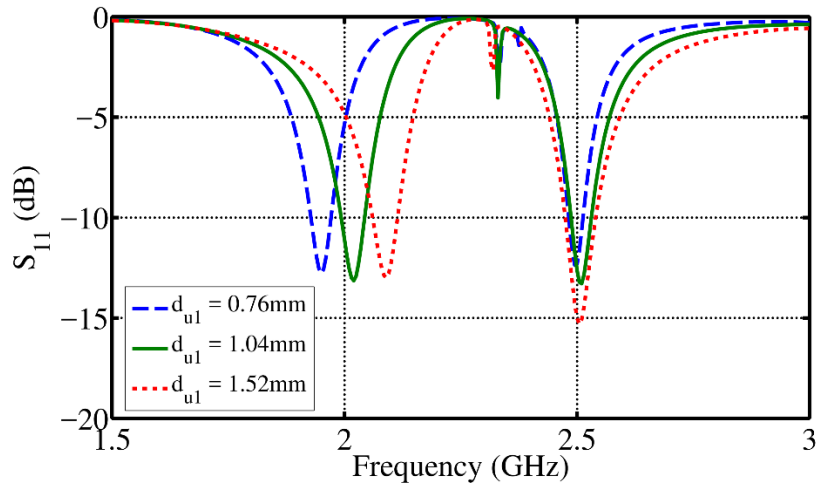
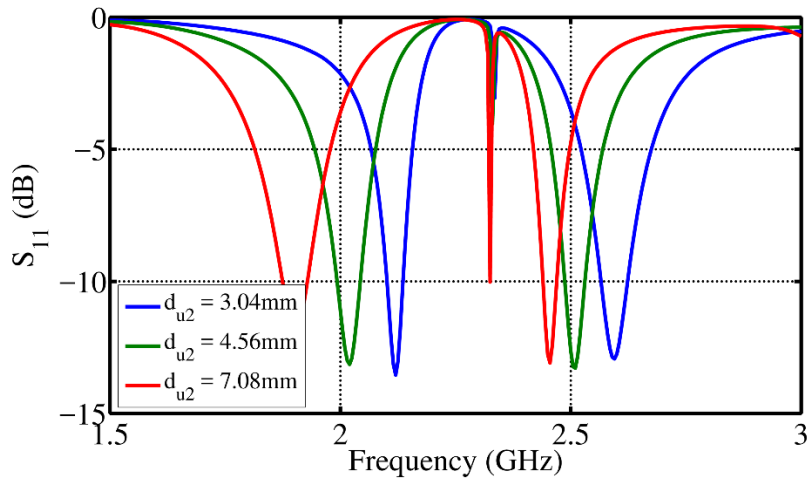


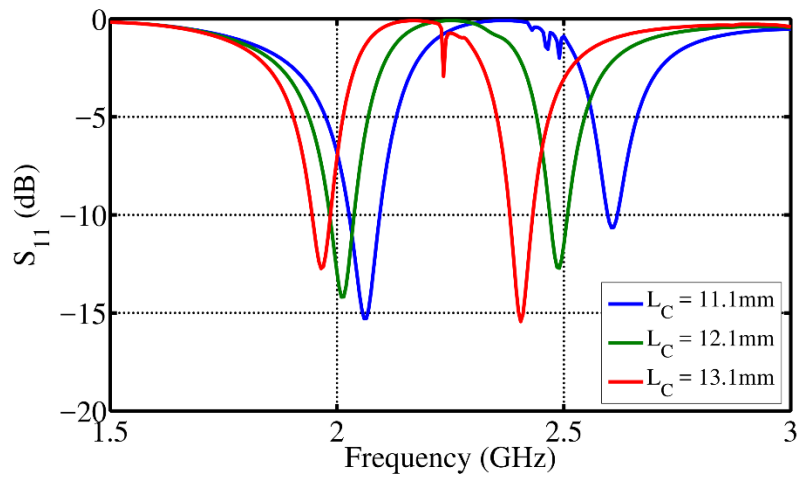
Figure 3-10. Independent tuning of the first operational band by adjusting d_{u1} .

The simulated S_{11} performances with varying d_{u2} , W_C , and L_C are plotted in Figure 3-11(a), Figure 3-11(b), and Figure 3-11(c), respectively. From these figures, it is concluded that the two operational bands can be tuned together towards either higher or lower frequency bands by

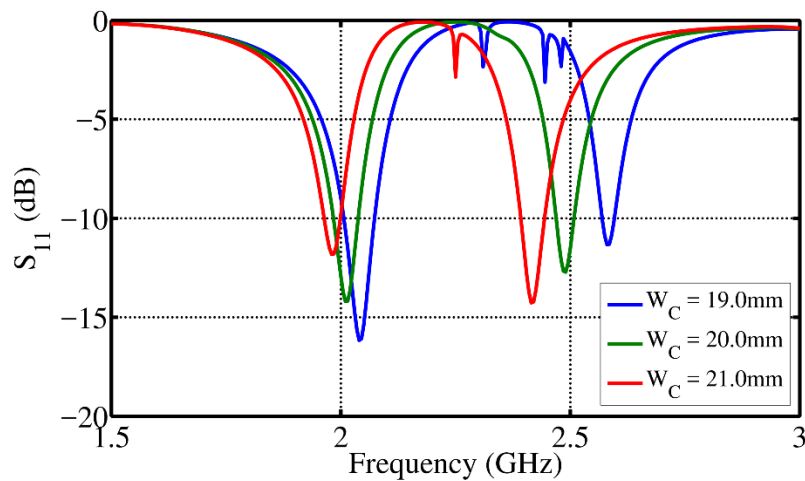
tuning one of the three parameters under investigation. This can also be explained by the equivalent circuit model shown in Figure 3-3(b). Firstly, if d_{u2} is decreased, the coupling between the embedded CSRRs and the ground plane becomes stronger. In other words, C_{sh} becomes larger. A simple calculation based on the equivalent circuit reveals that by increasing C_{sh} simultaneous blue shifts of both operational bands can be obtained, as shown in Figure 3-11(a). Secondly, changes in L_C and W_C mainly affect the resonant frequency of the CSRR resonator. Thus, in the equivalent circuit in Figure 3-3(b), the capacitance C_{CSRR} and the inductance L_{CSRR} are changed accordingly. Specifically, larger values of L_C and W_C result in larger C_{CSRR} and L_{CSRR} values, leading to a lower resonant frequency of CSRR. Through circuit calculation, we can see that this ultimately gives rise to the simultaneous band shifts of the two operational bands of the integrated antenna, as illustrated in Figure 3-11(c).



(a)



(b)

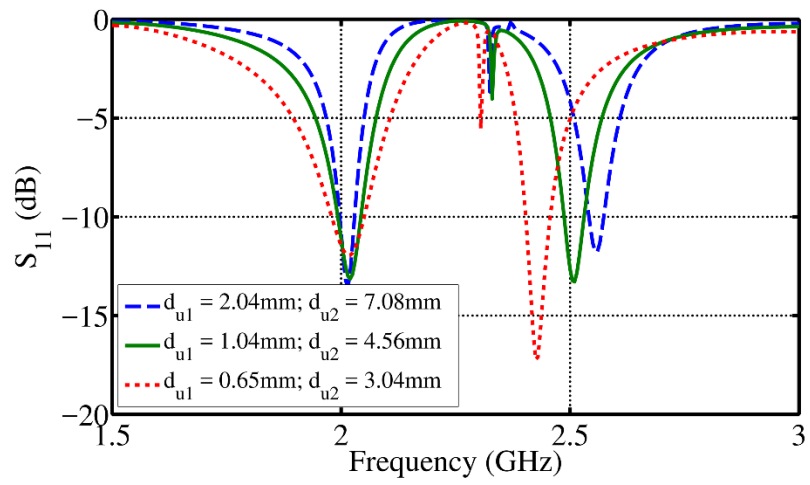


(c)

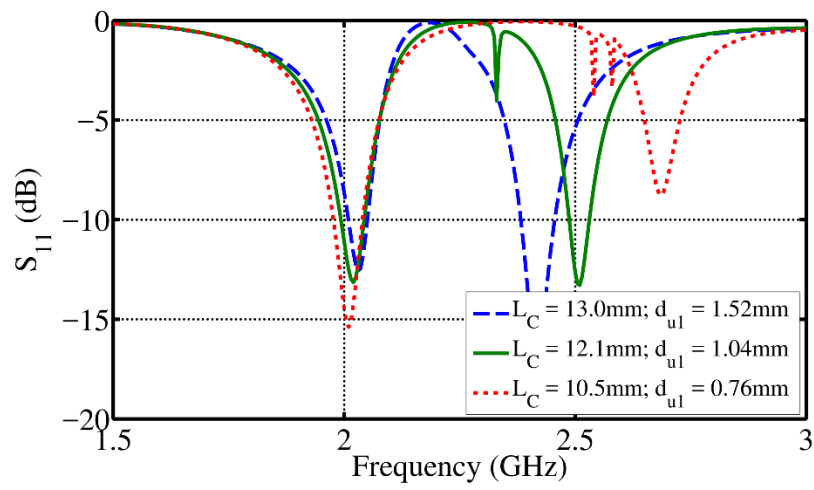
Figure 3-11. Parametric studies of (a) d_{u2} , (b) L_C , and (c) W_C .

Using the above parametric studies, the independent tuning of the second band is demonstrated in Figure 3-12. Basically, three tuning methods that include simultaneously adjusting the values of (d_{u1}, d_{u2}) , (d_{u1}, L_C) , and (d_{u1}, W_C) are introduced. These methods are shown in Figure 3-12(a), Figure 3-12(b), and Figure 3-12(c), respectively.

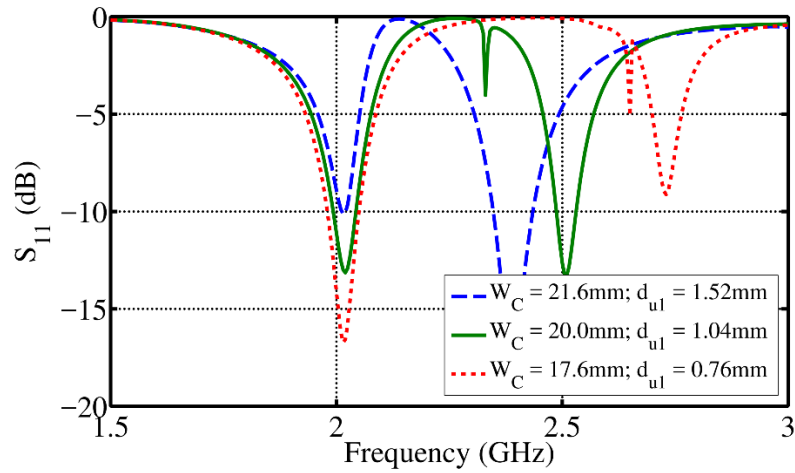
It is worth mentioning that further antenna miniaturization can also be obtained by the tuning technique discussed above.



(a)



(b)



(c)

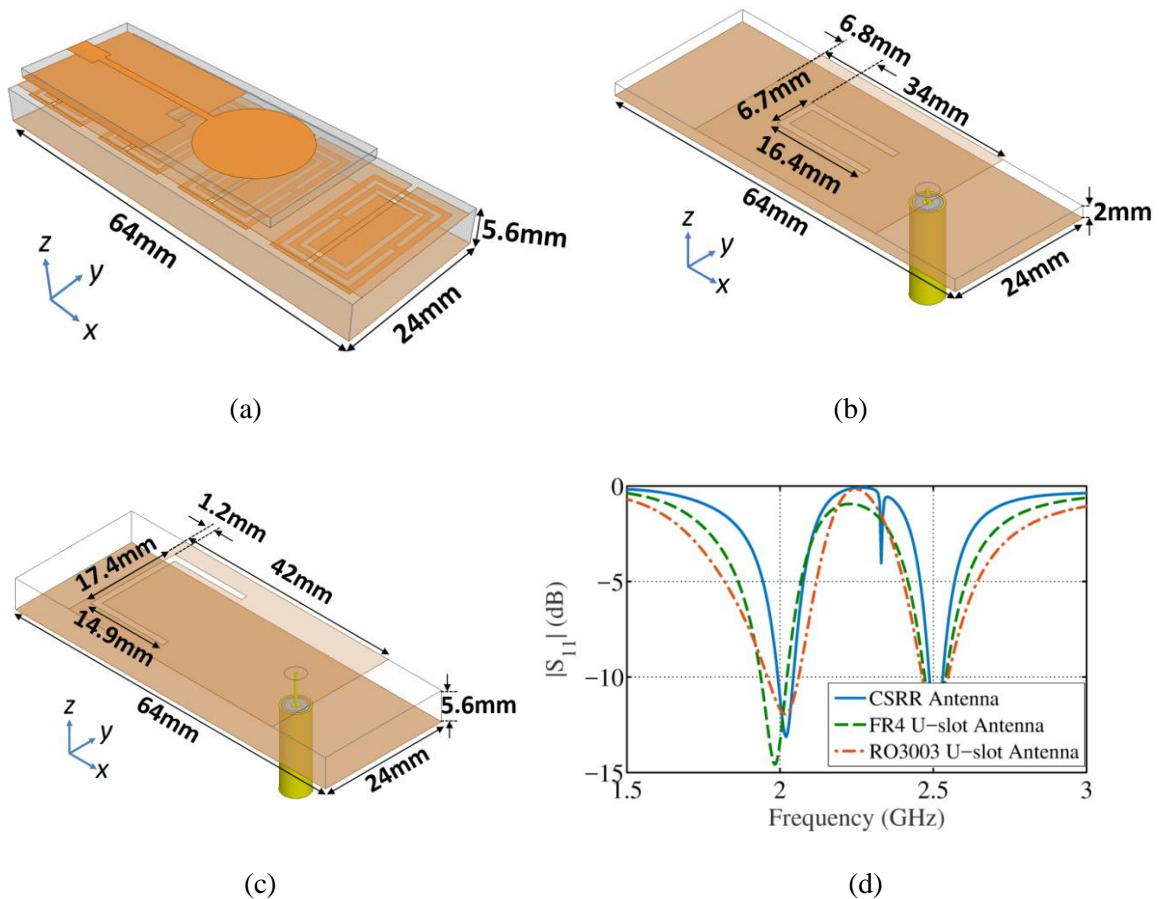
Figure 3-12. Individual band-tuning technique for the second operational band, which relies on simultaneously varying the parameters (a) d_{u1} and d_{u2} , (b) d_{u1} and L_C , and (c) d_{u1} and W_C .

3.4 Comparison with Conventional U-Slot Antenna

For a better illustration of the advantages of the proposed antenna over conventional patch antennas, a comparison among the proposed dual-band antenna, a conventional dual-band probe-fed U-slot patch antenna based on an FR4 substrate with a thickness of 2 mm, and a conventional dual-band probe-fed U-slot patch antenna based on an RO3003 substrate with a thickness of 5.6 mm (equal to that of the MS in our proposed antenna) is presented.

The configurations of the antennas are shown in Figure 3-13(a) to Figure 3-13(c). It should be noted that all three antennas have the same footprint, which is 64 mm \times 24 mm. For the two conventional patch antennas, the width of their radiating patches is kept the same and equal to 24 mm. However, the lengths of the patch antennas, the dimensions of the U-shaped slots, and the positions of their feeding probes are tuned so that impedance matchings are realized at 2.0 GHz as well as 2.5 GHz.

The simulated S_{11} results of the antennas are summarized in Figure 3-13(d). The simulated $S_{11} < -10$ dB bandwidths at the 2.0 GHz frequency band of the MS artificial ground plane based, the FR4-based, and the RO3003-based dual-band antennas are 50 MHz (2.5%), 86 MHz (4.3%), and 102 MHz (5.1%), respectively. The simulated $S_{11} < -10$ dB bandwidths at the 2.5 GHz frequency band of the MS artificial ground plane based, the FR4-based, and the RO3003-based dual-band antennas are 50 MHz (2.0%), 69 MHz (2.8%), and 84 MHz (3.4%), respectively. In Figure 3-13(e) and Figure 3-13(f), the gains of the MS artificial ground plane based, the FR4-based, and the RO3003-based dual-band antennas are plotted at 2.0 GHz and 2.5 GHz, respectively. It can be seen that at 2.0 GHz, the gains of the three antennas are 5.4 dBi, 2.0 dBi, and 4.1 dBi, respectively. At 2.5 GHz, the gains of the three antennas are 5.1 dBi, 2.3 dBi, and 5.0 dBi, respectively.



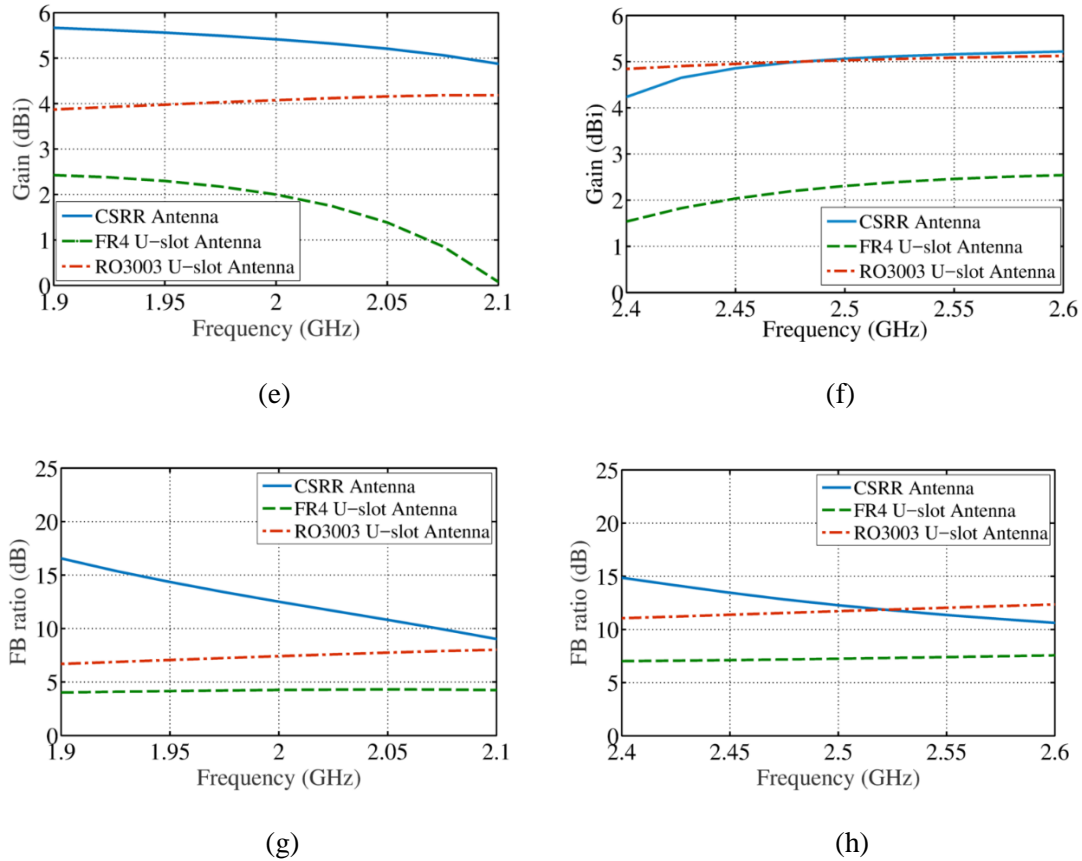


Figure 3-13. Configurations of (a) proposed antenna, (b) FR-4, and (c) RO4003 U-slot patch antennas. Comparisons of (d) S_{11} , gain performances at (e) lower and (f) higher bands, and FB ratios at (e) lower and (f) higher bands among the three antennas.

As shown in Figure 3-13(f), the simulated FB ratios at 2.0 GHz of the MS artificial ground plane based, the FR4-based, and the RO3003-based patch antennas are 12.5 dB, 4.3 dB, and 7.3 dB, respectively. As presented in Figure 3-13(h), the simulated FB ratios at 2.5 GHz of the MS artificial ground plane based, the FR4-based, and the RO3003-based patch antennas are 12.3 dB, 7.3 dB, and 11.7 dB, respectively. Thus, within the 2.0 GHz frequency band, our antenna has the highest gain and FB ratio. As for the 2.5 GHz frequency band, it is observed that the proposed antenna still provides the highest FB ratio and an antenna gain similar to that of the RO3003 based-antenna but much better than that of the FR4-based antenna. The sacrifice made to achieve these superior radiation characteristics is the relatively narrow bandwidth of our proposed antenna.

It is worth mentioning that the proposed dual-band antenna can be further miniaturized by appropriately tuning the corresponding design parameters based on the individual band tuning techniques discussed in the previous section. For example, by either reducing the thickness of the first MS layer d_{u1} , or slightly increasing the thickness of the second MS layer d_{u2} , or the width of the CSRR L_C , both operational bands can be tuned to lower frequencies.

3.5 Experimental Results

To experimentally verify the proposed dual-band MS artificial ground plane enabled integrated antenna design, an antenna prototype is fabricated, assembled, and measured. The antenna prototype is shown in Figure 3-14.



Figure 3-14. Antenna prototype of the proposed dual-band MS artificial ground plane enabled integrated antenna.

Figure 3-4 shows the measured impedance matching performance of the proposed dual-band antenna as a solid S_{11} curve. A good agreement between the simulated and measured results is observed. Two measured operational bands are centered at 1.89 and 2.51 GHz, respectively. The slight band shifts toward the higher frequency ranges of both operational bands are due to fabrication errors such as the introduction of air layers in the MS artificial ground plane when the RO3003 laminates are put together. As shown in the previous sections, varying the thickness of the

MS artificial ground plane results in the band shift of both operational bands. The measured $S_{11} < -10$ dB bandwidth for the first operational band is 110 MHz ranging from 1.84 GHz to 1.95 GHz, which is equivalent to a fractional bandwidth of 5.8%. The measured $S_{11} < -10$ dB bandwidth for the second operational band is 100 MHz ranging from 2.46 GHz to 2.56 GHz, which is equivalent to a fractional bandwidth of 4.0%. The measured operational bands are within the frequency spectrum of the GSM-1900 mobile communication frequency band and the industry, scientific, and medical (ISM) frequency band. Hence, the proposed antenna can possibly be integrated into communication systems where the two bands are accommodated. It is worth mentioning that, by tuning the design parameters, the operational bands of the proposed antenna can be tuned to support other frequency bands.

The measured gain profiles of the proposed dual-band antenna are presented in Figure 3-5(a) and Figure 3-5(b) as solid curves. Obviously, the measured results correspond well with the simulated ones. In addition, as can be seen, within the first operation band, the measured gain varies from 3.2 to 5.3 dBi, with the peak gain at 1.92 GHz. As for the second operation band, the measured gain varies from 3.3 to 4.8 dBi, with the peak gain at 2.53 GHz. The reasons for the small gain drops of the measured results and the ripples along the measured gain profiles are as follows. The first reason is the existence of unwanted loss and radiation from connecting cables used during the antenna measurements. The second reason is the existence of interference noises. The final reason is the fabrication imperfections such as thickness variation as well as extra loss due to the thin adhesive layers introduced when dielectric laminates are assembled.

Figure 3-6(a) and Figure 3-6(b) illustrate the measured radiation patterns at 1.9 and 2.5 GHz, respectively, on both the E -plane and H -plane as solid red curves. The measured HPBW_s at 1.9 GHz are 105° and 93° on the E -plane and H -plane, respectively. The measured HPBW_s at 2.5 GHz are 108° and 120° on the E -plane and H -plane, respectively. The measured cross-polarization patterns are well suppressed for both bands. The measured FB ratios at both 1.9 and

2.5 GHz are all above 6 dB. Hence, the majority of the radiated power is along the broadside with suppressed back radiation and cross-polarization at both bands.

A comparison can be made between the proposed MS artificial ground plane based dual-band antenna and its counterparts already reported in the literature, as shown in Table 3-3. All the reported antennas possess dual-band or multi-band functionality enabled by MSs and unidirectional radiation patterns along the broadside at all bands. In the first place, the proposed MS artificial ground plane enabled dual-band antenna has the smallest footprint. It should be noted that λ_0 is the wavelength in free space at the lower band frequency for each antenna. Despite the small footprint, the operational bands of the proposed antenna are wider than most of its counterparts' bands. Only the antennas reported in [26] and [55] have wider second operational bands. However, the bandwidths of their first operational bands are narrower. When it comes to gain performances, the proposed antenna provides a higher gain at the lower band compared to all its counterparts except for the antenna reported in [26]. This is because the antenna in [26] has a very large footprint that is almost 15 times larger than that of the proposed antenna in this chapter. Moreover, the proposed antenna has a more balanced gain profile between the first and the second band compared to all the other antennas. Specifically, the smallest gain difference between the first and second band is achieved by the proposed antenna; this gain difference is only 0.37 dBi. In conclusion, these comparisons reveal that the proposed MS artificial ground plane enabled dual-band antenna achieves the smallest footprint while still maintaining wide operational band and moderate gains at both operational bands.

Table 3-3. Comparison of Dual-Band and Multi-Band Antennas Enabled by MS.

	Freq. (GHz)	Freq. Ratio	S_{11} BW (%)	AR BW (%)	Gain (dBi/c)	FBTR (dB)	Footprint (λ_0^2)
[23]	1.34/2.38	1.78	1.72/4.54 (-6dB)	-	1.8/5.9	7.5/13	0.1

[23]	1.33/2.41	1.81	1.88/10.03 (-6dB)	- /1	2.1/5.7	8/10	0.1
[26]	2.45/5.8	2.37	4/12	-	6.4/7.6	> 10	0.96
[47]	2.86/3.1	1.08	1.75/2.57	1.05/1.61	4.15/4.77	-	0.18
[55]	1.75/4.06	2.32	- /6	-	1.2/6.86	15	0.08
[56]	2.41/3.82	1.59	0.91/1.76	-	-2.1/5.04	5.2/13	0.074
[56]	2.39/2.96	1.24	1.32/2.68	-	0.21/3.13	8.2/14	0.077
[56]	2.31/2.83	1.23	1.38/3.29	-	-2.1/3.85	8.3/14	0.07
[58]	2.4/2.9	1.21	2.1/3.45	-	2.25/3.11	6/10	0.078
This Work	1.9/2.5	1.32	5.8/4.0	-	4.52/4.15	> 6	0.062

3.6 Conclusion

In this chapter, the design methodology of an MS artificial ground plane enabled miniaturized dual-band antenna with unidirectional radiation patterns along the broadside at both bands was introduced and explained. The MS artificial ground plane was proven not only to provide dual-band functionality, but also to achieve antenna performance enhancements in numerous aspects including bandwidth, FB ratio, and gain. The working principles of the proposed antenna were explained by the dispersion analysis of a single MS unit cell. It was found that the self-resonance of the unit cell resulting from the resonating CSRR structure actually enables the two operational bands of the proposed antenna. The significant size reduction of the proposed antenna can also be attributed to the CSRR structure. The methods for independently tuning each operational band were explored, making the antenna more flexible for integration into different communication systems with different frequency requirements. Finally, an antenna prototype was

fabricated and tested to validate the antenna design. Good agreement was observed between the simulated and measured results. A comparison between the proposed antenna in this chapter and other MS-enabled dual-band antennas reported in the literature reveals that the proposed antenna has numerous desirable features that are preferred in modern communication systems [63].

Chapter 4

A Compact Dual-Band Dual-Sense Circularly-Polarized Antenna Enabled by a CSRR Loaded Metasurface

4.1 Introduction

In order to increase the capacity of modern communication systems, more than one frequency band is often used to accommodate multiple communication channels. As a result, increasing research has been devoted to developing antennas with more than one operational frequency band. Instead of using multiple antennas in a system, a single dual-band or multi-band antenna can achieve size reduction by sharing different communication channels within one antenna aperture. Recently, dual-band or multi-band antennas are widely used in many communication systems, such as multifunctional radar systems and satellite communication systems.

On the other hand, to avoid the multipath fading effect commonly seen in communication systems, and to release the restriction on the relative positions of transmitting and receiving antennas, CP antennas are more suitable for certain applications such as transmitting nodes in radio frequency identification (RFID) systems than the linearly-polarized (LP) antennas. Therefore, a dual-band CP antenna is very attractive for modern compact communication systems. As a result, dual-band CP antennas are now widely used in numerous applications such as GPS [64-75], RFID [76-81], WLAN [81-83], and satellite communications [84-88].

There are many dual-band CP antennas reported in the literature, including slot antennas [89-92], cavity-backed antennas [69, 73, 75, 82, 93-95], and antennas with properly designed feeding networks [64, 68, 74, 76-80, 85, 96-102]. The dual-band slot antennas can provide wide

axial ratio (AR) < 3 dB operational bands but their bi-directional radiation patterns limit their gain performances. The cavity-backed antennas possess unidirectional radiation patterns along the broadside, but the introduction of the cavity significantly increases antenna profiles. The dual-band antenna designs with extra feeding networks eliminate the usage of cavities to achieve unidirectional radiation patterns. However, the high insertion losses introduced by the complicated networks result in lower antenna efficiency.

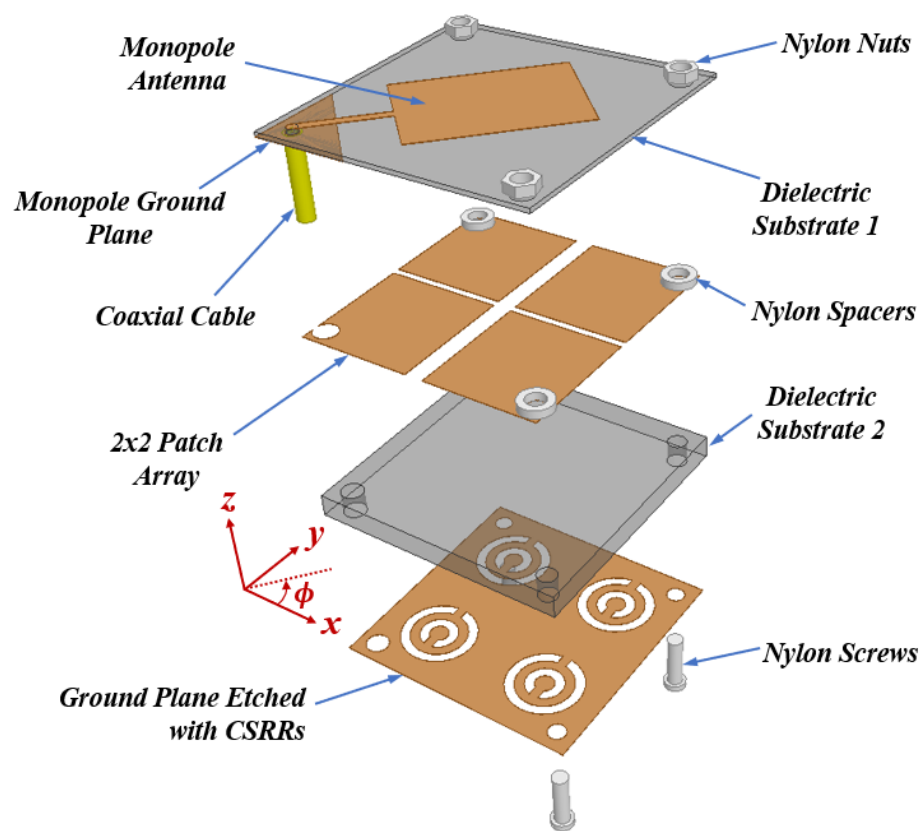
There are also low-profile antennas reported with unidirectional radiation patterns along the broadside that do not need extra feeding networks. [65, 66, 70-72, 81, 83, 84, 86-88, 103-114]. These antenna design methods can be categorized into three classes. In the first class, the different shapes of slots are cut on conventional patch antennas either to break the symmetry of the antenna structure or to introduce additional orthogonal mode at two bands. The second design method is to stack parasitic antennas on top of the original antenna. The final design method is applying metasurfaces (MSs) into dual-band CP antenna engineering. One example is reported in [81], where a dual-band CP antenna is proposed by integrating a dipole antenna with artificial magnetic conductor (AMC) surface.

Among the dual-band CP antennas, only a small number of antennas with distinct sense of polarization at the two bands are reported [84, 87, 88, 90, 91, 101, 108, 111-114]. Within this category, dual-band dual-sense CP antennas are actually very preferable in some applications where high isolation between the two bands are required, as in satellite communications. For example, two slot antennas were reported in [90, 91] with two different senses of CP polarization achieved at the two operational bands. However, as mentioned, their gains are relatively low. Stacked patch with or without slot loadings were reported [84, 87, 101, 108, 112, 113] to be able to provide dual-band dual-sense CP functionality. However, they all suffer from narrow operational bandwidths. By virtue of MSs, antennas [111, 114] were also capable of providing dual-band dual-sense unidirectional CP radiation.

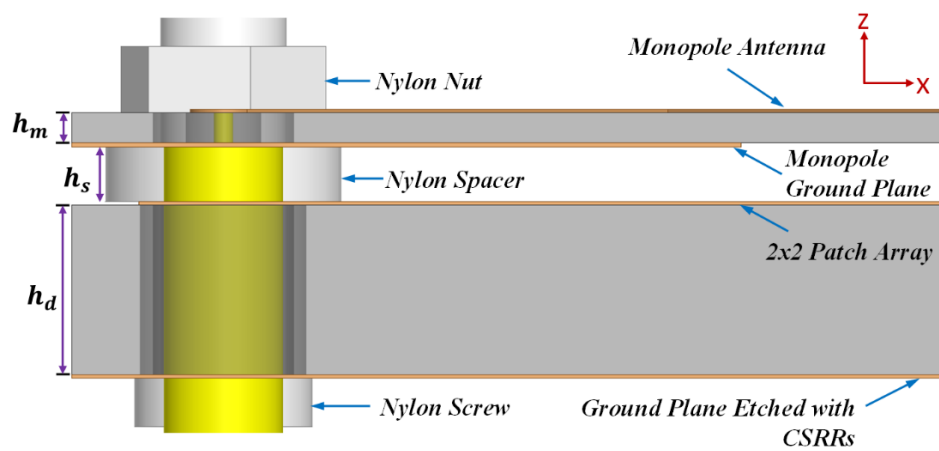
In this chapter, a novel dual-band dual-sense CP antenna design is proposed with low antenna profile and without any extra feeding networks.

4.2 Antenna Design

Figure 4-1(a) and Figure 4-1(b) show the 3D exploded and side views of the proposed dual-band dual-sense CP antenna. It can be seen that the proposed antenna consists of two parts similar to the MS artificial ground plane enabled antennas proposed in previous chapters. The first part is a printed planar monopole antenna serving as the feeding element while the second part is a MS below it acting as the main radiating element. There is an air gap between the two elements to realize the reactive coupling between them. The monopole antenna is a rectangular metallic patch fed by a 50Ω microstrip line. Both the rectangular patch and the transmission line are printed on a Rogers RO4003 laminate with a relative dielectric constant $\epsilon_r = 3.55$ and a loss tangent $\tan\delta = 0.0027$. Figure 4-1(c) presents the top and bottom views of the monopole antenna. The MS is actually a 2×2 periodic unit cell array with each unit cell consisting of a rectangular metallic patch and a CSRR resonator printed on the top and bottom surfaces of a RO4003 laminate. In order to achieve mechanical robustness of the proposed antenna, nylon nuts, spacers, and screws are adopted as illustrated in Figure 4-1(a).



(a)



(b)

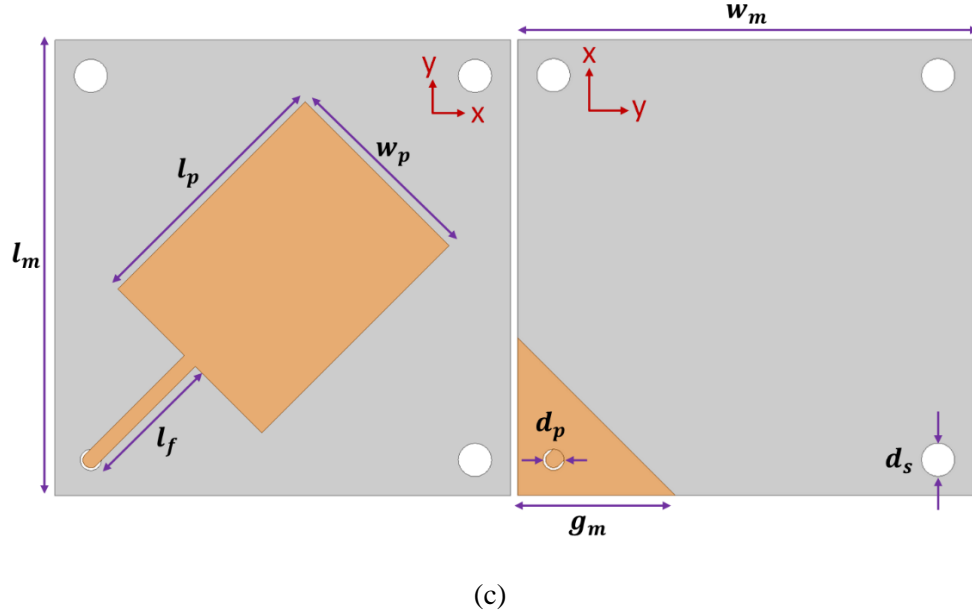


Figure 4-1. (a) 3D exploded and (b) side views of the proposed antenna. (c) Top (left) and bottom (right) views of the monopole antenna.

4.3 Unit Cell Analysis

The configuration of a single unit cell extracted from the MS is shown in Figure 4-2(a). As proven in previous chapters, for MS artificial ground plane enabled antennas, the MS artificial ground plane is the actual radiator reactively excited by the planar monopole antenna above it. Moreover, the resonant frequencies of the MS and also the integrated antennas can be predicted accurately by investigating the dispersive behavior of a single unit cell and approximating the MS resonator to a rectangular microstrip patch antenna.

However, unlike the designs proposed in previous chapters, two orthogonal modes are excited simultaneously for the proposed antenna design, which is illustrated in Figure 4-3. As shown, the E -field \mathbf{E}_m generated by the monopole antenna can be decomposed as $\mathbf{E}_m = \hat{x}E_{\perp} + \hat{y}E_{\parallel}$, where E_{\perp} and E_{\parallel} represent the decomposed E -fields perpendicular and parallel to the symmetrical line of the CSRR, respectively. When the MS is excited by \mathbf{E}_m , two orthogonal

resonant modes are excited, and they are similar to the TM_{10} and TM_{01} modes of a rectangular patch antenna.

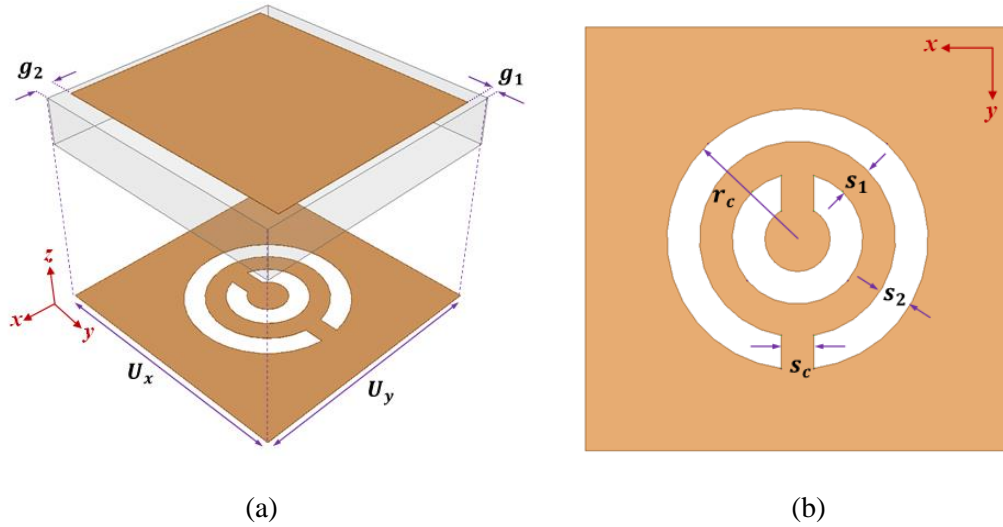


Figure 4-2. (a) Configuration of a single unit cell. (b) Detailed dimensions of the CSRR resonator.

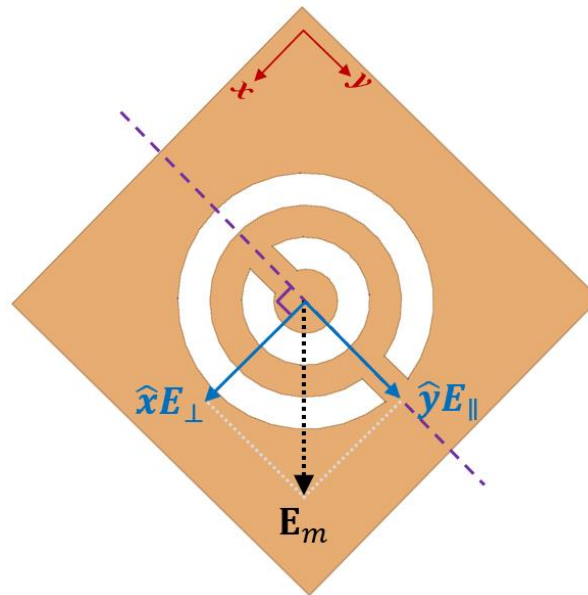


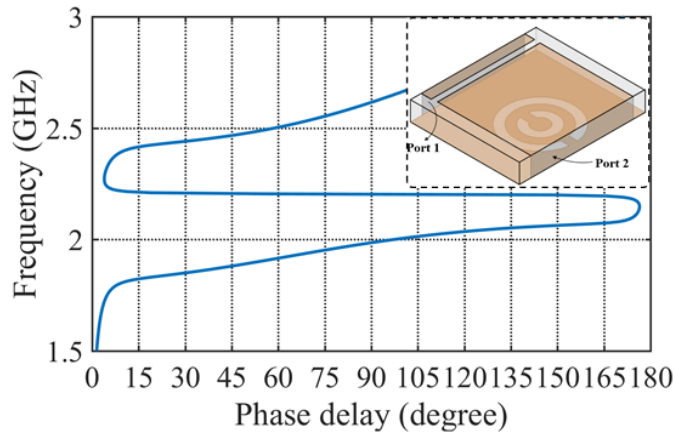
Figure 4-3. Field decomposition of \mathbf{E}_m .

It is intuitive to say that if the two orthogonal modes can be excited to have almost the same magnitudes but a 90-degree phase difference at certain frequency f , a CP radiation can be achieved. In terms of a patch antenna, this means that the two resonant frequencies f_{01} and f_{10} of

the TM_{10} and TM_{01} modes must satisfy either $f_{01} < f < f_{10}$ or $f_{10} < f < f_{01}$ with f_{01} and f_{10} close to each other. In addition, the sense of CP polarization is determined by the sign of $f_{01} - f_{10}$.

Thus, for the proposed antenna to provide dual-band functionality at two bands f_a and f_b , two orthogonal modes resonating at f_{01}^a and f_{10}^a and the other two orthogonal modes at f_{01}^b and f_{10}^b must be excited. Moreover, for the CP radiations at f_a and f_b to have a distinct sense of polarization, the signs of $(f_{01}^a - f_{10}^a)$ and $(f_{01}^b - f_{10}^b)$ must be different and not equal to 0. In fact, the following dispersive unit cell analysis reveals that the two conditions can be satisfied by the proposed MS in this chapter. As is later shown, the self-resonance of the CSRRs and their bi-anisotropic characteristics contribute to the dual-band functionality and dual-sense CP radiation, respectively.

The simulation models of the unit cell dispersion analysis of the two orthogonal resonant modes are shown as the insets in Figure 4-4(a) and Figure 4-4(b). Similar to the unit cell simulations in previous chapters, in each model, two lumped ports are applied to the two faces of the unit cell parallel (Figure 4-4(a)) or perpendicular (Figure 4-4(b)) to the symmetrical line of the CSRR resonator. It should be noted that in these two simulations, the metallic patch on the top surface of the unit cell is of a square shape with g_1 and g_2 equal to 0.75 mm so that only the bi-anisotropic effect of the CSRR resonator is investigated.



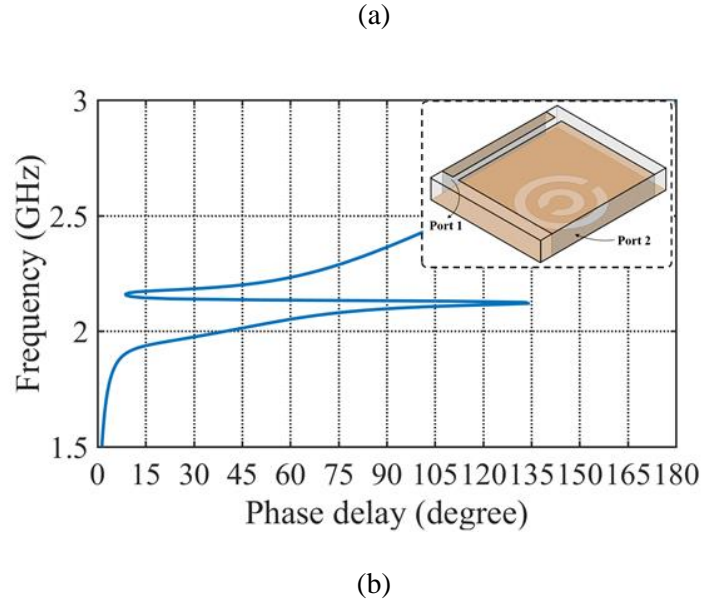


Figure 4-4. Dispersion behavior of a single unit cell with wave propagating (a) parallel and (b) perpendicular to the symmetrical line of the CSRR resonator.

The simulated dispersive curves of the two resonant modes of the MS are shown in Figure 4-4. It is obvious that because of the bi-anisotropic characteristic of the CSRR resonator, the two dispersive curves are distinct from each other. Specifically, the resonant frequencies can be predicted based on the following equation:

$$N \times P = n\pi \quad (4-1)$$

where N is the number of unit cells along directions parallel or perpendicular to the symmetrical line of the CSRRs, and P is the associated phase delay introduced by a single unit cell along the directions. As will be shown, only the fundamental TM mode is of practical interest; therefore n is assigned to be equal to 1. Based on Eq. (4-1), the resonant frequencies are the vertical coordinate of the points along the dispersive curves with horizontal coordinate equal to $\pi/2$.

Consequently, the resonant frequencies are predicted to be $f_{01}^a = 1.98$ GHz, $f_{10}^a = 2.10$ GHz, $f_{01}^b = 2.62$ GHz, and $f_{10}^b = 2.36$ GHz. The aforementioned conditions for the generation of the dual-band dual-sense polarization are all satisfied. Based on the discussion above, CSRRs are

the key elements to realize dual-band dual-sense CP radiation, because they not only split the dispersive curve into two band by virtue of their self-resonance, but also give rise to distinct dispersive behaviors of the two orthogonal TM modes as a result of their bi-anisotropic characteristics.

To further prove that dual-sense CP radiation is enabled by the bi-anisotropic behavior of the CSRR, dispersive analysis of a non-bianisotropic CSRR (NBCSRR) loaded unit cell is carried out. The configuration of the NBCSRR and the simulated results are shown in Figure 4-5. Except for the replacement of the CSRR by the NBCSRR, all other design parameters of the NBCSRR unit cell are kept the same as those of the CSRR loaded unit cell. The results show that the dispersive curves are the same for both modes, indicating that only LP radiation can be achieved for the two operational bands if the MS is loaded with NBCSRR resonators.

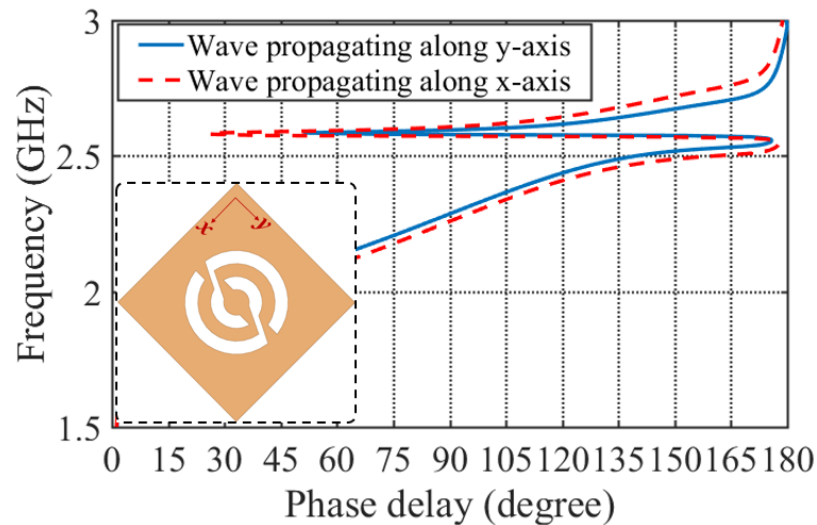


Figure 4-5. Dispersion behavior of a unit cell loaded with NBCSRR.

Similar to the field analyses in previous chapters, the E -field distributions within the MS artificial ground plane are also investigated (not shown here), and prove the similarity between the resonant modes of the MS artificial ground plane and those of a conventional rectangular patch antenna.

4.4 Simulated Antenna Performances

The detailed antenna dimensions associated with Figure 4-1 and Figure 4-2 are summarized in Table 4-1.

Table 4-1. Detailed Dimensions of the Proposed Dual-Band Dual-Sense CP Antenna (all in mm).

h_m	h_s	h_d	l_m	w_m	l_f	l_p	w_p	d_p	d_s
0.81	1.57	4.56	52	52	16	30.2	23.2	2.36	3.8
g_m	U_x	U_y	g_1	g_2	r_c	s_1	s_2	s_c	
18	26	26	0.75	1.8	2	0.8	0.8	0.8	

The simulated impedance matching performance of the proposed antenna is presented in Figure 4-6. Two resonances are observed at 1.9 and 2.4 GHz, giving rise to two $S_{11} < -10$ dB frequency bands. The simulated bandwidth of the first frequency band is equal to 150 MHz ranging from 1.81 to 1.96 GHz. This is equivalent to a fractional bandwidth of 8.0%. The second $S_{11} < -10$ dB impedance matching band is 250 MHz ranging from 2.30 to 2.55 GHz, which is equivalent to a fractional bandwidth of 10.3%. It should be noted that there is an additional narrow band centered at 2.06 GHz in between the two operational bands. This is the combination of higher order modes within the first dispersive band and the self-resonance of the unit cell as illustrated in Chapter 3.

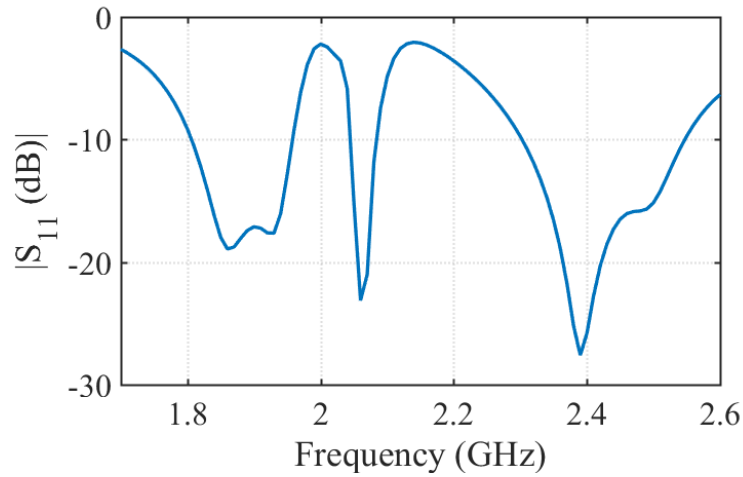


Figure 4-6. Simulated S_{11} of the proposed dual-band dual-sense CP antenna.

The simulated broadside AR performance of the proposed antenna is presented in Figure 4-7. It can be seen that the proposed antenna has two AR < 3 dB bands centered at 1.90 and 2.47 GHz, respectively. The simulated bandwidth of the first AR < 3 dB frequency band is equal to 50 MHz ranging from 1.87 to 1.92 GHz. This is equivalent to a fractional bandwidth of 2.6%. The second AR < 3 dB band is 30 MHz ranging from 2.45 to 2.48 GHz, which is equivalent to a fractional bandwidth of 1.2%. Therefore, the simulated $S_{11} < -10$ dB bands fully cover the AR < 3 dB bands. Thus, the simulated operational bands of the proposed antenna are the same as the simulated AR < 3 dB bands.

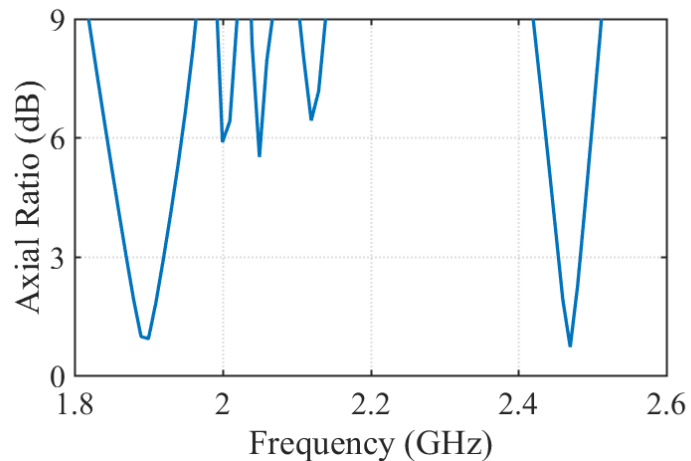
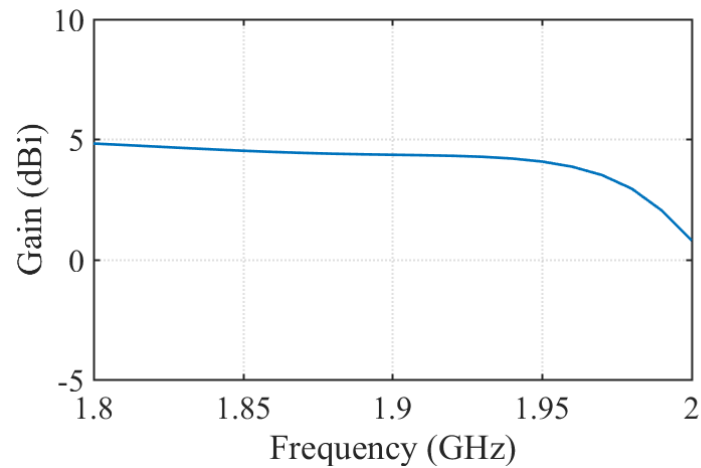
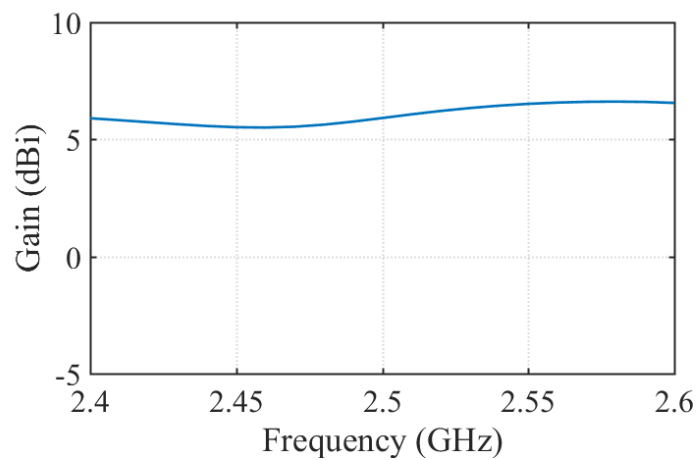


Figure 4-7. Simulated broadside AR performance of the proposed antenna.

The simulated broadside gain performances for the two operational bands are plotted in Figure 4-8(a) and Figure 4-8(b), respectively. Within the first operational band, the broadside antenna gain varies from 4.31 to 4.43 dBi. Within the second operational band, the broadside antenna gain is from 5.52 to 5.63 dBi.



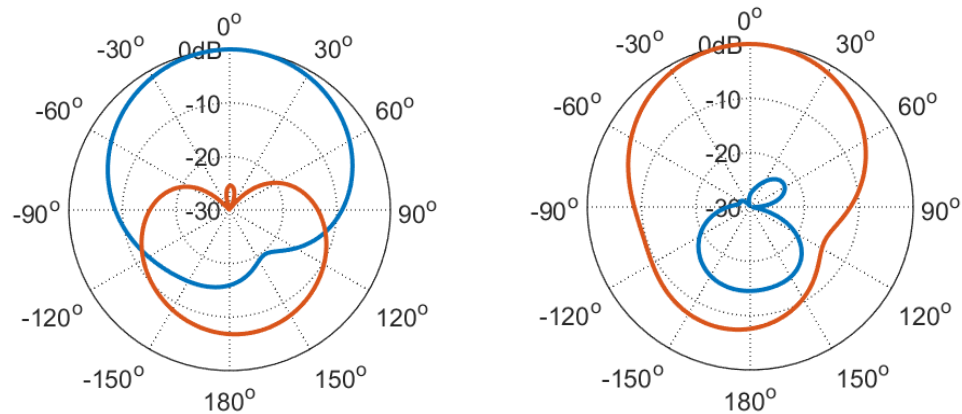
(a)



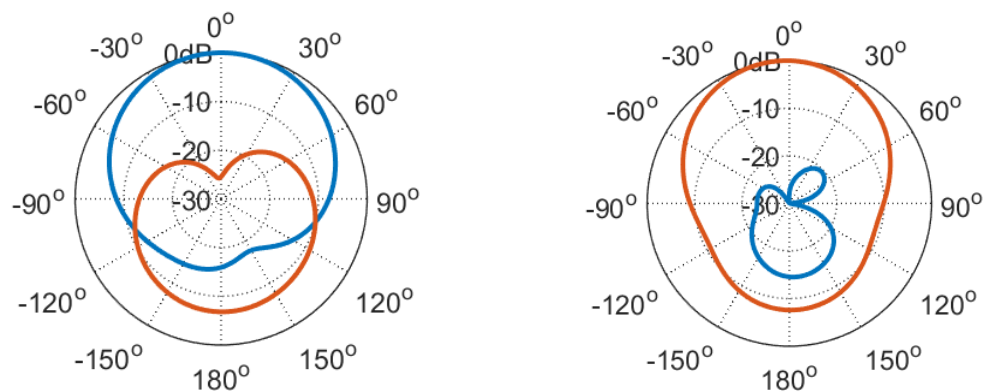
(b)

Figure 4-8. Simulated broadside antenna gains of the proposed antenna at the (a) first and (b) second operational bands.

The simulated normalized radiation patterns of the proposed antenna on both $\phi = 45^\circ$ and $\phi = 135^\circ$ planes (see Figure 4-1(a) for the definition of ϕ) at 1.90 and 2.47 GHz are plotted in Figure 4-9(a) and Figure 4-9(b), respectively. The right-handed CP (RHCP) radiation patterns are represented by the blue lines while the left-handed CP (LHCP) radiation patterns are depicted by the red lines. It can be seen that two distinct senses of CP polarization are achieved at the two operational bands. Specifically, RHCP is achieved at the lower band while LHCP is realized at the higher band. Moreover, unidirectional patterns with the peak gain along the broadside and suppressed back radiations are accomplished for both bands. On $\phi = 45^\circ$ plane, the simulated HPBWs are 99° and 90° at 1.90 and 2.47 GHz, respectively. On $\phi = 135^\circ$ plane, the simulated HPBWs are 103° and 98° at 1.90 and 2.47 GHz, respectively.



(a)



(b)

Figure 4-9. Simulated normalized radiation patterns on (a) $\phi = 45^\circ$ and (b) $\phi = 135^\circ$ planes at 1.90 (left) and 2.47 (right) GHz.

4.5 Conclusion

In this chapter, the design methodology of a dual-band dual-sense CP antenna was introduced. An MS was designed, serving as an artificial ground plane of the proposed integrated antenna. The CSRRs not only achieve the significant antenna size reduction, but also introduce the dual-band dual-sense CP radiation functionality. The antenna working principle was revealed by the dispersive analysis of a single unit cell extracted from the MS. Modest operational bandwidths and moderate broadside gains are achieved at both bands. Unidirectional radiation patterns are generated by the antenna at the two operational bands with well suppressed back radiations. In summary, the proposed antenna is a promising candidate for integration into modern multi-channel communication systems.

Chapter 5

A Novel Wearable Quarter-Mode Substrate Integrated Waveguide Antenna Design Enabled by Flexible Materials

5.1 Introduction

5.1.1 SIW Antenna

Since the SIW slot array antenna was first proposed in [115], numerous SIW-based antennas have been proposed by researchers and engineers. For example, in [116], by virtue of the multimode SIW feeding technology, a dual V-type linearly tapered slot antenna was proposed which is suitable for monopulse antenna applications. In [117], an SIW-based leaky wave antenna was proposed for millimeter-wave band. Another example is an H -plane horn antenna based on SIW technology as presented in [118].

The SIW cavity-backed antennas were also proposed and implemented into many applications. For example, in [119], a low-profile SIW cavity-backed antenna was reported, based on the TE_{120} mode of the SIW cavity. This antenna was a single slotted SIW cavity fed by the grounded CPW (GCPW) feeding method. Another SIW-cavity backed antenna was reported in [120], where a patch antenna is backed with a circularly-shaped SIW cavity. Compared to conventional patch antenna design, the proposed SIW cavity-backed patch antenna achieves both efficiency and bandwidth enhancements.

Similar to the relationship between rectangular SIW and traditional metallic rectangular waveguide described in Chapter 1, there is equivalence between SIW-based rectangular cavity and traditional metallic rectangular cavity. Here, the length and width of the SIW cavity are denoted as

L_{SIW} and W_{SIW} , respectively, and the thickness of the SIW cavity is denoted as t . The resonant frequency of an SIW rectangular cavity with operating in TE_{mnl} ($m = 1, 2, \dots; n = 1, 2, \dots; l = 0, 1, \dots$) mode can be derived based on Eq. (1-3) and written as

$$f_{mnl} = \frac{c}{2\sqrt{\epsilon_r \mu_r}} \sqrt{\left(\frac{m}{L}\right)^2 + \left(\frac{n}{W}\right)^2 + \left(\frac{l}{t}\right)^2} \quad (5-1)$$

$$L = L_{\text{SIW}} - 1.08 \frac{d^2}{p} + 0.1 \frac{d^2}{L_{\text{SIW}}} \quad (5-1a)$$

$$W = W_{\text{SIW}} - 1.08 \frac{d^2}{p} + 0.1 \frac{d^2}{W_{\text{SIW}}} \quad (5-1b)$$

It should be noted that Eq. (5-1) only provides approximated resonant frequency for SIW cavity-backed slot antenna design, because the introduction of the slot along with the feeding structure modifies the cavity configuration, and thus results in frequency shift.

In order to realize size reduction, antennas based on half mode SIW (HMSIW) was proposed. The HMSIW-based cavity possesses only half the footprint of its SIW-based [118, 121] counterparts. In [122], a HMSIW cavity-backed LP antenna was reported to have a compact form factor while maintaining the advantages of SIW cavity-backed antennas. To further miniaturize antenna volumes, a QMSIW-based cavity, which requires only a quarter sector of an SIW-based cavity, was adopted. For example, a QMSIW-based antenna was proposed in [123]. For another example, in [124], a CP QMSIW cavity-backed antenna was reported.

5.1.2 SIW Wearable Antenna

The SIW-based antenna designs are combined with textile material systems to offer antenna solutions to wearable communication systems. The low profile and high isolation between the SIW-based antenna and its surroundings make the SIW-based antennas promising candidates for wearable applications.

There are several SIW-based wearable textile antenna reported in the literature. The first textile SIW-based antenna design was reported in [125], where an SIW cavity-backed slot antenna is implemented with the closed-cell expanded rubber protective foams with a dielectric constant $\epsilon_r = 1.495$ and a loss tangent $\tan\delta = 0.016$. Conductive fabrics are used as antenna metallic layers. In [126], a HMSIW textile antenna was proposed with the dual-band functionality to cover 2.4 and 5.8 GHz ISM bands. This antenna was fabricated using closed-cell expanded rubber protective foams. The copper-plated polyester taffeta fabrics were used to construct the antenna conducting layers. In [128], a QMSIW antenna was proposed, operating within the 2.4 GHz ISM band. The antenna was also fabricated with flexible closed-cell expanded rubber protective foam as its dielectric substrate. A conductive e-textile copper-plated polyester taffeta fabric was used to form the metallic layer. To realize antenna size reduction, a metamaterial inspired SIW textile antenna was proposed in [130], based on wool felt with a dielectric constant $\epsilon_r = 1.4$ and a loss tangent $\tan\delta = 0.0254$.

Among the aforementioned textile antenna designs, the vertical electroplated via holes of SIW structures are all realized by metallic eyelets. However, in [127], a HMSIW textile antenna was proposed with embroidered vias. In addition, the substrate used in this antenna design is a low-loss nonabsorbent foam with a dielectric constant $\epsilon_r = 1.06$. The metallic layers were realized by conductive fabrics. In [129], a dual-band textile QMSIW antenna was proposed to cover both 2.4 and 5.8 GHz ISM bands. In this design, the vertical electroplated via holes were directly realized by a solid piece of the ShieldIt super conducting textile whose dielectric substrate is a 3 mm-thick felt with a dielectric constant $\epsilon_r = 1.3$ and a loss tangent $\tan\delta = 0.044$.

5.2 Flexible QMSIW Antenna Design with Novel Flexible Materials

Figure 5-1 shows the simulation model for a conventional square QMSIW antenna. The EGaIn liquid metal is used to build up the flexible metallic wall to mimic vertical electroplated via holes of a QMSIW cavity. The flexible dielectric substrates are the SEBS polymer with a dielectric constant $\epsilon_r = 2.52$ and a loss tangent $\tan\delta = 0.00045$. The thickness of the QMSIW cavity is 6.3 mm. The thickness of the SEBS substrate where the microstrip feeding line is printed is 0.508 mm. Another 0.508 mm-thick SEBS substrate is attached below the microstrip feeding line to isolate it from human body. A vertically oriented EGaIn probe connecting the top metallic patch of the QMSIW and the microstrip feeding line is used to excite the QMSIW resonant cavity. There is a circular disc etched off from the antenna ground plane to let the probe go through.

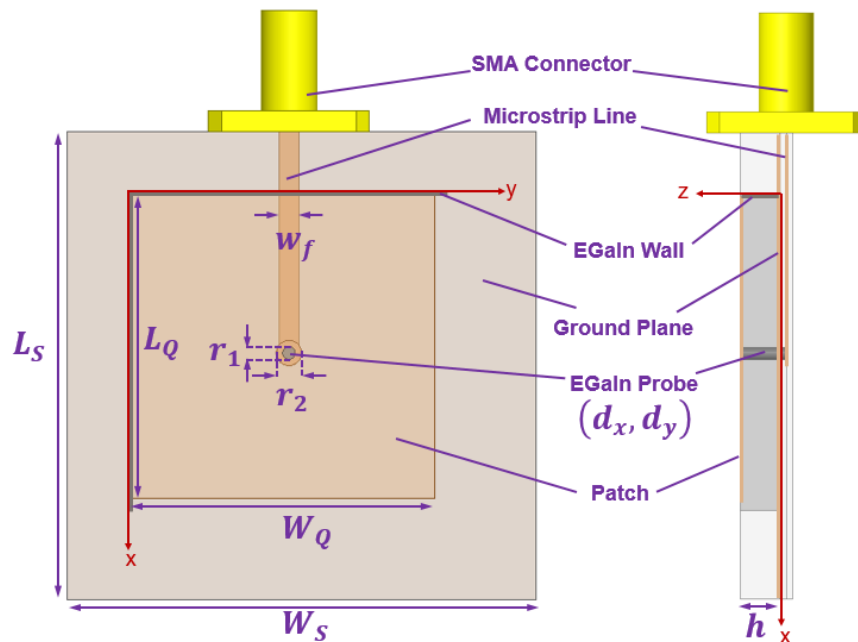


Figure 5-1. Configuration of a conventional QMSIW antenna with equal length and width.

A parametric study is carried out on (d_x, d_y) to investigate the effect of the position of the feeding probe on the resonant frequency and the input impedance matching of the QMSIW antenna. The simulated results are plotted in Figure 5-2(a) and Figure 5-2(b) for the resonant frequency and

the impedance matching performance of the QMSIW, respectively. In Figure 5-2, $f_x = \frac{d_x}{L_Q}$ and $f_y = \frac{d_y}{L_Q}$. It should be noted that the frequency range in the parametric study is from 2.3 to 2.8 GHz, thus when the probe is near the open corner ($f_x, f_y \rightarrow 1$) of the QMSIW antenna, the actual resonance of the antenna is above 2.8 GHz. In Figure 5-2, a red-dashed curve is also plotted. When the feeding probe is at positions represented by the red curve, the impedance of the antenna is well matched at around 2.5 GHz. It is concluded that the distance between the feeding position and the open corner of the QMSIW antenna determines both resonant frequency and impedance matching. Specifically, when the distance is larger, the resonant frequency shifts toward lower frequency band, but the impedance matching is degraded. This conclusion serves as a guideline for the following QMSIW antenna design.

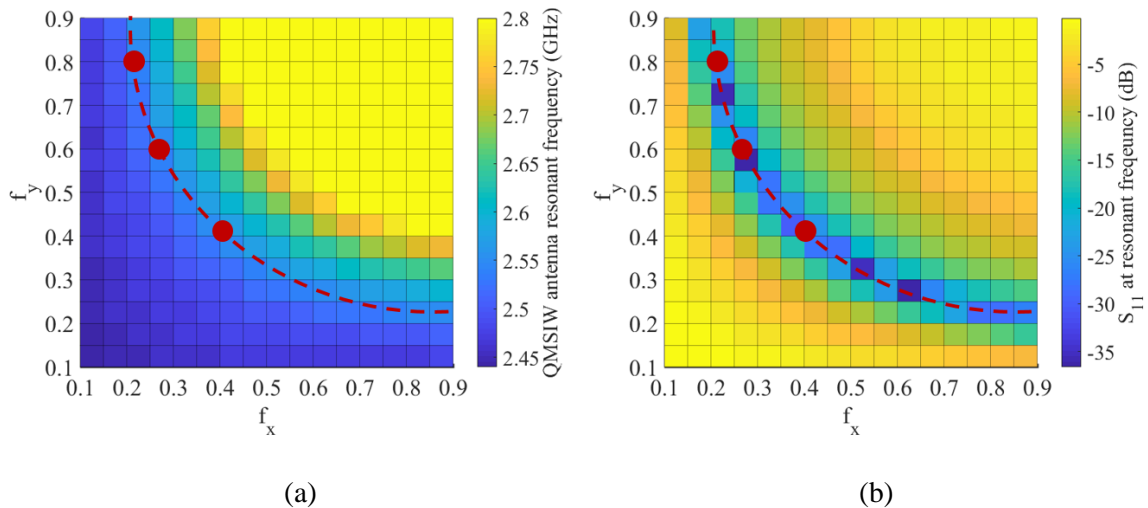


Figure 5-2. The simulated (a) resonant frequency and (b) S_{11} at the resonant frequency of the QMSIW antenna.

Along the red-dashed line in Figure 5-2, three sampling points with (f_x, f_y) equal to (0.2, 0.8), (0.25, 0.6), and (0.35, 0.4) are investigated. The corresponding simulated S_{11} performances of the QMSIW antenna are shown in Figure 5-3. The results show that the quality-factor of the

QSMIW cavity antenna is independent from the position of the probe as long as the coordinate (f_x, f_y) is on the red-dashed line shown in Figure 5-2.

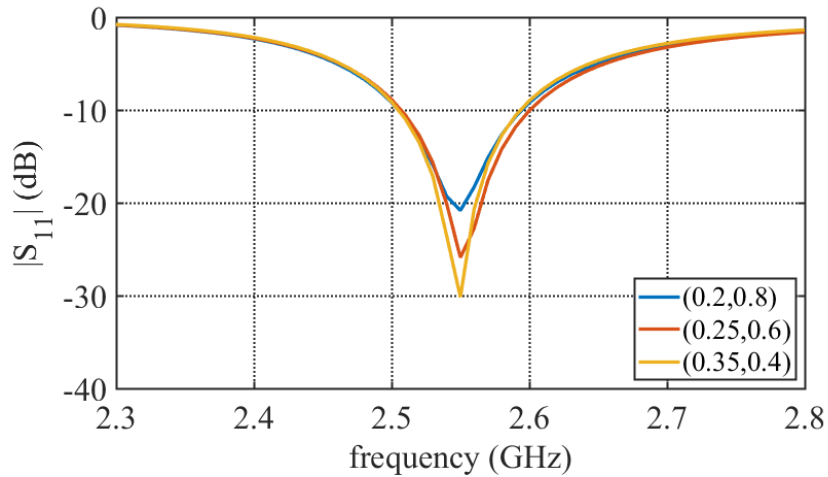


Figure 5-3. Simulated S_{11} performances of the QSMIW antenna with different feeding positions.

It is well known that one method to increase the bandwidth of a microstrip patch antenna is to stack an additional parasitic antenna element above the original one. However, to the author's best knowledge, the stacked QSMIW antenna has not been reported yet. The design methodology of a stacked wearable flexible QSMIW antenna with bandwidth enhancement is explored in the rest of this Chapter.

Figure 5-4 shows the configuration of a stacked flexible QSMIW antenna. The thickness of the SEBS layer where the feeding microstrip line is printed on is 0.508 mm. Another 0.508 mm-thick SEBS substrate is attached below the feeding network to provide isolation from human body.

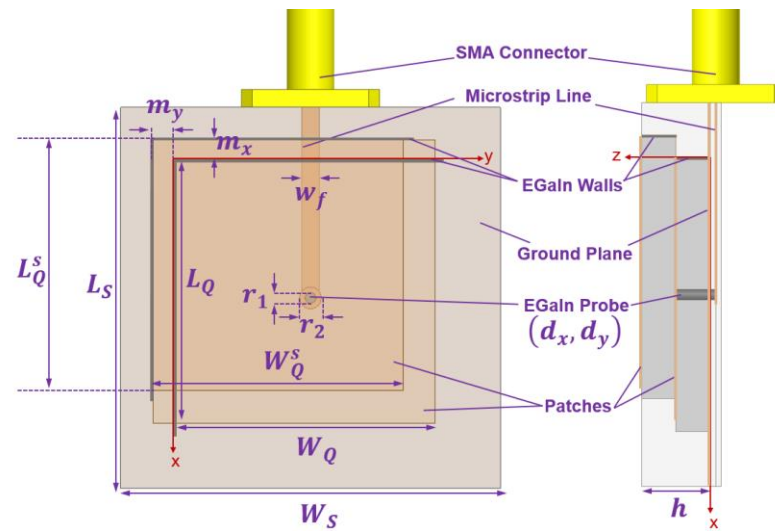


Figure 5-4. Configuration of the stacked QMSIW antenna.

A preliminary simulated S_{11} of the stacked QMSIW antenna is shown in Figure 5-5, with detailed dimensions listed in the figure caption. A comparison of Figure 5-5 and Figure 5-3 shows that the stacked QMSIW antenna provides two resonances instead of only one resonance provided by a conventional QMSIW antenna. Specifically, the first and second resonances are centered at 2.4 and 2.6 GHz, respectively. If the two resonances can be tuned to be sufficiently close to one another, a wide bandwidth can be formed.

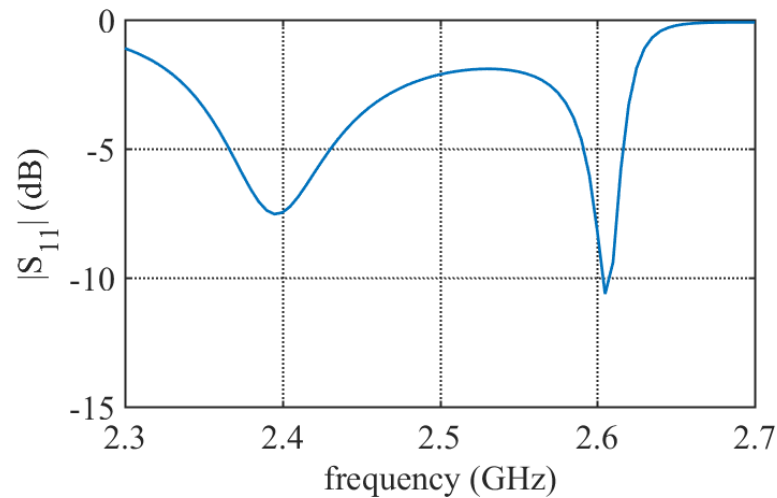
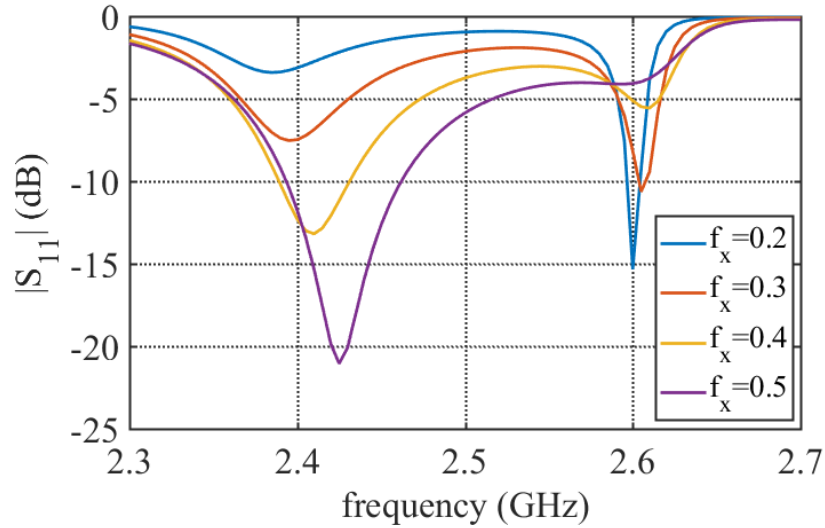


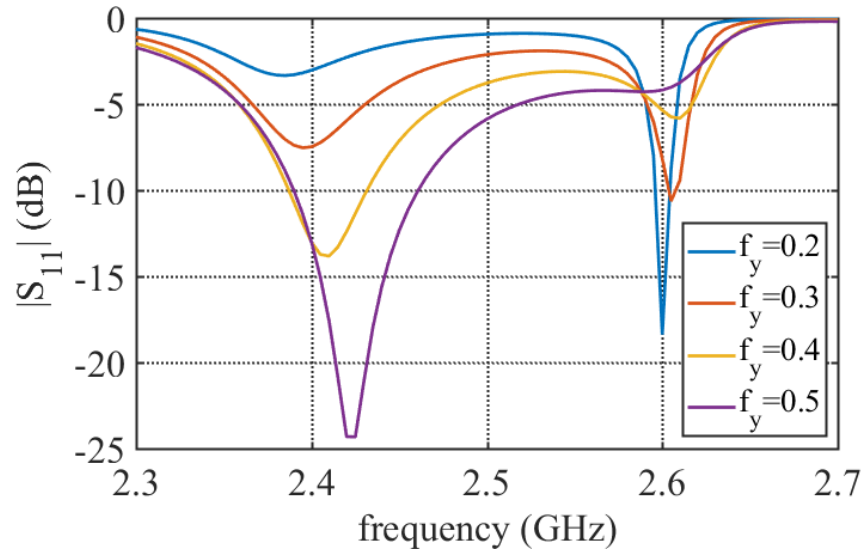
Figure 5-5. Simulated S_{11} of the preliminary stacked QMSIW antenna design with $L_S = W_S = 36$, $L_Q = W_Q = 26$, $L_Q^s = W_Q^s = 26$, $r_1 = 0.5$, $r_2 = 1.0$, $w_f = 2.6$, $h = 6.3$, $m_x = m_y = 0$, $f_x = f_y = 0.3$, all in millimeter.

To this end, a series parametric studies on corresponding design parameters are carried out to explore the possibility of merging the two resonances together.

The first parametric study is of parameters f_x and f_y . The corresponding simulated results are shown in Figure 5-6(a) and Figure 5-6(b), respectively. It should be mentioned that all the other dimensions are kept the same as the preliminary design. The results clearly demonstrate that the effects of changing f_x and f_y are the same. Specifically, the two resonances are kept at 2.4 and 2.6 GHz. In other words, the coupling between the original and the stacked QMSIW antennas are the same with different values of f_x or f_y . In addition, a smaller f_x or f_y results in a better impedance matching for the second resonance and a worse one for the first resonance, and vice versa.



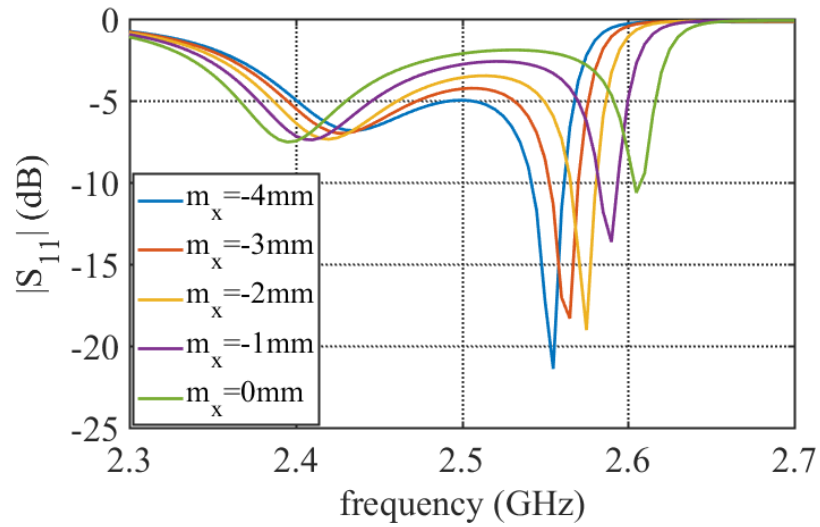
(a)



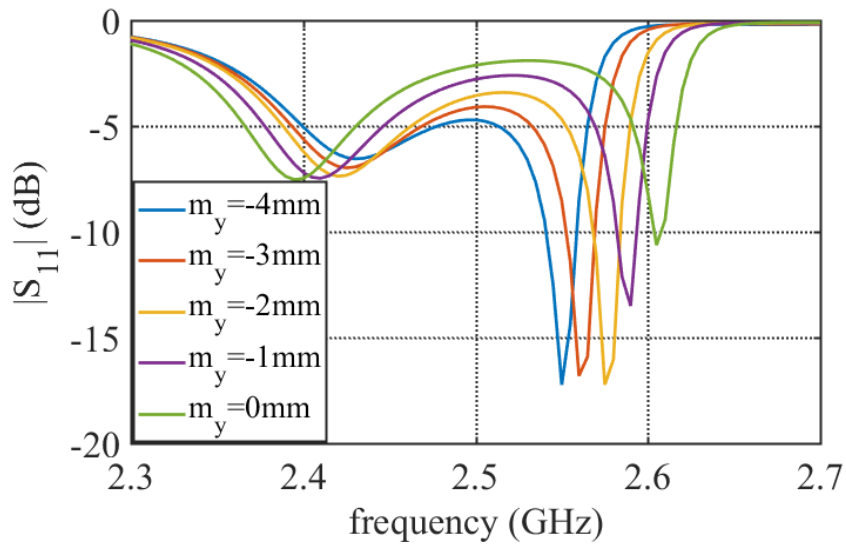
(b)

Figure 5-6. Parametric studies on (a) f_x and (b) f_y .

The second parametric study focuses on parameters m_x and m_y . The corresponding simulated results are shown in Figure 5-7(a) and Figure 5-7(b). The results show that the effects of changing m_x and m_y are almost the same. Specifically, by increasing the value of m_x or m_y , the two resonances get closer to each other. In other words, the coupling between the original and the additional QMSIW antennas become smaller. Consequently, m_x and m_y can be adjusted to tune the coupling strength. Another effect of tuning m_x and m_y is on the impedance matching of the two resonances. As demonstrated, a smaller m_x or m_y causes a better impedance matching for the first band and a worse one for the second band.



(a)

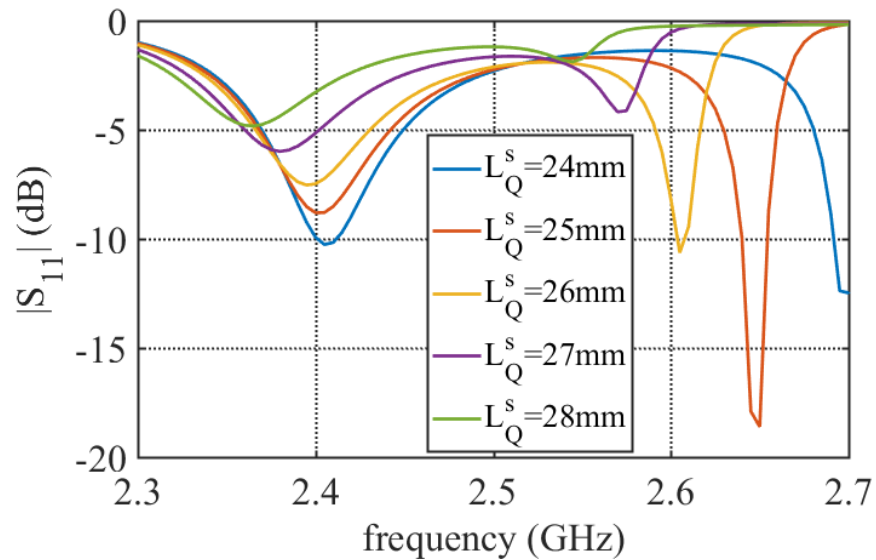


(b)

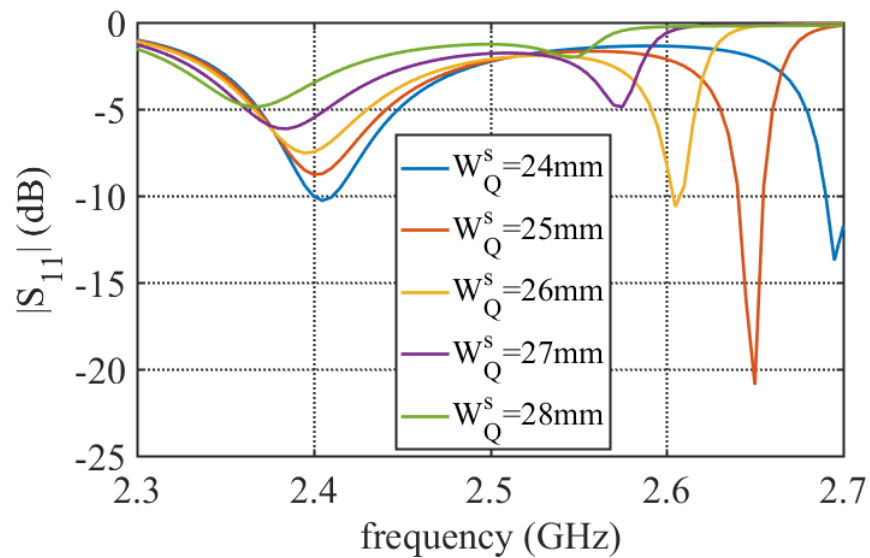
Figure 5-7. Parametric studies on (a) m_x and (b) m_y .

The third parametric study focuses on the size of the stacked antenna. To avoid the change of coupling between the stacked and original antenna, the length and the width of the stacked antenna are assigned as $L_Q^s = L_Q - m_x$ and $W_Q^s = W_Q - m_y$. In this way, adjusting L_Q^s and W_Q^s are equivalent to changing m_x and m_y . The corresponding results for stacked antenna with different

length and width are shown in Figure 5-8(a) and Figure 5-8(b). As shown, the effects of changing L_Q^s and W_Q^s are almost the same. Basically, the increase of either parameter causes the second band to shift toward lower frequency range, while the first band remains almost unaffected. However, with larger values of L_Q^s and W_Q^s , impedance matchings for both bands are degraded.



(a)



(b)

Figure 5-8. Parametric studies on (a) L_Q^S and (b) W_Q^S .

Based on the parametric studies discussed above, the stacked QMSIW antenna is optimized and the finalized design parameters are summarized in Table 5-1. The overall size of the antenna is thus $36.9 \text{ mm} \times 36.9 \text{ mm} \times 7.3 \text{ mm}$, which is equivalent to an electrical dimension of $0.3\lambda_0 \times 0.3\lambda_0 \times 0.06\lambda_0$, where λ_0 is the wavelength at 2.44 GHz in free space.

Table 5-1. Finalized Design Parameters for the Stacked QMSIW Antenna (all in mm).

L_S	W_S	L_Q	W_Q	L_Q^S	W_Q^S	f_x	f_y	m_x	m_y	w_f	r_1	h	r_2
36.9	36.9	25.9	25.9	25.9	24.9	0.3	0.4	-2	-1	2.6	0.5	6.3	1.0

The simulated S_{11} and gain performance of the proposed stacked QMSIW antenna is shown in Figure 5-9. As shown, the $S_{11} < -10 \text{ dB}$ bandwidth is 140 MHz ranging from 2.36 to 2.50 GHz, centered at 2.43 GHz. This bandwidth is equivalent to a fractional bandwidth of 5.8%, despite the small antenna volume. It should be mentioned that the $S_{11} < -10 \text{ dB}$ band fully cover the industrial, scientific, and medical (ISM) band. The gain within the $S_{11} < -10 \text{ dB}$ band varies from 4.3 to 5.0 dBi. Moreover, there is a gain null located at 2.6 GHz, resulting in a steep higher band edge of the gain profile and thus an improved frequency selectivity. In other words, the stacked QMSIW antenna also possesses a filtering characteristic.

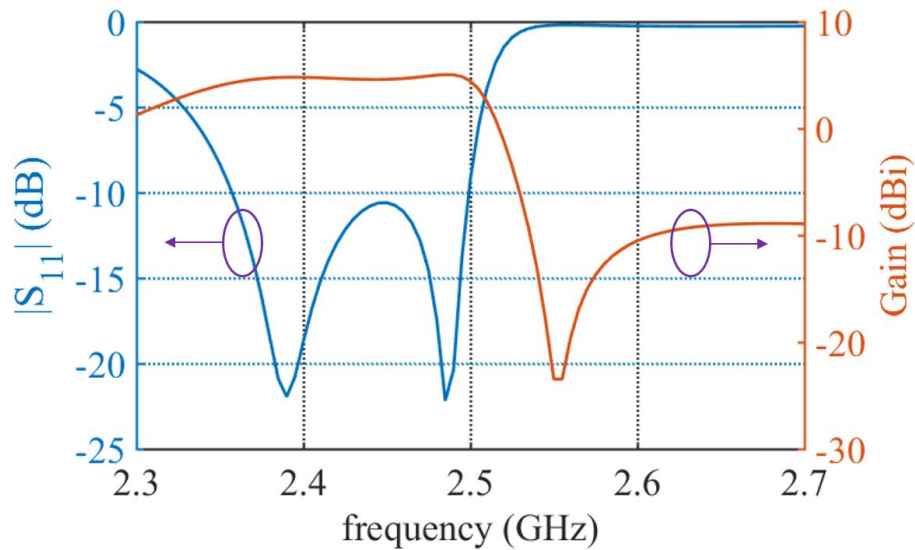


Figure 5-9. Simulated S_{11} and gain of the proposed stacked QMSIW antenna.

In order to illustrate the bandwidth enhancement achieved by the stacked QMSIW antenna, a reference single-layered QMSIW antenna is simulated with exact overall and QMSIW cavity size as the proposed QMSIW antenna. The simulated results (not shown here) show that without the stacked structure, the bandwidth is only 70 MHz ranging from 2.41 to 2.48 GHz, which is only half of the bandwidth of the proposed antenna. In summary, the proposed stacked QMSIW antenna successfully improves the bandwidth and the frequency selectivity at the same time.

The simulated normalized radiation patterns of the proposed stacked QMSIW antenna at 2.44 GHz on both the E -plane and H -plane are plotted in Figure 5-10(a) and Figure 5-10(b), respectively. The co-polarization is denoted as solid curves, while the cross-polarization is represented by the dashed curves.

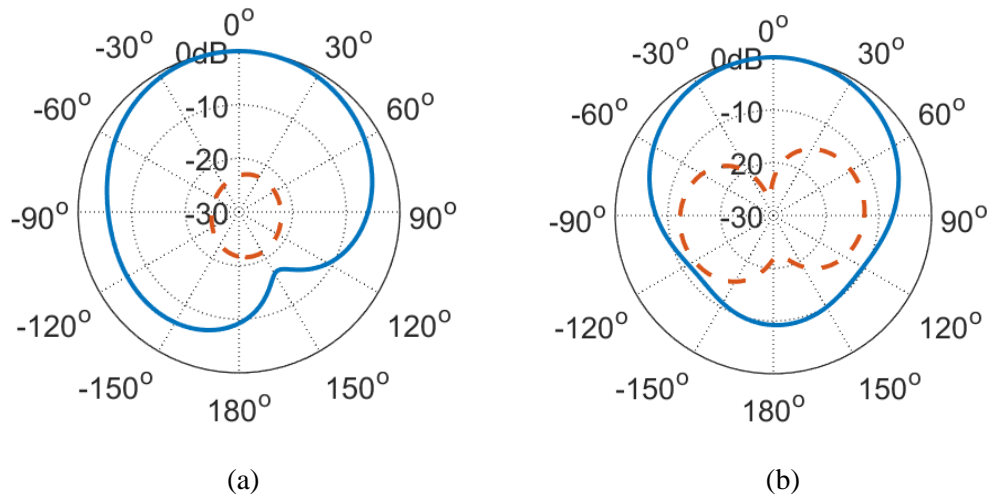


Figure 5-10. Simulated normalized radiation patterns on the (a) *E*-plane and (b) *H*-plane at 2.44 GHz.

5.3 Wearable Stacked QMSIW Antenna

In this section, the effects of antenna deformation and human body loading, both of which are commonly observed when antennas are integrated in wearable systems, are investigated.

5.3.1 Antenna Deformations

Figure 5-11 shows the scenario when the stacked QMSIW antenna is bent by an angle denoted as θ_b .

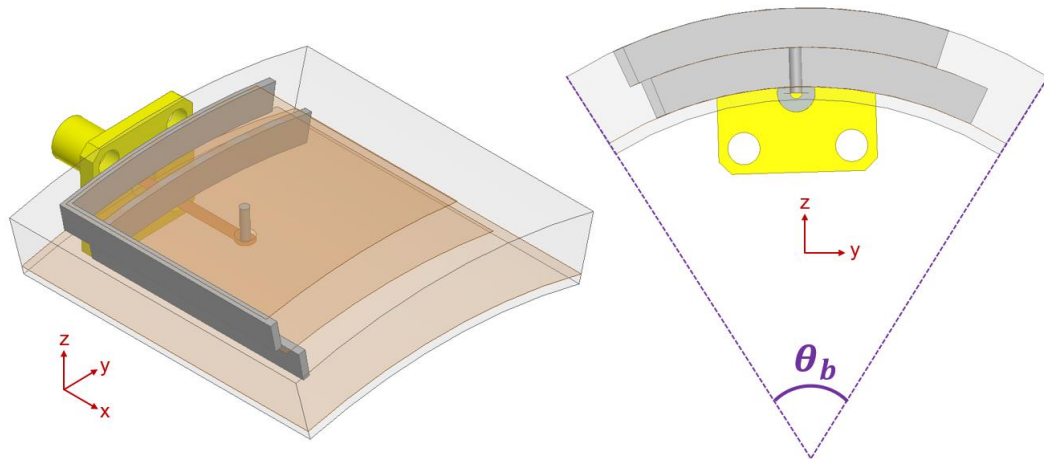


Figure 5-11. Bent stacked QMSIW antenna.

To investigate the effects of different bent angles, a parametric study on the value of θ_b is carried out, and the simulated S_{11} is shown in Figure 5-12. As shown, when θ_b is equal to 10° , 20° , 30° , and 40° , the corresponding $S_{11} < -10$ dB bandwidths of the antenna are 130 MHz (from 2.38 to 2.51 GHz), 130 MHz (from 2.39 to 2.52 GHz), 130 MHz (from 2.40 to 2.53 GHz), and 110 MHz (from 2.42 to 2.53 GHz), respectively. In addition, it is clear that the increase of θ_b cause the operational bands of the stacked QMSIW antenna to slightly shift to higher frequency range. However, wide bandwidths are still achieved, and are much larger than the bandwidth of a conventional QMSIW antenna.

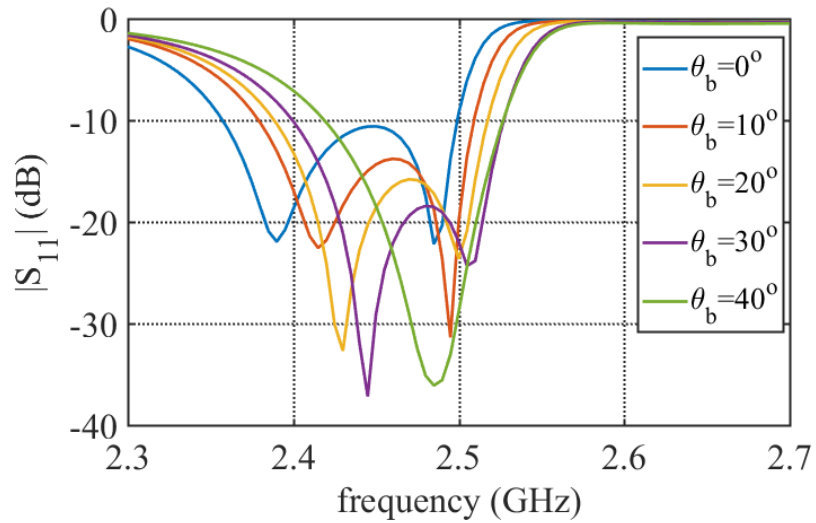


Figure 5-12. Simulated banding effect on the S_{11} of the proposed stacked QMSIW antenna.

The simulated gain performances are shown in Figure 5-13. As shown, when θ_b is 10° , 20° , 30° , and 40° , the gains are well maintained around 5 dBi within corresponding $S_{11} < -10$ dB operational band. Obviously, the increase of θ_b does not cause the any degradation of antenna gain performance.

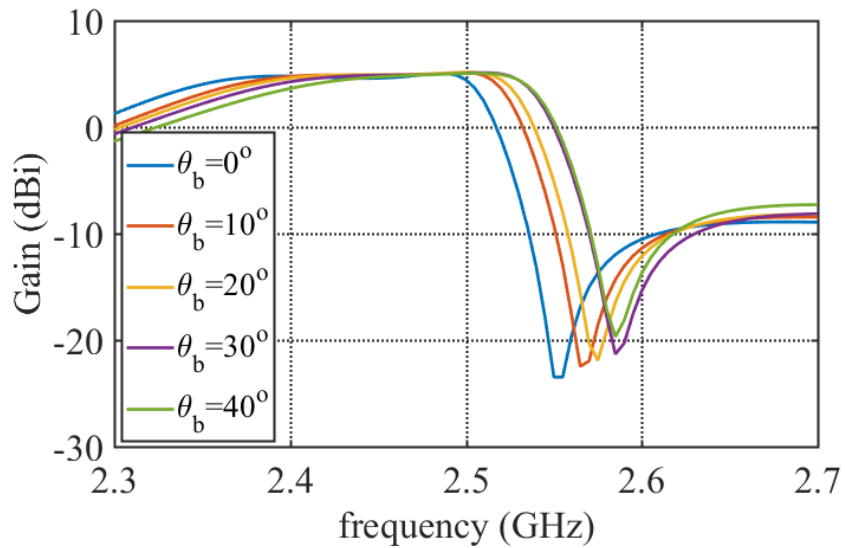


Figure 5-13. Simulated banding effect on the gain of the proposed stacked QMSIW antenna.

The simulated normalized radiation patterns at 2.44 GHz when the proposed antenna is bent are shown in Figure 5-14(a) and (b) on the E -plane and H -plane, respectively. As shown, when θ_b is equal to 10° , 20° , 30° , and 40° , the co-polarization patterns on both the E -plane and H -plane remain almost the same as those when the antenna is not bent. Although slight increases of cross-polarization are observed, the cross-polarization levels are still well suppressed and are at least 17 dB below the co-polarization level along the broadside.

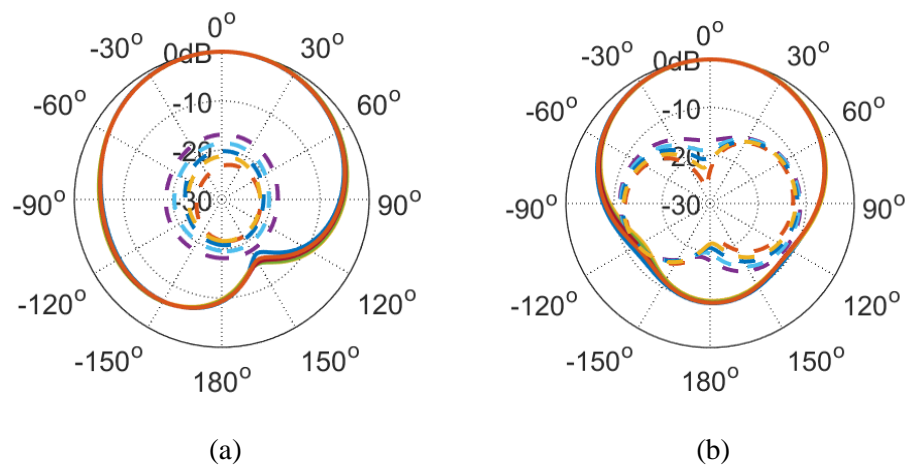


Figure 5-14. Simulated bending effect on the normalized radiation patterns of the proposed stacked QMSIW antenna on the (a) E -plane and (b) H -plane.

5.3.2 Human Body Loading Effect

In order to investigate the human body loading effects on the stacked QMSIW antenna's performances, the corresponding human body models are built up, as shown in Figure 5-15 and Figure 5-18, to model human chest and arm. The electromagnetic properties and dimensions of skin, fat, muscle, and bone are summarized in Table 5-2. It should be noted that the thicknesses characterize the human chest model and the radius describe the human arm model. Figure 5-15 shows the scenario when the stacked QMSIW antenna is placed on a truncated human chest model.

Table 5-2. Electromagnetic Properties and Dimensions of Skin, Fat, Muscle, and Bone of Human Body Models.

	Skin	Fat	Muscle	Bone
Dielectric Constant	37.952	5.2749	52.668	18.49
Conductivity (S/m)	1.487	0.1067	1.773	0.8229
Thickness (mm)	2	5	20	-
Radius (mm)	40	38	33	13

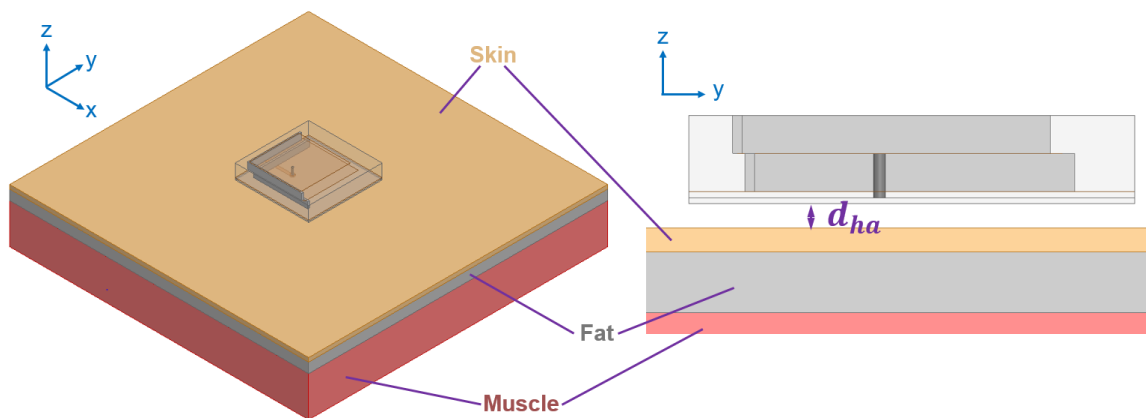


Figure 5-15. Simulation setup for modeling antenna being placed on human chest.

The simulated S_{11} and gain of the stacked QMSIW antenna when it is placed on human chest is shown in Figure 5-16 with different values of d_{ha} . The simulated performances of the QMSIW antenna in free space is also included as references. The results show that the $S_{11} < -10$ dB impedance matching bands slightly shift toward higher frequency regions. In addition, the bandwidth is slightly decreased as the antenna is approaching the human model. In terms of the gain performances, a 1.5 to 2.0 dBi drop is observed within the operational bands when the antenna is loaded by the human body model. Specifically, the gain profile of the antenna for each value of d_{ha} are almost the same varying from 2.0 to 3.0 dBi.

The simulated normalized radiation patterns at 2.44 GHz of the stacked QMSIW antenna when it is placed on human arm model on the E -plane and H -plane are plotted in Figure 5-17(a)

and Figure 5-17(b), respectively. The antenna radiation patterns in free space are also included for references. As shown, the unidirectional radiations along the broadside of the antenna are well maintained. In addition, the cross-polarization level is decreased on the E -plane when the antenna is loaded by human body model. However, on the H -plane, the cross-polarization level is increased.

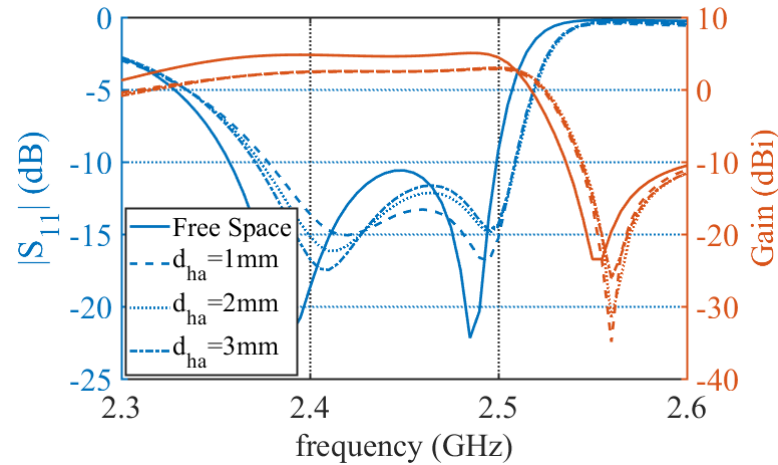


Figure 5-16. Simulated antenna performances when the antenna is placed human chest model.

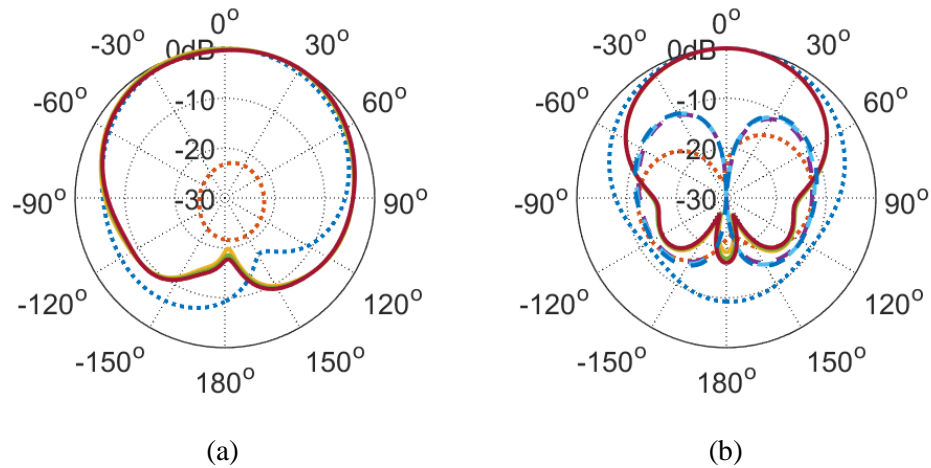


Figure 5-17. Simulated normalized radiation patterns at 2.44 GHz on the (a) E -plane and (b) H -plane when the antenna is placed human chest model (dot line: antenna in free space; solid line: co-polarization; dashed line: cross-polarization).

Figure 5-18 shows the scenario when the stacked QMSIW antenna is placed on a truncated human arm model. To make the antenna conform to the human arm, the antenna is bent with an angle of 30° .

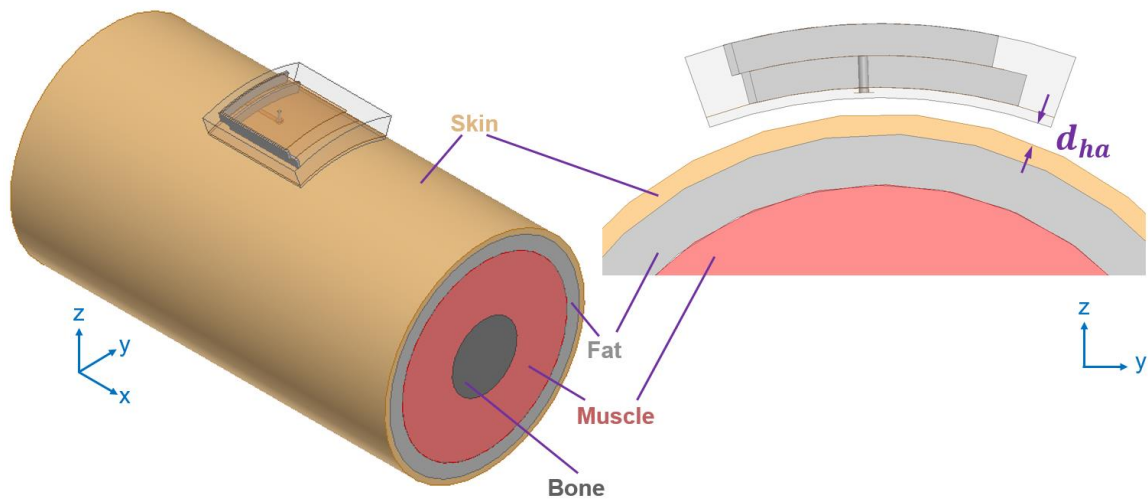


Figure 5-18. Simulation of the stacked QMSIW antenna placed on human arm.

The simulated S_{11} and gain of the antenna with varying distance d_{ha} between the proposed antenna and human arm model are shown in Figure 5-19. The simulated performances of the QMSIW antenna in free space, but bent with an angle equal to 30° , is also shown for reference. The results show that the $S_{11} < -10$ dB impedance matching bands remain almost the same as that of the free space case, but the bandwidths slightly decrease. In terms of the gain performances, a 1.5 to 1.8 dBi drop is observed within the operational bands when the antenna is loaded by the human body model. Specifically, the gain profile of the antenna for each value of d_{ha} are almost the same, varying from 2.2 to 3.5 dBi.

The simulated normalized radiation patterns at 2.44 GHz of the stacked QMSIW antenna on E -plane and H -plane when it is placed on the human chest model are plotted in Figure 5-20(a) and Figure 5-20(b), respectively. The radiation patterns in free space with the antenna bent by 30° are also included for reference. As shown, the unidirectional radiations of the antenna are well

maintained. In addition, the co- and cross-polarization patterns for the antenna loaded by human arm are almost the same as those for the antenna in free space.

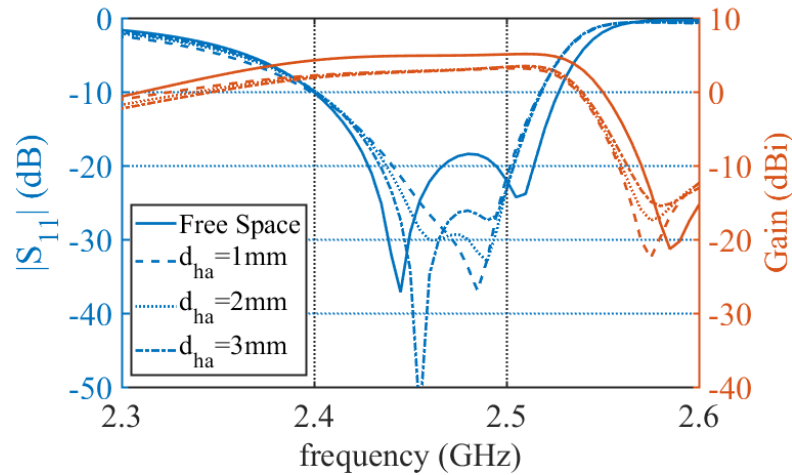


Figure 5-19. Simulated antenna performances when the antenna is placed human arm model.

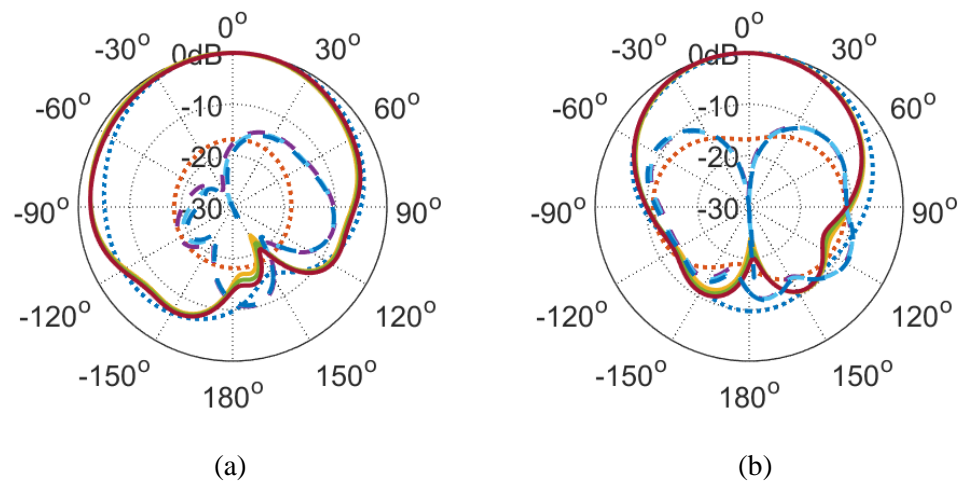


Figure 5-20. Simulated normalized radiation patterns at 2.44 GHz on the (a) *E*-plane and (b) *H*-plane when the antenna is placed human arm model (dot line: antenna in free space; solid line: co-polarization; dashed line: cross-polarization).

5.4 Conclusion

In this chapter, the design of a novel compact stacked QMSIW wearable antenna based on flexible material system was introduced. The footprint of the proposed antenna is only $0.3\lambda_0 \times 0.3\lambda_0$, where λ_0 is the wavelength at 2.44 GHz in free space. The dielectric layers of the proposed antenna is a flexible material SEBS. The vertical electroplated via holes of conventional QMSIW antenna are replaced by liquid metal walls based on the EGaIn material. To the author's best knowledge, this is the first time that liquid metal has been applied in SIW-based antenna design. The stacked QMSIW configuration is proven not only to provide a wide fractional bandwidth of 6%, but also to achieve filtering characteristic by introducing a gain null at the higher frequency edge. To test its flexibility, the effects of bending the antenna are investigated. The results show that the wideband performances of the antenna are maintained and for a bending angle smaller than 30° , the targeted ISM band can be fully covered. To explore the human body loading effect, the antenna was placed on human chest and arm models. The results illustrate that in both situations the ISM band are fully covered. The wideband as well as the filtering characteristic are well maintained. However, the gains experience around 1.5 to 2.0 dBi drop for both cases. This is commonly seen in wearable antennas. The unidirectional patterns with low cross-polarization patterns are achieved despite the human body loadings. In summary, the proposed compact wideband stacked QMSIW antenna is a promising candidate in wearable applications.

Chapter 6

Reconfigurable Directional Surface Plasma (SP) Wave Generators

6.1 Introduction

Traditional approaches for the generation of SP waves utilize bulky prisms [131, 132] or gratings to couple light propagating in free space into surface waves (SWs) guided along the interface defined between an insulator and a metal. However, due to the fact that prisms are large the applicability of this coupling mechanism is rather limited. Recently, several SP wave generators with compact size have been proposed [133, 134]. For example, in [133], the proposed SP generator consists of a single Si NW placed on a gold substrate. When the Si NW is illuminated with a normally incident plane wave (impinging from air), it couples the incident wave into SP waves along the interface defined between the air and the gold substrate. The advantages that this coupling technique offers are the following: (a) the NW is of deep sub-wavelength size, and (b) the coupling efficiency of the Si NW SP wave generator is higher than that of previously reported SP wave generators.

Because of the inherent geometrical symmetry that the aforementioned SP wave couplers exhibit, they can only support the generation of bi-directional SP waves; this feature is not advantageous for the realization of modern advanced functional photonic devices. Consequently, the ability to generate unidirectional SP waves is a highly desirable feature and a considerable research effort has been put towards its realization. Several approaches have been reported so far that successfully realize the generation of unidirectional SP waves. For example, in [135- 139], the unidirectional generation of SP waves was realized by illuminating the SP wave generators with plane waves incident at an oblique angle. Another approach is based on designing asymmetrical SP

wave generators. For example, the involvement of reflectors on one side of the SP generators [140-143] can achieve SP waves propagating only on the other side. In addition, modifications are made to symmetrical SP wave generators to make them asymmetrical [144-149]. For example, the traditional symmetrical nanoslit, NG, or grating were redesigned to be asymmetrical to realize unidirectional SP wave generations. The third methods is to design an array of SP wave generators [150, 151].

All of the SP wave generators discussed above, however, can only provide fixed functionality. In the following sections, four SP wave generators with reconfigurable functionalities are proposed based on Si NWs.

6.2 Unidirectional SP wave Generator Based on Nanowires (NWs)

6.2.1 NW Pair

The configuration of a Si NW pair on a gold film is shown in Figure 6-1(a). Figure 6-1(b) shows the side view of the proposed two-element NW array. The diameters d_1 and d_2 of the two NWs are both equal to 170 nm. Because the NWs are much longer than the wavelength in free space, they are considered to be infinitely long. The distance between the two NWs is denoted as d . A plane wave is obliquely incident upon the structure, with its wave vector lying in the yo -plane, forming an angle of θ with respect to the z -axis. Simulation of a single Si NW on the gold film reveals that an optimal launch of SP waves occurs at 350 THz, therefore this is set as the operating frequency for this study. This frequency is also close to the resonant frequency of the TE_{00} mode of a single Si NW illuminated by a TE^x polarized plane wave in free space.

Before discussing the working principle of the proposed SP wave generator, it should be noted that the near-field coupling between the two Si NWs is disregarded, and the excitation of SP

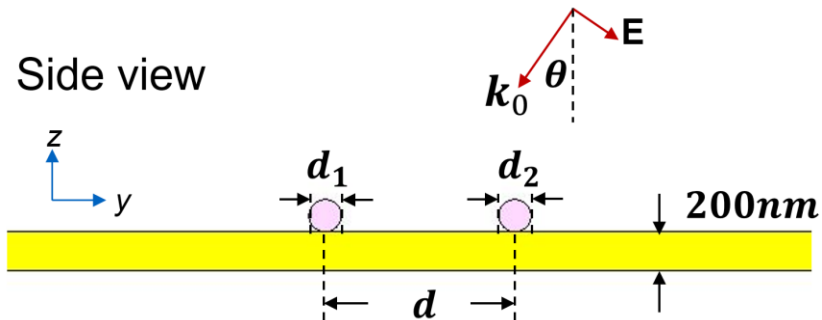
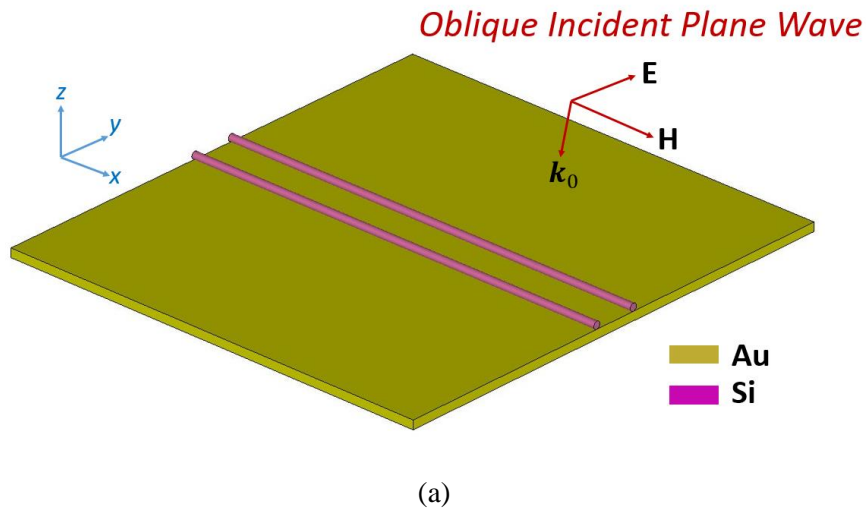
waves from the two Si NWs is therefore considered to be independent. Consequently, the E -fields of the SP wave propagating along $-y$ and $+y$ directions is expressed as:

$$\mathbf{E}_{-y}(y, z, t) = \sqrt{\frac{1}{2}} \mathbf{E}_{sp}(y, z, t) [1 + e^{j(\beta_{sp}d + \phi)}] \quad (6-1)$$

$$\mathbf{E}_{+y}(y, z, t) = \sqrt{\frac{1}{2}} \mathbf{E}_{sp}(y, z, t) [1 + e^{j(-\beta_{sp}d + \phi)}] \quad (6-2)$$

where $\beta_{sp} = k_{sp} - j\gamma$ is the complex propagation constant of the SP wave; k_{sp} and γ are respectively the corresponding wavenumber and the attenuation constant. $\mathbf{E}_{sp}(y, z, t)$ is the E -field of the SP wave generated by a single Si NW. The parameter ϕ represents the phase difference of the SP waves generated by the two Si NWs and is expressed as:

$$\phi = -k_0 d \sin\theta \quad (6-3)$$



(b)

Figure 6-1. (a) 3D configuration and (b) side view of a two-element Si NW array on top of a gold film.

Based on Eqs. (6-1) to (6-3), the total field of an SP wave propagating along the y -axis, excited by a normally incident plane wave ($\theta = 0$), is calculated. Corresponding results are shown in Figure 6-2(a). It can be seen that the $-y$ and the $+y$ propagating waves overlap. This indicates that the maximal and minimal generation of SP waves can be achieved simultaneously by adjusting the distance between the two Si NWs. According to the curve in Figure 6-2(a), the first null of the SP wave excitation occurs when $d = 400$ nm, while the maximal excitation of the SP wave happens when $d = 800$ nm. However, when the plane wave is obliquely incident on the two-element NW array, the SP waves propagating along $\pm y$ directions are not identical, as shown in Figure 6-2(b).

Numerical simulations are carried out to validate the analytical predictions discussed above. In order to quantify the unidirectional SP wave generation the extinction ratio (ER) is defined as:

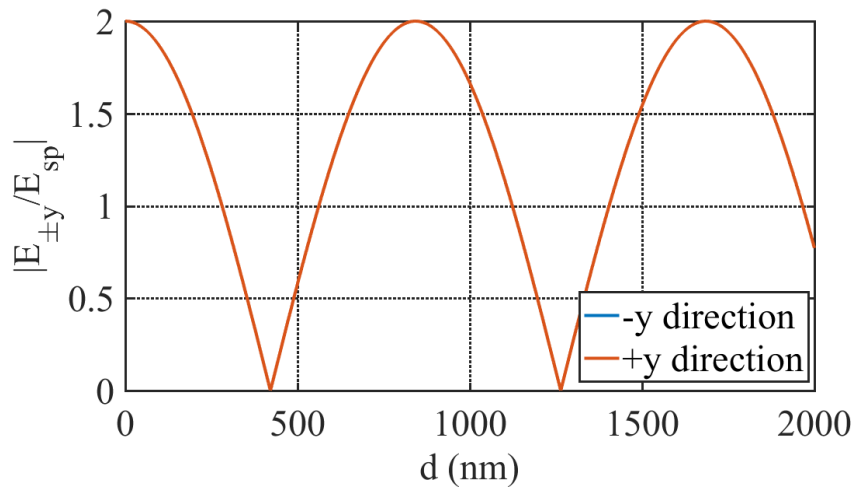
$$\text{ER (dB)} = 20 \times \log_{10} \left(\frac{|E_{z,+y}|}{|E_{z,-y}|} \right) \quad (6-4)$$

Intuitively, if $\text{ER} > 0$, the majority of the generated SP wave propagates along the $+y$ direction. However, if $\text{ER} < 0$, the majority of the generated SP wave propagates along the $-y$ direction.

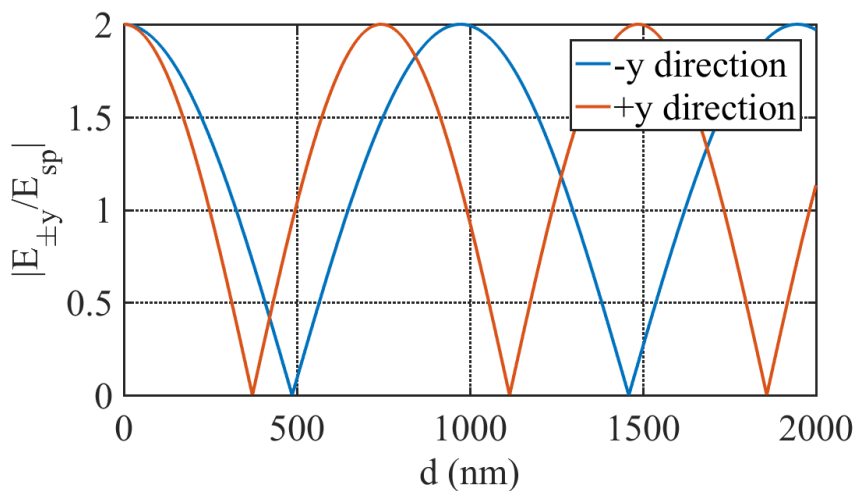
In the simulation, a parametric study on d is carried out where the value of d varies from 300 to 1300 nm. To characterize the intensity of the generated SP waves, two probes are placed 20 μm away from the two-element NW array system to record the magnitudes of the z -component of E -fields. Because the E -field of the SP waves have only a z -component E_z , the power flow of the SP waves is characterized in terms of E_z . The simulated $|E_{z,\pm y}|$ is presented in Figure 6-3(a). As shown, the maximal values of $|E_{z,+y}|$ and $|E_{z,-y}|$ occur when $d = 400$ nm and $d = 600$ nm. However, the analytically predicted the maximal values of $|E_{z,+y}|$ and $|E_{z,-y}|$ occur when $d =$

750 nm and $d = 1000$ nm. The discrepancies between the analytical and simulated results is attributable to the phase shift when the SP waves are propagating through the Si NWs.

The simulated ER is presented in Figure 6-3(b). As shown, when $d = 300$ nm, $d = 800$ nm, and $d = 980$ nm, the excitation of the SP waves are achieved only along +y direction, only along -y direction, and along both $\pm y$ directions. The corresponding E -field distributions are shown in Figure 6-4(a) to Figure 6-4(c).



(a)



(b)

Figure 6-2. Analytically calculated $\left| \frac{E_{\pm y}}{E_{spp}} \right|$ with plane wave incident angle equal to (a) 0 and (b) $\frac{\pi}{23}$.

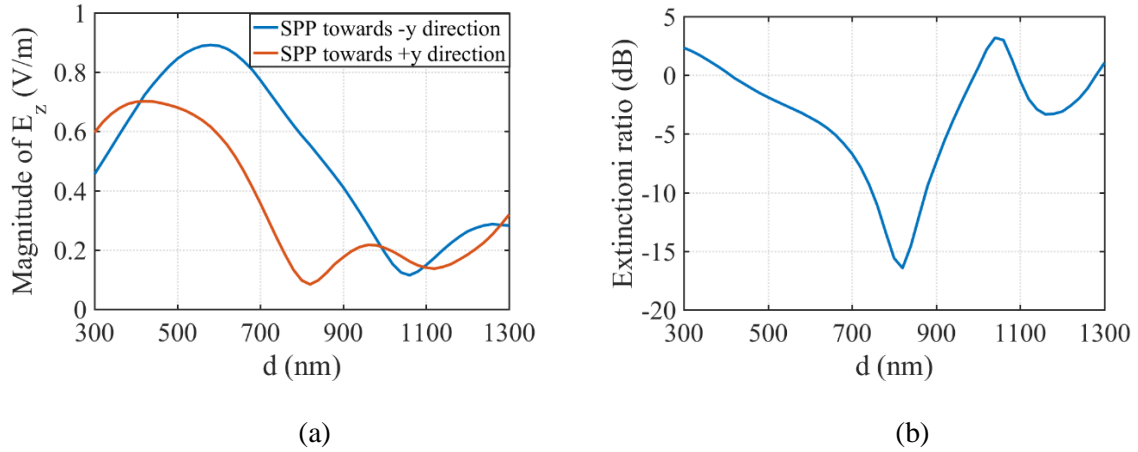


Figure 6-3. Simulated (a) $|E_{z,\pm y}|$ (V/m) and (b) ER (dB) with varying d .

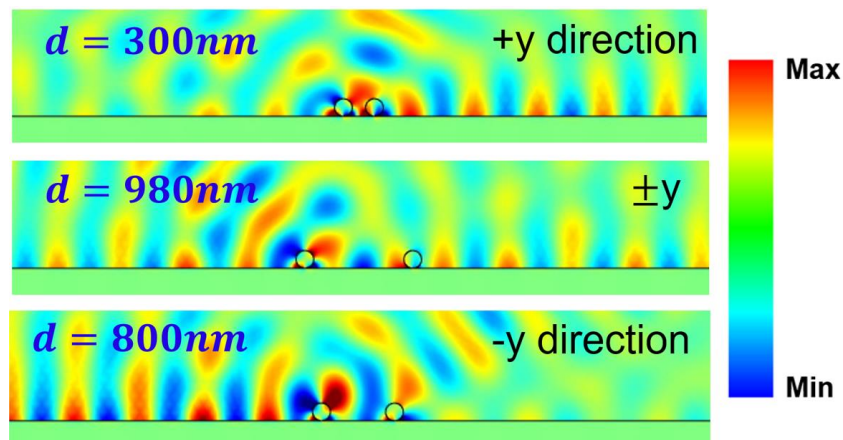


Figure 6-4. Snapshots of the E_z when the SP wave generator is illuminated by an obliquely incident plane wave with $d = 300$ nm, $d = 980$ nm, and $d = 800$ nm.

While the Si NW pair discussed above achieves reconfigurable directional SP wave generations with an obliquely incident plane wave, the following SP wave generator design can realize reconfigurable directional SP wave generations with a normally incident plane wave.

For a Si NW in free space illuminated by a plane wave, where its propagation direction and E -field vector are perpendicular to the Si NW axis, the resonant modes of the Si NW can be described by

$$\frac{J_m^t\left(\frac{nk_0d}{2}\right)}{J_m\left(\frac{nk_0d}{2}\right)} = n \frac{H_m^t\left(\frac{k_0d}{2}\right)}{H_m\left(\frac{k_0d}{2}\right)} \quad (6-5)$$

If Eq. (6-5) is numerically solved it can be shown that the diameter d of a Si NW in its fundamental resonant mode at 350 THz is 85 nm. It is also found that a Si NW with a smaller diameter can have similar resonance strength to that of a Si NW with a larger diameter. However, the phase of the resonance of the two NWs can be different. As mentioned in [131], the generation of SP waves by the Si NW is highly correlated with the self-resonances of the NW. Two Si NWs with different radii generates SP waves with similar strength, but with different phases. When they are placed on the gold sheet at a carefully chosen separation distance, it is possible to excite unidirectional SP waves.

To validate the proposed SP wave generator, corresponding numerical simulation is carried out, as shown in Figure 6-5(a). It can be seen that a normally incident wave at 350 THz impinges upon two Si NWs. Figure 6-5(b) illustrates the detailed dimensions of the proposed SP wave generator. The diameters of the first and second NW are 150 nm and 190 nm, respectively. The distance between the two NWs is denoted as d .

A parametric study was carried out with respect to d , and the simulated $|E_{z,\pm y}|$ and ER are presented in Figure 6-6(a) and Figure 6-6(b), respectively. As shown, when the distance between the two NWs is 310 nm, the unidirectional SP wave generation is observed with the majority of the generated SP wave propagating along the $-y$ direction. In this case, ER equals to -11 dB. When d increases, the intensity of the SP wave propagating toward the $-y$ direction decreases while that of the SP wave propagating toward $+y$ direction increases. When $d = 460$ nm, bi-directional SP wave generation is observed with SP waves propagating equally along the $+y$ and $-y$ directions. In this

case, ER equals to 0. When the distance increases to 630 nm, the majority of the generated SP wave propagates toward the $+y$ direction (ER = 7 dB), and the unidirectional generation of SP wave appears again. Figure 6-7(a) to Figure 6-7(c) show three snapshots of the E_z with distance d equal to 310 nm, 460 nm, and 630 nm, respectively. These figures further illustrates the directional generations of the SP waves from a normally incident plane wave by the proposed SP wave generator. More importantly, the direction of the SP wave propagation is reconfigurable by adjusting the distance between the two Si NWs.

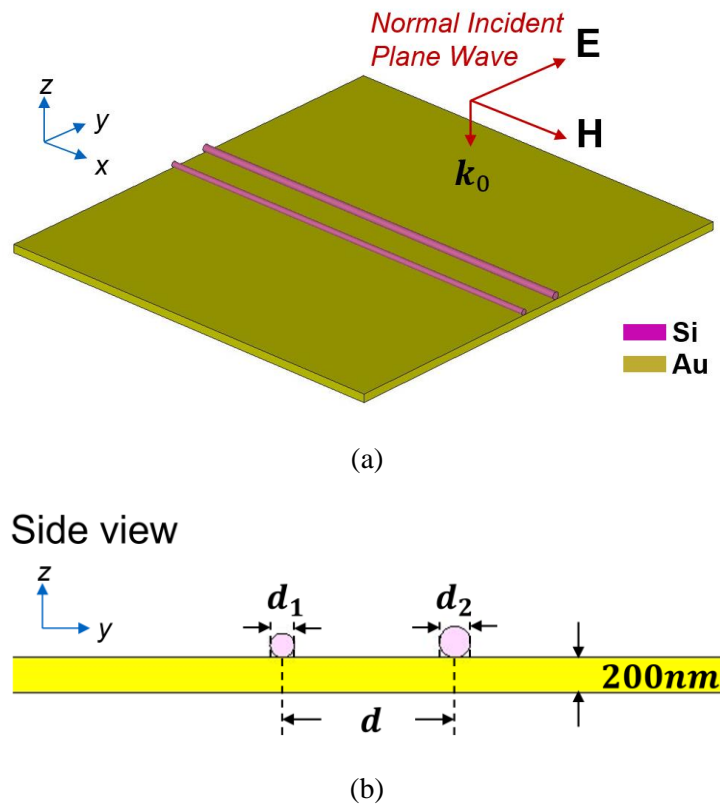


Figure 6-5. (a) 3D configuration and (b) 2D side view of the simulation setup.

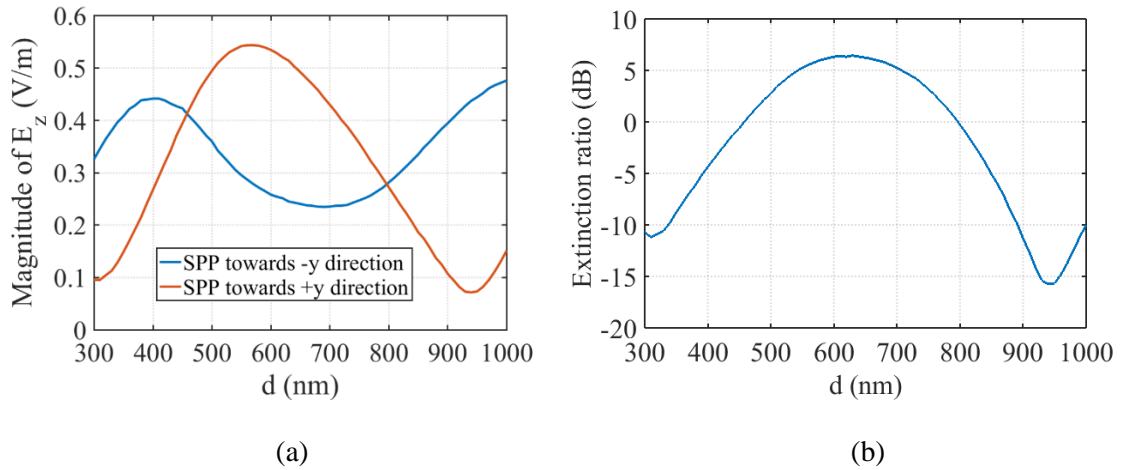


Figure 6-6. Simulated (a) $|E_{z,\pm y}|$ and (b) ER (dB) with varying NW-separation d .

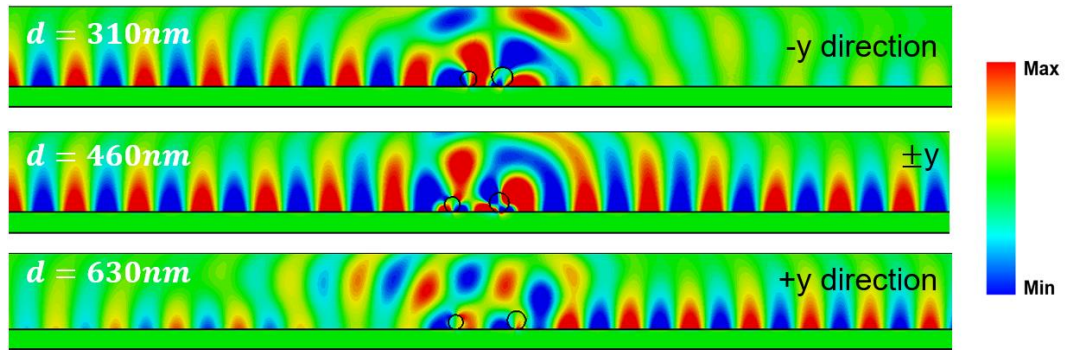


Figure 6-7. Snapshots of the E_z when the proposed SP generator is illuminated by a normally incident plane wave with $d = 310\text{ nm}$, $d = 460\text{ nm}$, and $d = 630\text{ nm}$.

6.2.2 NW in Nanogroove (NG)

In this section, another SP wave generator design is presented to achieve directional coupling of SP waves from normally incident plane waves. The 3D configuration of the proposed SP wave generator is shown in Figure 6-8(a). A normally incident plane wave at 350 THz with its E -field polarized along the y -axis and its H -field along the x -axis is utilized for optical excitation. The proposed SP wave generator consists of a Si NW placed in a NG etched on the surface of an

Au sheet with a thickness of 500 nm. Figure 6-8(b) shows the detailed dimensions of the NW and NG. The parameter d represents the distance from the Si NW to the left edge of the NG. As is later shown, the reconfigurability is achieved by tuning the position of the NW inside the NG along the y direction.

A parametric study is carried out in terms of d from 0 to 515 nm, and the simulated $|E_{z,\pm y}|$ and ER are presented in Figure 6-9(a) and Figure 6-9(b), respectively. When $d = 0$, the majority of the generated SP wave propagates along the $-y$ direction with ER = -16 dB. When $d = 220$ nm, the SP waves generated by this structure propagate equally along the $\pm y$ directions with ER = 0. When $d = 140$ nm. The majority of the generated SP wave propagates along the $-y$ direction with ER = 13 dB.

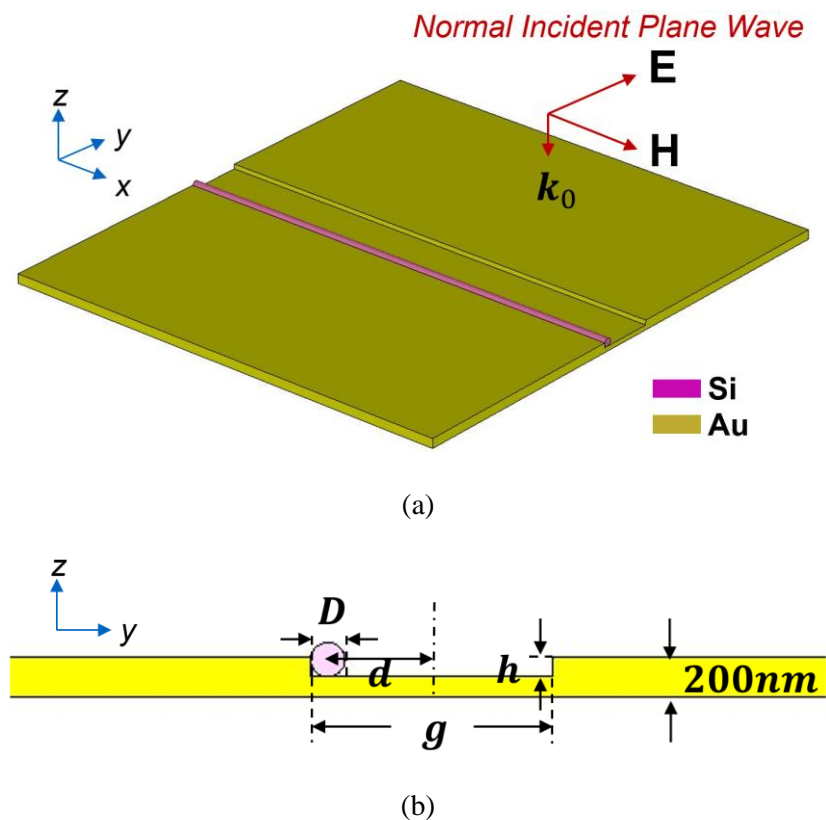


Figure 6-8. (a) 3D configuration and (b) 2D side view of the simulation setup.

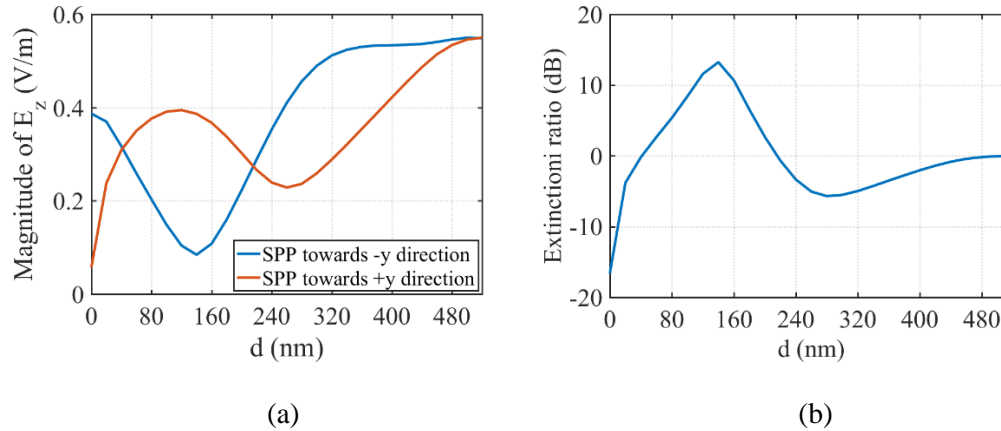


Figure 6-9. Simulated (a) $|E_{z,\pm y}|$ and (b) ER (dB) with varying NW-separation d .

Figure 6-10 shows the snapshots of the simulated E_z with distance d equal to 0, 220 nm, and 140 nm. Figure 6-10 further illustrates the directional generation of SP waves from a normally incident plane wave by the proposed SP wave generator.

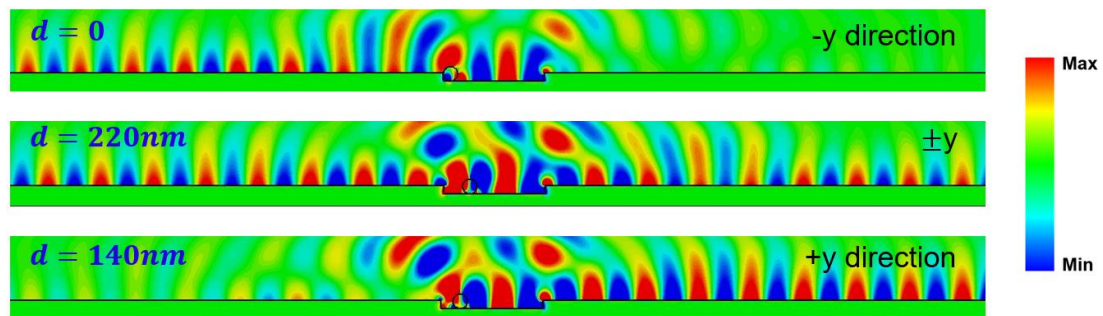


Figure 6-10. Snapshots of the E_z when the proposed SP wave generator is illuminated by a normally incident plane wave with $d = 0$, $d = 220$ nm, and $d = 140$ nm.

6.3 Reconfigurable SP Wave Generator Based on VO₂ Material

6.3.1 VO₂ Material

Recently, Vanadium (IV) dioxide (VO₂) has received increasing research interest because of its unique characteristic: its dielectric properties can be tuned if the material is externally excited,

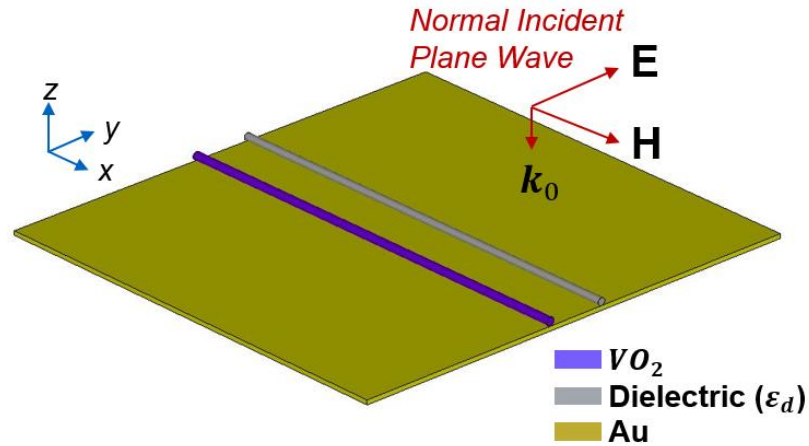
for instance by temperature variations and an optical pumping. Here, the phase transition means the insulator-to-metal transition (IMT) of VO₂. Specifically, the permittivity of VO₂ at 1.5 μm are

$$\begin{cases} \varepsilon_{\text{ins}} = 7.72 + j2.08 \\ \varepsilon_{\text{met}} = -4.22 + j9.39 \end{cases}$$

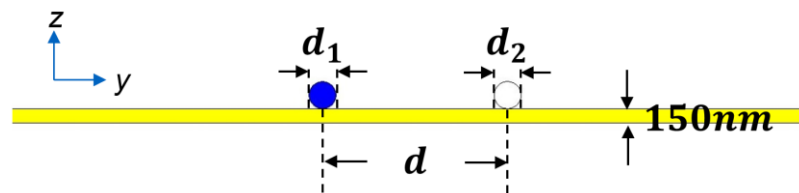
when the VO₂ operates in the insulator and metal phases, respectively.

6.3.2 VO₂ based SP wave generator Design

Based on the IMT provided by the VO₂ material, a reconfigurable SP wave generator at 1.5 μm is proposed in this section. The configuration of the SP wave generator is presented in Figure 6-11. The diameters of the VO₂ NW and a conventional dielectric NW are d_1 and d_2 , respectively. The separation between the two NWs is denoted by d . The dielectric constant of the conventional dielectric NW is ε_d . The thickness of the Au sheet is 150 nm.



(a)



(b)

Figure 6-11. (a) 3D configuration and (b) 2D side view of the proposed reconfigurable SP wave generator.

A 2D parametric study is carried out in terms of d and ϵ_d to explore the reconfigurability of the generator when the VO₂ NW is switched between the insulator phase and metal phase. The simulated ERs are shown in Figure 6-12. As shown, the ER within region **A** enclosed by a dashed ellipse in Figure 6-12(a) is significantly larger than that within the corresponding region **B** in Figure 6-12(b). In other words, the propagation of the generated SP wave toward $-y$ direction is highly suppressed when the VO₂ NW operates in the metal phase. However, when the VO₂ NW is in its insulator phase, the SP wave propagating toward $-y$ direction is recovered.

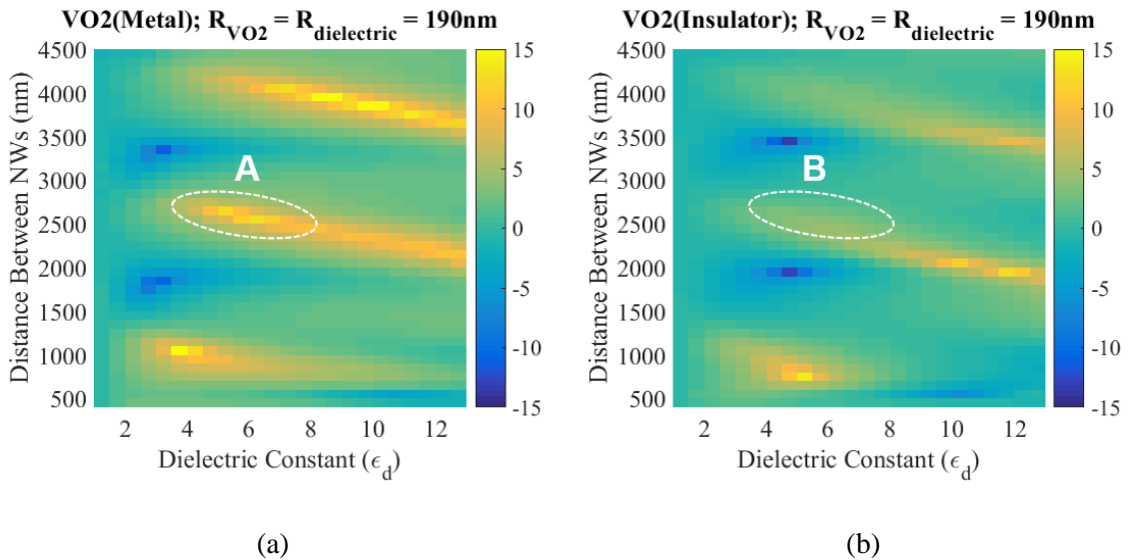


Figure 6-12. Simulated ER (dB) with varying d and ϵ_d when the VO₂ NW is in (a) metal and (b) insulator phase.

For a better illustration of the ERs in regions **A** and **B** in Figure 6-12, the simulated snapshots of the E_z with $(d, \epsilon_d) = (2600 \text{ mm}, 6)$ are plotted in Figure 6-13(a). The result shows that when the VO₂ NW is in the metal phase, the generated SP wave that propagates along the $-y$ direction is almost eliminated. However, when the VO₂ NW is in the insulator phase, as shown in

Figure 6-13(b), the SP wave propagating along $-y$ direction is recovered. Thus, a reconfigurable SP wave generator has been realized.

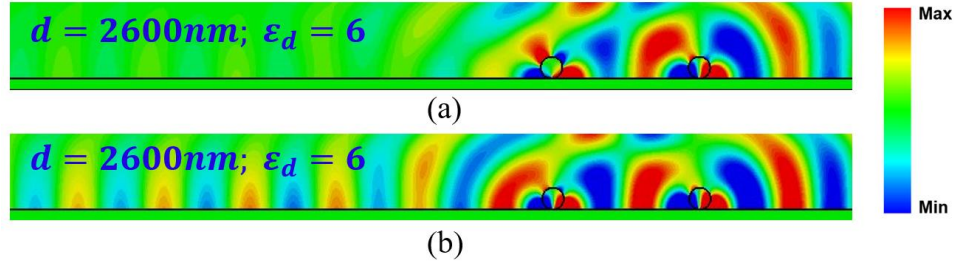


Figure 6-13. Snapshots of the E_z of the generated SP wave that propagates along the $-y$ direction when the SP wave generator is illuminated by a normally incident plane wave with the VO₂ NW in (a) metal and (b) insulator phases.

6.4 Conclusion

In this chapter, four reconfigurable SP wave generators for directional SP wave generation were introduced. Specifically, the first three designs are based on Si NWs and the final design is enabled by VO₂ NWs with an IMT capability. The Si NW-based reconfigurable SP wave generators can achieve the unidirectional or bi-directional SP wave generations when they are illuminated with either oblique (the first design) or normal (the second and third designs) incident plane waves. The reconfigurable generation of SP waves is made possible by varying the separation between a Si NW pair (the first and second designs) or the position of a Si NW within an Au NG (the third design). The fourth design can turn on and off the generated SP wave that propagates along the $-y$ direction, while keeping the SP wave propagating along the $+y$ direction unaffected. This is achieved by switching a VO₂ NW between its insulator and metal phases. In summary, these reconfigurable SP wave generators have numerous applications including integrated photonic circuits.

Chapter 7

Future Work

There are many possible future research directions envisioned based on the work presented in this dissertation.

In the future, antenna array concepts could be studied based on the antenna element designs presented in Chapter 2 and Chapter 3. The dual-band dual-sense CP antenna designs proposed in Chapter 4 will be fabricated and tested to verify the simulated results. In terms of the novel stacked QMSIW antenna proposed in Chapter 5, the fabrication procedure will be explored in collaboration with Prof. Michael Dickey's research group at the North Carolina State University (NCSU). Specifically, the methods of injecting the EGaIn liquid metal into the SEBS polymer layer will be investigated. Once the antenna is fabricated, measurements of the antenna will be carried out. Fabrications of the NW-based SP wave generators proposed in Chapter 6 will also be investigated. The experimental characterization of the generation of SP waves will be explored. Moreover, the working principles of the SP wave will also be studied to explain the theory behind the directional generation of SP waves.

Bibliography

- [1] K. -L. Wong, *Planar Antennas for Wireless Communications*. New York: Wiley, 2003, Ch. 3.
- [2] W. Hong et al., “Multi-beam antenna technologies for 5G wireless communications,” *IEEE Trans. Antennas Propag.*, vol. 65, no. 12, pp. 6231–6249, Dec. 2017.
- [3] K. Wu, Y. J. Cheng, T. Djerafi, and W. Hong, “Substrate-integrated millimeter-wave and terahertz antenna technology,” *Proc. IEEE*, vol. 100, no. 7, pp. 2219–2232, Jul. 2012.
- [4] M. Bozzi, A. Georgiadis, and K. Wu, “Review of substrate-integrated waveguide circuits and antennas,” *IET Microw. Antennas Propag.*, vol. 5, no. 8, pp. 909–920, Jun. 2011.
- [5] R. Garg, P. Bhartia, I. Bahl, and A. Ittipiboon, *Microstrip Antenna Design Handbook*. Norwood, MA: Artech House, 2001.
- [6] R. Moro, S. Agneessens, H. Rogier, A. Dierck, and M. Bozzi, “Textile microwave components in substrate integrated waveguide technology,” *IEEE Trans. Microw. Theory Techn.*, vol. 63, no. 2, pp. 422–432, Feb. 2015.
- [7] J.-J. Greffet, “Nanoantennas for light emission,” *Science*, vol. 308, p. 1561, 2005.
- [8] S. Maier, *Plasmonics: Fundamentals and Applications*. New York: Springer, 2007.
- [9] G. J. Hayes, J. So, A. Qusba, M. D. Dickey, and G. Lazzi, “Flexible liquid metal alloy (EGaIn) microstrip patch antenna,” *IEEE Trans. Antennas Propag.*, vol. 60, no. 5, pp. 2151–2156, May 2012.
- [10] M. Lis et al., “Polymer Dielectrics for 3D-Printed RF Devices in the Ka Band,” *Adv. Mater. Technol.*, vol. 1, no. 2, p. 1600027, May 2016.
- [11] C. A. Balanis, *Antenna Theory: Analysis and Design*, 2nd ed. New York, NY, USA: Wiley, 1997.

- [12] D. Deslandes and K. Wu, "Integrated microstrip and rectangular waveguide in planar form," *IEEE Microw. Wireless Compon. Lett.*, vol. 11, no. 2, pp. 68–70, Feb. 2001.
- [13] D. Deslandes, "Design equations for tapered microstrip-to-substrate integrated waveguide transitions," in *Proc. IEEE MTT-S Int. Microw. Symp.*, May 2010, pp. 1–1.
- [14] D. Deslandes and K. Wu, "Integrated transition of coplanar to rectangular waveguides," in *Proc. Int. Microwave Symp. Dig.*, 2001, vol. 2, pp. 619–622.
- [15] F. Xu and K. Wu, "Guided-wave and leakage characteristics of substrate integrated waveguide," *IEEE Trans. Microw. Theory Tech.*, vol. 53, no. 1, pp. 66–73, Jan. 2005.
- [16] Y. Cassivi, L. Perregrini, P. Arcioni, M. Bressan, K. Wu, and G. Conciauro, "Dispersion characteristics of substrate integrated rectangular waveguide," *IEEE Microw. Wireless Compon. Lett.*, vol. 12, no. 9, pp. 333–335, Sep. 2002.
- [17] D. Deslandes and K. Wu, "Single-substrate integration technique of planar circuits and waveguide filters," *IEEE Trans. Microw. Theory Tech.*, vol. 51, no. 2, pp. 593–596, Feb. 2003.
- [18] Y. Cheng, W. Hong, K. Wu, Z. Kuai, C. Yu, J. Chen, J. Zhou, and H. Tang, "Substrate integrated waveguide (SIW) Rotman lens and its Ka-band multibeam array antenna applications," *IEEE Trans. Antennas Propag.*, vol. 56, no. 8, pp. 2504–2513, Aug. 2008.
- [19] C. Zhong, J. Xu, Z. Yu, and Y. Zhu, "Ka-band substrate integrated waveguide Gunn oscillator," *IEEE Microw. Wireless Compon. Lett.*, vol. 18, pp. 461–463, Jul. 2008.
- [20] M. Abdolhamidi and M. Shahabadi, "X-band substrate integrated waveguide amplifier," *IEEE Microw. Wireless Comp. Lett.*, vol. 18, pp. 815–817, 2008.
- [21] A. D. Rakić, A. B. Djurisić, J. M. Elazar, and M. L. Majewski, "Optical properties of metallic films for vertical-cavity optoelectronic devices," *Appl. Opt.*, vol. 37, no. 22, pp. 5271–5283, Aug. 1998.

- [22] D. Sievenpiper, L. Zhang, R. Jimenez Broas, N. Alexopolous, and E. Yablonivitch, "High-impedance electromagnetic surfaces with a forbidden frequency band," *IEEE Trans. Microw. Theory Tech.*, vol. 47, pp. 2059–2074, Nov. 1999.
- [23] W. Q. Cao, B. N. Zhang, A. J. Liu, T. B. Yu, D. S. Guo, and X. F. Pan, "Multi-frequency and dual-mode patch antenna based on electromagnetic band-gap (EBG) structure," *IEEE Trans. Antennas Propagat.*, vol. 60, no. 12, pp. 6007 - 6012, Dec. 2012.
- [24] Z. H. Jiang, D. E. Brocker, P. E. Sieber, and D. H. Werner, "A compact, low-profile metasurface-enabled antenna for wearable medical body area network devices," *IEEE Trans. Antennas Propagat.*, vol. 62, no. 8, pp. 4021–4030, Aug. 2013.
- [25] C. R. Simovski, P. de Maagt, and I. V. Melchakova, "High-impedance surfaces having stable resonance with respect to polarization and incidence angle," *IEEE Trans. Antennas Propagat.*, vol. 53, no. 3, Mar. 2005.
- [26] S. Zhu and R. Langley, "Dual-band wearable textile antenna on an EBG substrate," *IEEE Trans. Antennas Propagat.*, vol. 57, no. 4, pp. 926–935, Apr. 2009.
- [27] S. R. Best and D. L. Hanna, "Design of a broadband dipole in close proximity to an EBG ground plane," *IEEE Antennas Propagat. Mag.*, vol. 50, no. 6, pp. 52–64, Dec. 2008.
- [28] S. H. Martin, I. Martinez, J. P. Turpin, D. H. Werner, E. Lier, and M. G. Bray, "The synthesis of wide- and multi-bandgap electromagnetic surfaces with finite size and nonuniform capacitive loading," *IEEE Trans. Antennas Propagat.*, vol. 62, no. 9, pp. 1962 – 1972, Sept. 2014.
- [29] B. H. Fong, J. S. Colburn, J. J. Ottusch, J. L. Visher, and D. F. Sievenpiper, "Scalar and tensor holographic artificial impedance surfaces," *IEEE Trans. Antennas Propagat.*, vol. 58, no. 10, pp. 3212–3221, Oct. 2010.
- [30] <http://www.ansys.com/Products/Electronics/ANSYS-HFSS>.

- [31] J. Ortiz, J. Baena, V. Losada, F. Medina, R. Marques, and J. Quijano, "Self-complementary metasurface for designing narrow band pass/stop filters," *IEEE Microw. Wireless Compon. Lett.*, vol. 23, no. 6, pp. 291–293, Jun. 2013.
- [32] J. G. Pollock and A. K. Iyer, "Below-cutoff propagation in metamaterial lined circular waveguides," *IEEE Trans. Microw. Theory Tech.*, vol. 61, no. 9, pp. 3169–3178, 2013.
- [33] O. Luukkonen, F. Costa, C. R. Simovski, A. Monorchio, and S. A. Tretyakov, "A thin electromagnetic absorber for wide incidence angles and both polarizations," *IEEE Trans. Antennas Propagat.*, vol. 57, no. 10, pp. 3119–3125, Oct. 2009.
- [34] Z. H. Jiang and D. H. Werner, "Quasi-three-dimensional angle-tolerant electromagnetic illusion using ultrathin metasurface coatings," *Adv. Funct. Mater.*, vol. 24, no. 48, pp. 7728–7736, Dec. 2014.
- [35] Z. H. Jiang, M. D. Gregory, and D. H. Werner, "A broadband monopole antenna enabled by an ultrathin anisotropic metamaterial coating," *IEEE Antennas Wireless Propagat. Lett.*, vol. 10, pp. 1543–1546, 2011.
- [36] D. Germain, D. Seetharamdoo, S. N. Burokur, and A. de Lustrac, "Phase compensated metasurface for a conformal microwave antenna," *Appl. Phys. Lett.*, vol. 103, no. 12, p. 124102, Sep. 2013.
- [37] H. L. Zhu, S. W. Cheung, K. L. Chung, and T. I. Yuk, "Linear-to-circular polarization conversion using metasurface," *IEEE Trans. Antennas Propagat.*, vol. 61, no. 9, pp. 4615–4623, Sep. 2013.
- [38] D. Blanco, E. Rajo-Iglesias, S. Maci, and N. Llombart, "Directivity enhancement and spurious radiation suppression in leaky-wave antennas using inductive grid metasurfaces," *IEEE Trans. Antennas Propagat.*, vol. 63, pp. 891–900, Mar. 2015.

- [39] B. H. Fong, J. S. Colburn, J. J. Ottusch, J. L. Visher, and D. F. Sievenpiper, "Scalar and tensor holographic artificial impedance surfaces," *IEEE Trans. Antennas Propagat.*, vol. 58, no. 10, pp. 3212–3221, Oct. 2010.
- [40] C. Pfeiffer and A. Grbic, "Millimeter-wave transmitarrays for wavefront and polarization control," *IEEE Trans. Microw. Theory Tech.*, vol. 61, no. 12, pp. 4407–4417, Dec. 2013.
- [41] Q.-Y. Chen, S.-W. Qu, X.-Q. Zhang, and M.-Y. Xia, "Low-profile wideband reflectarray by novel elements with linear phase response," *IEEE Antennas Wireless Propagat. Lett.*, vol. 11, pp. 1545–1547, 2012.
- [42] A. Vallecchi, J. R. de Luis, F. Capolino, and F. de Flaviis, "Low profile fully planar folded dipole antenna on a high impedance surface," *IEEE Trans. Antennas Propagat.*, vol. 60, no. 1, pp. 51–62, Jan. 2012.
- [43] L. Akhoondzadesh-Asl, D. J. Kern, P. S. Hall, and D. H. Werner, "Wideband dipoles on electromagnetic bandgap ground planes," *IEEE Trans. Antennas Propagat.*, vol. 55, no. 9, pp. 2426–2434, Sep. 2007.
- [44] H. R. Raad, A. I. Abbosh, H. M. Al-Rizzo, and D. G. Rucker, "Flexible and compact AMC based antenna for telemedicine applications," *IEEE Trans. Antennas Propagat.*, vol. 61, no. 2, pp. 524–531, Feb. 2013.
- [45] F. Yang, V. Demir, D. A. Elsherbeni, A. Z. Elsherbeni, and A. A. Eldek, "Planar dipole antennas near the edge of an EBG ground plane," in *Proc. Antennas Propagat. Symp.*, Jul. 2005, vol. 1A, pp. 750–753.
- [46] H. Mosallaei and K. Sarabandi, "Antenna miniaturization and bandwidth enhancement using a reactive impedance substrate," *IEEE Trans. Antennas Propagat.*, vol. 52, no. 9, pp. 2403–2414, Sep. 2004.

- [47] H.-X. Xu, G.-M. Wang, J.-G. Liang, M. Q. Qi, and X. Gao, "Compact circularly polarized antennas combining meta-surfaces and strong space-filling meta-resonators," *IEEE Trans. Antennas. Propagat.*, vol. 61, no. 7, pp. 3442–3450, Jul. 2013.
- [48] T. Nakamura and T. Fukusako, "Broadband design of circularly polarized microstrip patch antenna using artificial ground structure with rectangular unit cells," *IEEE Trans. Antennas Propagat.*, vol. 59, no. 6, pp. 2103–2110, Jun. 2011.
- [49] L. Bernard, G. Chertier, and R. Sauleau, "Wideband circularly polarized patch antennas on reactive impedance substrates," *IEEE Antennas Wireless Propagat. Lett.*, vol. 10, pp. 1015–1018, 2011.
- [50] B. S. Cook, and A. Shamim, "Utilizing Wideband AMC structures for high-gain inkjet-printed antennas on lossy paper substrate," *IEEE Antennas Wireless Propagat. Lett.*, vol.12, pp.76-79, 2013.
- [51] P. Prakash, M. P. Abegaonkar, A. Basu, and S. K. Koul, "Gain enhancement of a CPW-fed monopole antenna using polarization insensitive AMC structure," *IEEE Antennas Wireless Propagat. Lett.*, vol. 12, pp. 1315–1318, 2013.
- [52] W. Liu, Z. N. Chen, and X. Qing, "Metamaterial-based low-profile broadband mushroom antenna," *IEEE Trans. Antennas Propagat.*, vol. 62, no. 3, pp. 1165–1172, Mar. 2014.
- [53] F. Yang and Y. Rahmat-Samii, "A low profile single dipole antenna radiating circularly polarized waves," *IEEE Trans. Antennas Propagat.*, vol. 53, no. 9, pp. 3083–3086, Sep. 2005.
- [54] T. Cai, G. Wang, and J. Liang, "Analysis and design of novel 2-D transmission-line metamaterial and its application to compact dual-band antenna," *IEEE Antennas Wireless Propagat. Lett.*, vol. 13, pp. 555–558, 2014.
- [55] H.-X. Xu, G.-M. Wang, M.-Q. Qi, C.-X. Zhang, J.-G. Liang, J.-Q. Gong, and Y.-C. Zhou, "Analysis and design of two-dimensional resonant-type composite right/left-handed transmission

lines with compact gain-enhanced resonant antennas,” *IEEE Trans. Antennas Propagat.*, vol. 61, no. 2, pp. 735–747, 2013.

[56] Y. Dong, H. Toyao, and T. Itoh, “Design and characterization of miniaturized patch antennas loaded with complementary split-ring resonators,” *IEEE Trans. Antennas Propagat.*, vol. 60, no. 2, pp. 772–785, Feb. 2012.

[57] B. F. Zong, G. M. Wang, C. Zhou, and Y. W. Wang, “Compact low profile dual-band patch antenna using novel TL-MTM structures,” *IEEE Antennas Wireless Propagat. Lett.*, vol. 14, pp. 567–570, Nov. 2015.

[58] Y. Dong, H. Toyao, and T. Itoh, “Compact circularly-polarized patch antenna loaded with metamaterials,” *IEEE Trans. Antennas Propagat.*, vol. 59, no. 11, pp. 4329–4333, Nov. 2011.

[59] T. Yue, Z. H. Jiang, and D. H. Werner, “Compact, wideband antennas enabled by interdigitated capacitor-loaded metasurfaces,” *IEEE Trans. Antennas Propagat.*, vol. 64, no. 5, pp. 1595–1606, May. 2016.

[60] W. Liu, Z. N. Chen, and X. M. Qing, “Metamaterial-based low-profile broadband aperture coupled grid-slotted patch antenna,” *IEEE Trans. Antennas Propagat.*, vol. 63, no. 7, pp. 3325–3329, Jul. 2015.

[61] Q. Wu, C. P. Scarborough, D. H. Werner, E. Lier, and X. Wang, “Design synthesis of metasurfaces for broadband hybrid-mode horn antennas with enhanced radiation pattern and polarization characteristics,” *IEEE Trans. Antennas Propagat.*, vol. 60, no. 8, pp. 3594–3604, Aug. 2012.

[62] J. D. Baena, J. Bonache, F. Martin, R. M. Sillero, F. Falcone, T. Lopetegi, M. A. G. Laso, J. Garcia-Garcia, I. Gil, M. F. Portillo, and M. Sorolla, “Equivalent-circuit models for split-ring resonators and complementary split-ring resonators coupled to planar transmission lines,” *IEEE Trans. Microw. Theory Tech.*, vol. 53, no. 4, pt. 2, pp. 1451–1461, Apr. 2005.

- [63] D. H. Werner and Z. H. Jiang, Eds., *Electromagnetics of Body Area Networks: Antennas, Propagation, and RF Systems*. Hoboken, NJ, USA: Wiley, 2016.
- [64] C. Sun, H. Zheng, and Y. Liu, "Analysis and design of a low-cost dual-band compact circularly polarized antenna for GPS application," *IEEE Trans. Antennas Propag.*, vol. 64, no. 1, pp. 365–370, Jan. 2016.
- [65] O. P. Falade, M. U. Rehman, Y. Gao, X. Chen, and C. G. Parini, "Single feed stacked patch circular polarized antenna for triple band GPS receivers," *IEEE Trans. Antennas Propag.*, vol. 60, no. 10, pp. 4479–4484, Oct. 2012.
- [66] Y. Zhou, C. C. Chen, and J. L. Volakis, "Dual band proximity-fed stacked patch antenna for tri-band GPS applications," *IEEE Trans. Antennas Propag.*, vol. 55, no. 1, pp. 220–223, Jan. 2007.
- [67] M. Chen and C. C. Chen, "A compact dual-band GPS antenna design," *IEEE Antennas Wireless Propag. Lett.*, vol. 12, pp. 245–248, Mar. 2013.
- [68] S. Gupta and G. Mumcu, "Dual-band miniature coupled double loop GPS antenna loaded with lumped capacitors and inductive pins," *IEEE Trans. Antennas Propag.*, vol. 61, no. 6, pp. 2904–2910, Jun. 2013.
- [69] S. X. Ta, I. Park, and R. W. Ziolkowski, "Multi-band, wide-beam, circularly polarized, crossed, asymmetrically barbed dipole antennas for GPS applications," *IEEE Trans. Antennas Propag.*, vol. 61, no. 11, pp. 5771–5775, Nov. 2013.
- [70] Nasimuddin, Z. N. Chen, and X. Qing, "Dual-band circularly polarized S-shaped slotted patch antenna with a small frequency-ratio," *IEEE Trans. Antennas Propag.*, vol. 58, no. 6, pp. 2112–2115, Jun. 2010.
- [71] L. Boccia, G. Amendola, and G. Massa, "A dual frequency microstrip patch antenna for high-precision GPS applications," *IEEE Antennas Wireless Propag. Lett.*, vol. 3, pp. 157–160, 2004.

- [72] S. Chen, G. Liu, X. Chen, T. Lin, X. Liu, and Z. Duan, "Compact dual-band GPS microstrip antenna using multilayer LTCC substrate," *IEEE Antennas Wireless Propag. Lett.*, vol. 9, pp. 421–423, May. 2010.
- [73] W. Hsieh, T. Chang, and J. Kiang, "Dual-band circularly polarized cavity-backed annular slot antenna for GPS receiver," *IEEE Trans. Antennas Propag.*, vol. 60, no. 4, pp. 2076–2080, Apr. 2012.
- [74] X. Sun, Z. Zhang, and Z. Feng, "Dual-band circularly polarized stacked annular-ring patch antenna for GPS application," *IEEE Antennas Wireless Propag. Lett.*, vol. 10, pp. 49–52, Mar. 2011.
- [75] S. X. Ta, I. Park, and R. W. Ziolkowski, "Dual-band wide-beam crossed asymmetric dipole antenna for GPS application," *Electron. Lett.*, vol. 48, no. 25, pp. 1580–1581, Dec. 2012.
- [76] Q. Liu, J. Shen, J. Yin, H. Liu, and Y. Liu, "Compact 0.92/2.45-GHz dual-band directional circularly polarized microstrip antenna for handheld RFID reader applications," *IEEE Trans. Antennas Propag.*, vol. 63, no. 9, pp. 3849–3856, Sept. 2015.
- [77] R. Caso, A. Michel, M. Rodriguez-Pino, and P. Nepa, "Dual-band UHF-RFID/WLAN circularly polarized antenna for portable RFID readers," *IEEE Trans. Antennas Propag.*, vol. 62, no. 5, pp. 2822–2826, May 2014.
- [78] Q. Liu, J. Shen, H.-L. Liu, and Y.-A. Liu, "Dual-band circularly-polarized unidirectional patch antenna for RFID reader applications," *IEEE Trans. Antennas Propag.*, vol. 62, no. 12, pp. 6428–6434, Dec. 2014.
- [79] Y. K. Jung and B. Lee, "Dual-band circularly polarized microstrip RFID reader antenna using metamaterial branch-line coupler," *IEEE Trans. Antennas Propag.*, vol. 60, no. 2, pp. 786–791, Feb. 2012.
- [80] T. N. Chang and J. M. Lin, "Serial aperture-coupled dual-band circularly polarized antenna," *IEEE Trans. Antennas Propag.*, vol. 59, no. 6, pp. 2419–2423, Jun. 2011.

- [81] S. X. Ta and I. Park, "Dual-band low-profile crossed asymmetric dipole antenna on dual-band AMC surface," *IEEE Antennas Wireless Propag. Lett.*, vol. 13, pp. 587–590, Apr. 2014.
- [82] K. Saurav, D. Sarkar, A. Singh, and K. V. Srivastava, "Multiband circularly polarized cavity-backed crossed dipole antenna", *IEEE Trans. Antennas Propag.*, vol. 63, no. 10, pp. 4286 – 4296, Oct. 2015.
- [83] S. X. Ta, J. Jin Han, and R. W. Ziolkowski, "Circularly polarized crossed dipole on an HIS for 2.4/5.2/5.8-GHz WLAN applications," *IEEE Antennas Wireless Propag. Lett.*, vol. 12, pp. 1464–1467, Nov. 2013.
- [84] X. L. Bao and M. J. Ammann, "Dual-frequency dual circularly-polarized patch antenna with wide beamwidth," *Electron. Lett.*, vol. 44, no. 21, pp. 1233–1234, Oct. 2008.
- [85] F. Ferreco, C. Luxey, G. Jacquemod, and R. Staraj, "Dual-band circularly polarized microstrip antenna for satellite applications," *IEEE Antennas Wireless Propag. Lett.*, vol. 4, pp. 13–15, Jun.2005.
- [86] Y. J. Sung and Y. S. Kim, "Circular polarised microstrip patch antennas for broadband and dual-band operation," *Electron. Lett.*, vol. 40, no. 9, pp. 520–522, Apr.2004.
- [87] J.-D. Zhang, W. Wu, and D.-G. Fang, "Dual-band and dual-circularly polarized shared-aperture array antennas with single-layer substrate," *IEEE Trans. Antennas Propag.*, vol. 64, no. 1, pp. 109-116, Jan. 2016.
- [88] K. Chen, J. Yuan and X. Luo, "Compact dual-band dual circularly polarised annular-ring patch antenna for BeiDou navigation satellite system application," *IET Microw., Antennas Propag.*, vol. 11, no. 8, pp. 1079-1085, Jul. 2017.
- [89] C.-H. Chen and E. K. N. Yung, "Dual-band circularly-polarized CPW-fed slot antenna with a small frequency ratio and wide bandwidths," *IEEE Trans. Antennas Propag.*, vol. 59, no. 4, pp. 1379–1384, Apr. 2011.

- [90] C.-H. Chen and E. K. N. Yung, "Dual-band dual-sense circularly-polarized CPW-fed slot antenna with two spiral slots loaded," *IEEE Trans. Antennas Propag.*, vol. 57, no. 6, pp. 1829–1834, Jun. 2009.
- [91] X. L. Bao and M. J. Ammann, "Dual-frequency dual-sense circularly polarized slot antenna fed by microstrip line," *IEEE Trans. Antennas Propag.*, vol. 56, no. 3, pp. 645–649, Mar. 2008.
- [92] D.-C. Chang, B. H. Zeng, and J.-C. Liu, "CPW-fed circular fractal slot antenna design for dual-band applications," *IEEE Trans. Antennas Propag.*, vol. 56, no. 12, pp. 3630–3636, Dec. 2008.
- [93] K. Saurav, D. Sarkar, and K. V. Srivastava, "Dual-band circularly polarized cavity-backed crossed-dipole antennas," *IEEE Antennas Wireless Propag. Lett.*, vol. 14, pp. 52–55, Jan. 2015.
- [94] Y. Ding and K. W. Leung, "Dual-band circularly polarized dual-slot antenna with a dielectric cover," *IEEE Trans. Antennas Propag.*, vol. 57, no. 12, pp. 3757–3764, Dec. 2009.
- [95] K. Kandasamy, B. Majumder, J. Mukherjee, and K. P. Ray, "Dual-band circularly polarized split ring resonators loaded square slot antenna," *IEEE Trans. Antennas Propag.*, vol. 64, no. 8, pp. 3640–3645, Aug. 2016.
- [96] Y. Q. Zhang, X. Li, L. Yang, and S. X. Gong, "Dual-band circularly polarized annular-ring microstrip antenna for GNSS applications," *IEEE Antennas Wireless Propag. Lett.*, vol. 12, pp. 615–618, Apr. 2013.
- [97] J. X. Li, H. Y. Shi, H. Li, and A. X. Zhang, "Quad-band probe-fed stacked annular patch antenna for GNSS applications," *IEEE Antennas Wireless Propag. Lett.*, vol. 13, pp. 372–375, Mar. 2014.
- [98] Z. Wang, S. Fang, S. Fu, and S. Lu, "Dual-band probe-fed stacked patch antenna for GNSS applications," *IEEE Antennas Wireless Propag. Lett.*, vol. 8, pp. 100–103, Apr. 2009.

- [99] Q. Wu, H. M. Wang, C. Yu, X. W. Zhang, and W. Hong, "L/S band dual circularly polarized antenna fed by 3-dB coupler," *IEEE Antennas Wireless Propag. Lett.*, vol. 14, pp. 426-429, Feb.2015.
- [100] D. Sanchez-Hernandez, G. Passiopoulos, M. Ferrando, E. Reyes, and I. D. Robertson, "Dual-band circularly polarized microstrip antennas with a single feed," *Electron. Lett.*, vol. 32, pp. 2296–2298, Dec.1996.
- [101] C. H. Cai, J. S. Row, and K. L. Wong, "Dual-frequency microstrip antenna with dual circular polarization," *Electron. Lett.*, vol. 42, no. 22, pp. 1261–1262, Oct. 2006.
- [102] K. Wincza and S. Gruszczynski, "Series-fed dual-band dual-polarized antenna lattice fed by slot-coupled power dividers," *IEEE Antennas Wireless Propag. Lett.*, vol. 15, pp. 1065 - 1068, Mar.2016.
- [103] H. Yi and S.-W. Qu, "A novel dual-band circularly polarized antenna based on electromagnetic band-gap structure," *IEEE Antennas Wireless Propag. Lett.*, vol. 12, pp. 1149–1152, Sept.2013.
- [104] X. L. Bao and M. J. Ammann, "Dual-frequency circularly-polarized patch antenna with compact size and small frequency ratio," *IEEE Trans. Antennas Propag.*, vol. 55, no. 7, pp. 2104–2107, Jul. 2007.
- [105] C. H. Chen and E. K. N. Yung, "A novel unidirectional dual-band circularly-polarized patch antenna," *IEEE Trans. Antennas Propag.*, vol. 59, no. 8, pp. 3052–3057, Aug. 2011.
- [106] K.-P. Yang and K.-L. Wong, "Dual band circularly-polarized square microstrip antenna," *IEEE Trans. Antennas Propag.*, vol. 49, no. 3, pp. 377–382, Mar. 2001.
- [107] C. J. Deng, Y. Li, Z. J. Zhang, G. P. Pan, and Z. H. Feng, "Dual-band circularly polarized rotated patch antenna with a parasitic circular patch loading," *IEEE Antennas Wireless Propag. Lett.*, vol. 12, pp. 492–495, Apr.2013.

- [108] J.-D. Zhang, L. Zhu, N.-W. Liu, and W. Wu, "Dual-band and dual-circularly polarized single-layer microstrip array based on multiresonant modes," *IEEE Trans. Antennas Propag.*, vol. 65, no. 3, pp. 1428-1433, Mar. 2017.
- [109] G. B. Hsieh, M. H. Chen, and K. L. Wong, "Single-feed dual-band circularly polarised microstrip antenna," *Electron. Lett.*, vol. 34, no. 12, pp. 1170–1171, Jun. 1998.
- [110] J. S. Row, "Dual-frequency circularly polarised annular-ring microstrip antenna," *Electron. Lett.*, vol. 40, no. 3, pp. 153–154, Feb.2004.
- [111] S. Wang, L. Zhu, and W. Wu, "3-D printed inhomogeneous substrate and superstrate for application in dual-band and dual-CP stacked patch antenna," *IEEE Trans. Antennas Propag.*, vol. PP, no. 99, pp. 1–1, Feb. 2018.
- [112] P. Nayeri, K.-F. Lee, A. Z. Elsherbeni, and F. Yang, "Dual-band circularly polarized antennas using stacked patches with asymmetric U-slots," *IEEE Antennas Wireless Propag. Lett.*, vol. 10, pp. 492-495, May.2011.
- [113] Z.-X. Liang, D.-C. Yang, X.-C. Wei, and E.-P. Li, "Dual-band dual circularly polarized microstrip antenna with two eccentric rings and an arc-shaped conducting strip," *IEEE Antennas Wireless Propag. Lett.*, vol. 15, pp. 834-837, Mar.2016.
- [114] K. Li, L. Li, J. Y.-M. Liu, C Zhu, and C.-H. Liang, "A novel design of low-profile dual-band circularly polarized antenna with meta-surface," *IEEE Antennas Wireless Propag. Lett.*, vol. 14, pp. 1650–1653, Sep. 2015.
- [115] L. Yan, W. Hong, G. Hua, J. Chen, K. Wu, and T. J. Cui, "Simulation and experiment on SIW slot array antennas," *IEEE Microw. Wireless Compon. Lett.*, vol. 14, no. 9, pp. 446–448, Sep. 2004.
- [116] Y. J. Cheng, W. Hong, and K. Wu, "Design of a monopulse antenna using a dual V-type linearly tapered slot antenna (DVL TSA)," *IEEE Trans. Antennas Propag.*, vol. 56, pp. 2903–2909, Sep. 2008.

- [117] F. Xu, K. Wu, and X. Zhang, "Periodic leaky-wave antenna for millimeter wave applications based on substrate integrated waveguide," *IEEE Trans. Antennas Propag.*, vol. 58, no. 2, pp. 340–347, Feb. 2010.
- [118] H. Wang, D. Fang, B. Zhang, and W. Che, "Dielectric loaded substrate integrated waveguide (SIW) H-plane horn antennas," *IEEE Trans. Antennas Propag.*, vol. 58, no. 3, pp. 640–647, Mar. 2010.
- [119] G. Q. Luo, Z. F. Hu, L. X. Dong, and L. L. Sun, "Planar slot antenna backed by substrate integrated waveguide cavity," *IEEE Antennas Wireless Propag. Lett.*, vol. 7, pp. 236–239, Aug. 2008.
- [120] M. H. Awida and A. E. Fathy, "Substrate-integrated waveguide KU-band cavity-backed 2 × 2 microstrip patch array antenna," *IEEE Antennas Wireless Propag. Lett.*, vol. 8, pp. 1054–1056, Oct. 2009.
- [121] Y. Q. Wang, W. Hong, Y. D. Dong, B. Liu, H. J. Tang, J. X. Chen, X. X. Yin, and K. Wu, "Half mode substrate integrated waveguide (HMSIW) bandpass filter," *IEEE Microw. Wireless Compon. Lett.*, vol. 17, no. 4, pp. 265–267, Apr. 2007.
- [122] S. A. N. M. Razavi, "Development of a linearly polarized cavity-backed antenna using HMSIW technique," *IEEE Antennas Wirel. Propag. Lett.*, vol. 11, pp. 1307–1310, 2012.
- [123] C. Jin, R. Li, A. Alphones, and X. Bao, "Quarter-mode substrate integrated waveguide and its application to antennas design," *IEEE Trans. Antennas Propag.*, vol. 61, no. 6, pp. 2921–2928, Jun. 2013.
- [124] Q. Wu, H. Wang, C. Yu, and W. Hong, "Low-profile circularly polarized cavity-backed antennas using SIW techniques," *IEEE Trans. Antennas Propag.*, vol. 64, no. 7, pp. 2832–2839, Jul. 2016.
- [125] R. Moro, S. Agneessens, H. Rogier, and M. Bozzi, "Wearable textile antenna in substrate integrated waveguide technology," *Electron. Lett.*, vol. 48, no. 16, pp. 985–987, Aug. 2012.

- [126] S. Agneessens and H. Rogier, "Compact half diamond dual-band textile HMSIW on-body antenna," *IEEE Trans. Antennas Propag.*, vol. 62, no. 5, pp. 2374–2381, May 2014.
- [127] T. Kaufmann and C. Fumeaux, "Wearable textile half-mode substrate-integrated cavity antenna using embroidered vias," *IEEE Antennas Wireless Propag. Lett.*, vol. 12, pp. 805–808, 2013.
- [128] S. Agneessens, S. Lemey, T. Vervust, and H. Rogier, "Wearable, small, and robust: The circular quarter-mode textile antenna," *IEEE Antennas Wireless Propag. Lett.*, vol. 14, pp. 1482–1485, 2015.
- [129] S. Yan, P. J. Soh, and G. A. Vandenbosch, "Dual-band textile MIMO antenna based on substrate-integrated waveguide (SIW) technology," *IEEE Trans. Antennas Propag.*, vol. 63, no. 11, pp. 4640–4647, Nov. 2015.
- [130] M. E. Lajevardi and M. Kamyab, "Ultraminiaturized Metamaterial-Inspired SIW Textile Antenna for Off-Body Applications," *IEEE Antennas Wireless Propag. Lett.*, vol. 16, pp. 3155–3158, 2015.
- [131] E. Kretschmann and H. Raether, "Radiative decay of nonradiative surface plasmons excited by light," *Z. Naturforsch. A* **23**, 2135–2136 (1968).
- [132] A. Otto, "Excitation of nonradiative surface plasma waves in silver by the method of frustrated total reflection," *Z. Phys.* **216**(4), 398–410 (1968).
- [133] P. E. Landreman and M. L. Brongersma, "Deep-subwavelength semiconductor nanowire surface plasmon polariton couplers," *Nano Lett.* **14**, 429–434 (2014).
- [134] P. Lalanne, J. P. Hugonin, and J. C. Rodier, "Theory of surface plasmon generation at nanoslit apertures," *Phys. Rev. Lett.* **95**(26), 263902 (2005).
- [135] H. Kim and B. Lee, "Unidirectional surface plasmon polariton excitation on single slit with oblique backside illumination," *Plasmonics* **4**(2), 153–159 (2009).

- [136] X. Li, Q. Tan, B. Bai, and G. Jin, “Experimental demonstration of tunable directional excitation of surface plasmon polaritons with a subwavelength metallic double slit,” *Appl. Phys. Lett.* **98**(25), 251109 (2011).
- [137] Z. Wang, M. Zhang, J. Wang, F. Lu, K. Li, and A. Xu, “Unidirectional launching of surface plasmons with subwavelength metallic gratings around the plasmonic critical angle,” *Appl. Phys. Lett.* **98**(25), 251109 (2011).
- [138] Y. Sonnefraud, S. Kerman, G. D. Martino, D. Y. Lei, and S. A. Maier, “Directional excitation of surface plasmon polaritons via nanoslits under varied incidence observed using leakage radiation microscopy,” *Opt. Express* **20**(5), 4893-4902 (2012).
- [139] F. López-Tejiera, and S. G. Rodrigo, L. Martín-Moreno, F. J. García-Vidal, E. Devaux, T. W. Ebbesen, J. R. Krenn, I. P. Radko, S. I. Bozhevolnyi, M. U. González, J. C. Weeber, and A. Dereux, “Efficient unidirectional nanoslit couplers for surface plasmons,” *Nat. Phys.* **3**, 324 (2007).
- [140] M. -D. He, K. -J. Wang, L. Wang, J. -B. Li, J. -Q. Liu, Z. -R. Huang, L. Wang, L. Wang, W. -D. Hu, and X. Chen, “Graphene-based terahertz tunable plasmonic directional coupler,” *Appl. Phys. Lett.* **105**(8), 081903 (2014).
- [141] C. Lu, X. Hu, H. Yang, and Q. Gong, “Chip-integrated ultrawide-band all-optical logic comparator in plasmonic circuits,” *Sci. Rep.* **4**, 3869 (2014).
- [142] C. Lu, X. Hu, H. Yang, and Q. Gong, “Integrated all-optical logic discriminators based on plasmonic bandgap engineering,” *Sci. Rep.* **3**, 2778 (2013).
- [143] C. Lu, X. Hu, H. Yang, and Q. Gong, “Ultrawide-Band Unidirectional Surface Plasmon Polariton Launchers,” *Adv. Opt. Mater.* **1**, 792–797 (2013).
- [144] J. J. Chen, Z. Li, S. Yue, and Q. H. Gong, “Efficient unidirectional generation of surface plasmon polaritons with asymmetric single-nanoslit,” *Appl. Phys. Lett.* **97**(4), 041113 (2010).
- [145] J. Chen, Z. Li, S. Yue, and Q. Gong, “Ultracompact surface-plasmon-polariton splitter based on modulations of quasicylindrical waves to the total field,” *J. Appl. Phys.* **109**, 073102 (2011).

- [146] J. J. Chen, Z. Li, S. Yue, and Q. H. Gong, "Highly efficient all-optical control of surface-plasmon-polariton generation based on a compact asymmetric single slit," *Nano Lett.* **11**(7), 2933–2937 (2011).
- [147] J. Chen, Z. Li, M. Lei, S. Yue, J. Xiao, and Q. Gong, "Broadband unidirectional generation of surface plasmon polaritons with dielectric-film-coated asymmetric single-slit," *Opt. Express* **19**, 26463-26469 (2011).
- [148] A. Baron, E. Devaux, J. C. Rodier, J. P. Hugonin, E. Rousseau, C. Genet, T. W. Ebbesen, and P. Lalanne, "Compact antenna for efficient and unidirectional launching and decoupling of surface plasmons," *Nano Lett.* **11**, 4207–4212 (2011).
- [149] L. Wang, T. Li, L. Li, W. Xia, X. G. Xu, and S. N. Zhu, "Electrically generated unidirectional surface plasmon source," *Opt. Express* **20**(8), 8710–8717 (2012).
- [150] J. Yang, X. Xiao, C. Hu, W. Zhang, S. Zhou, and J. Zhang, "Broadband surface plasmon polariton directional coupling via asymmetric optical slot nanoantenna pair," *Nano Lett.* **14**(2), 704–709 (2014).
- [151] F. Huang, X. Jiang, H. Yang, S. Li, and X. Sun, "Splitting of a surface plasmon polariton beam by chains of nanoparticles," *Appl. Phys. B* **122**, 16 (2016).
- [152] T. Yue, Z. H. Jiang, A. H. Panaretos, and D. H. Werner, "A compact dual-band antenna enabled by a complementary split-ring resonator-loaded metasurface," *IEEE Trans. Antennas Propag.*, vol. 65, no. 12, pp. 6878 - 6888, Dec. 2017.
- [153] T. Yue, Z. H. Jiang, and D. H. Werner, "A compact metasurface-enabled dual-band dual-sense circularly-polarized antenna loaded with complementary split ring resonators," submitted to *IEEE Trans. Antennas Propag.*, 2018.

VITA

Taiwei Yue

Born in Wuhan, China, 02/10/1991.

Educational Background

Doctor of Philosophy Aug. 2013 – Aug. 2018

Electrical Engineering

The Pennsylvania State University, University Park, PA, USA

Bachelor of Science Sept. 2009 – Jun. 2013

Physics

Nanjing University, Nanjing, China

Selected Journal Publications

- T. Yue, Z. H. Jiang, and D. H. Werner, "Compact, wideband antennas enabled by interdigitated capacitor-loaded metasurfaces," *IEEE Trans. Antennas Propag.*, vol. 64, no. 5, pp. 1595–1606, May 2016.
- T. Yue, Z. H. Jiang, A. H. Panaretos, and D. H. Werner, "A compact dual-band antenna enabled by a complementary split-ring resonator-loaded metasurface," *IEEE Trans. Antennas Propag.*, vol. 65, no. 12, pp. 6878 - 6888, Dec. 2017.
- T. Yue, Z. H. Jiang, and D. H. Werner, "A compact metasurface-enabled dual-band dual-sense circularly-polarized antenna loaded with complementary spit ring resonators," submitted to *IEEE Trans. Antennas Propagt.*, 2018.
- Z. H. Jiang, Z. Cui, T. Yue, Y. Zhu, and Douglas H. Werner, "Compact, highly efficient, and fully flexible circularly polarized antenna enabled by silver nanowires for wireless body-area networks," *IEEE Trans. Biomed. Circuit Syst.*, Vol. 11, No. 4, pp. 920-932, May 2017.
- B. Q. Lu, J. Nagar, T. Yue, M. F. Pantoja, and D. H. Werner, "Closed-Form Expressions for the Radiation Properties of Nanoloops in the Terahertz, Infrared and Optical Regime," *IEEE Trans. Antennas Propagt.*, Vol. 65, No. 1, pp. 121-133, Nov 2016.
- L. Kang, Z. H. Jiang, T. Yue, and D. H. Werner, "Handedness Dependent Electromagnetically Induced Transparency in Hybrid Chiral Metamaterials," *Sci. Rep.* **5**, 12224; doi: 10.1038/srep12224 (2015).